

Development of a high flux capability
neutron detection system in harsh
environment using a CVD diamond
detector

CVDダイヤモンド検出器を用いた混在
場高線量下で使える中性子束計測シス
ムの開発

XU XIUQING

DOCTOR OF PHILOSOPHY

Department of Accelerator Science

School of High Energy Accelerator Science

The Graduate University for Advanced Studies,
SOKENDAI

Tsukuba - December, 2021

Supervisor: Hiroshi Iwase
Masayuki Hagiwara
Head Examiner: Yoshihito Namito
Examiner: Toshiya Sanami
Masayuki Hagiwara
Yuji Kishimoto
Kiwamu Saito
Hiroshi Iwase

For all who supported me.

Abstract

The chemical vapor deposition (CVD) diamond detector is an attractive semiconductor detector owing to its advantages, such as its large bandgap, high electron–hole mobility, low leakage current, excellent timing resolution, and outstanding radiation hardness. In particular, the low γ -ray sensitivity and outstanding radiation hardness of the diamond detector make it suitable for neutron measurements in harsh radiation environment such as the containment vessel of Fukushima Daiichi nuclear power plant (NPP) and beamline tunnels of high intensity accelerators (e.g., Super KEKB, J-PARC, and LHC). In this study, a high flux capability neutron detection system for harsh radiation environments using CVD diamond detectors was developed.

The detector system consists of CVD diamond detectors coupled to a thin layer of ${}^6\text{LiF}$. In the detector-system design, the n/γ separation was improved by decreasing the gamma-pulse height through a reduction in the thickness of the diamond crystal. The thickness was determined with consideration of the charged-particle range in the diamond. The effect of the thickness on the energy-deposition spectrum was evaluated by performing simulations involving monoenergetic neutrons and γ -rays with various energies. The thickness of 25 μm was selected according to the energy-deposition spectrum, γ -ray sensitivity, and energy gives 99.99% events. CVD diamond detectors with ${}^6\text{LiF}$ neutron converters of two different thicknesses—25 μm (the improved design) and 140 μm (from the CIVIDEC product catalogue)—were acquired for tests of the basic properties and experimental response. The detectors both had equal active areas of 10 mm^2 and were manufactured by CIVIDEC (Vienna, Austria).

The detectors were characterized with regard to the current–voltage characteristics, charge-collection efficiency (CCE), and alpha-particle energy resolution with signal readout through a charge-sensitive preamplifier and linear amplifier (analogue readout). For the 25- μm -thick diamond detector, the leakage current was <10 pA under electric fields of <15 kV/cm. The CCEs of the detectors were measured using a mixed alpha-source, which was composed of ${}^{148}\text{Gd}$ (3.183 MeV), ${}^{241}\text{Am}$ (5.486 MeV), and ${}^{244}\text{Cm}$ (5.805 MeV). The maximum CCEs for the 25- μm -thick detector were 91.1%, 95.7%, and 96.0%, respectively, which were comparable to those for the 140- μm -thick detector.

The γ -ray irradiation experiments were performed at dose rates of 0.693–107 Gy/h using electronics with analog readout. The apparent energy deposition of the 140- μm -thick detector exceeded the peak energy (2.73 MeV) of triton produced in the ${}^6\text{Li}(n, \alpha){}^3\text{H}$ reaction at 6.36 Gy/h owing to signal pile-up effects, which enhanced the spillover between the pulse-height distributions of γ -ray and neutron events. Although, the 25- μm -thick diamond detector also exhibited significant pile-up effects, the neutron/gamma discrimination capability was maintained with the pulse-height distributions even at 107 Gy/h. This indicates that the 25- μm -thick diamond detector can be used for neutron measurements in the presence of a strong

background of γ -rays beyond 100 Gy/h even with the analog readout.

The responses of the detectors to thermal neutrons were studied through measurements and Monte Carlo simulations using the Particle and Heavy-Ion Transport Code System (PHITS). The measurement of thermal neutrons was performed using thermalized neutrons from an ^{241}Am -Be neutron source at the radiation calibration facility of the High Energy Accelerator Research Organization (KEK). The neutron source was at the center of a graphite pile that consisted of high-purity carbon, which produced a thermal-neutron field. The experimental and simulated results agreed well for the triton peaks, which were used to evaluate the thermal-neutron sensitivity. When the distance between the source and the detector surface was set as 47 cm, the thermal-neutron detection efficiency of the 25- μm -thick diamond detector was $1.04 \times 10^{-3} \pm 9 \times 10^{-5}$. In fast-neutron tests, triton peak count rates were obtained for 144-keV, 565-keV, 1.2-MeV, 5-MeV, and 14.8-MeV neutrons with an acrylic slab phantom for the 25- μm -thick detector. These results indicated that the reduction of the detector thickness from 140 to 25 μm was improved the effectiveness of the detector for thermal- and fast-neutron detection for γ -ray rejection.

For rejecting the pulse pile-up events and measuring the transient current signals with durations of a few nanoseconds, a fast current-sensitive preamplifier (CIVIDEC C2-TCT) with a 2-GHz bandwidth and 40-dB gain, and a 10-bit waveform digitizer (Agilent-Acqiris DC282) with a bandwidth of 1.5 GHz and a sampling rate of 2 GS/s (hereinafter referred to as the “TCT digital system”) was applied for signal readout instead of analogue readout. The pulse width of the signal was <10 ns, which was approximately several hundred times shorter than that of the charge-sensitive preamplifier. To confirm the energy resolution and γ -ray sensitivity of the detector with the TCT digital system, responses for this combination were measured for the alpha-particles from a mixed alpha-source (^{148}Gd , ^{241}Am , ^{244}Cm) and γ -rays from a ^{60}Co source with dose rates of 107 Gy/h. The 25- and 140- μm -thick CVD diamond detectors with the TCT digital system exhibited energy resolutions of 3.9% and 2.8%, respectively, at the ^{241}Am - α energy (5.486 MeV). Neither detector exhibited pile-up effects, even when exposed to intense γ -rays with dose rates of 107 Gy/h. The pulse-height distribution exhibited lower energy resolutions than that for analog readout. Nonetheless, these energy resolutions were sufficient for determining an appropriate threshold to discriminate γ -ray events from neutron events.

To test the detectors with the TCT digital system in a mixed radiation field of the electron accelerator target area that consisted of γ -rays and neutrons, the responses of the detectors were experimentally obtained at the electron linear accelerator facility of the Institute for Integrated Radiation and Nuclear Science, Kyoto University (KURNS). The thermal-neutron flux was $1.86 \times 10^5 \pm 0.16 \times 10^5$ $\text{cm}^{-2}\text{s}^{-1}$ at a 30-MeV beam energy, with an average current of 3.5 μA on the tungsten target and a water moderator.

To measure fast neutrons, the detector was used with a Bonner sphere spec-

trometer (BSS) that consisted of moderators with five diameters: 0 (bare), 40, 70, 110, and 190 mm. The Bonner sphere response functions were simulated using the PHITS Monte Carlo code. The BSS response-function tests were conducted for neutron sources of $^{241}\text{Am-Be}$ and ^{252}Cf . Using the SANDII unfolding code, the neutron spectra of the sources were accurately reproduced. Then, the BSS was used for the measurement of the neutron energy spectrum behind the 369.27 MeV-1 μA electron beam dump in the tunnel of the Superconducting Linac Test Facility at KEK. The unfolded neutron spectrum that was obtained agreed well with one obtained from a simulation for below hundreds of keV.

Contents

1	Introduction	1
1.1	Background	1
1.2	Short review of neutron detectors used in harsh radiation environments	5
1.3	Overview of diamond detector	7
1.3.1	Classification based on crystal structure	7
1.3.2	Thermal-neutron detection	8
1.3.3	Fast-neutron detection	10
1.3.4	Gamma rejection	11
1.3.5	Readout system	13
1.4	Objective of this study	14
2	Simulation analysis of thickness of diamond detector	15
2.1	Structure of diamond detector in simulation	16
2.2	Response of diamond detector with gamma-source	18
2.3	Response of diamond detector with neutron-source	24
3	Experimental characterization of diamond crystals	28
3.1	Current–voltage characteristics	30
3.2	Charge collection efficiency (CCE)	32
4	The response of diamond detector with traditional analog system	36
4.1	Experiment	36
4.1.1	Energy resolution	36
4.1.2	Response for Moderate activity γ -ray	36
4.1.3	High dose rate γ -ray responses experiment	38
4.1.4	Thermal-neutron response and detection efficiency measurement	39
4.1.5	Fast neutron	42
4.2	Simulation	45

4.3	Result and discussion	47
4.3.1	Energy resolution	47
4.3.2	Response to moderate-activity gamma-source	49
4.3.3	Response to high dose rate γ -ray	52
4.3.4	Thermal-neutron response and detection efficiency	54
4.3.5	Response of the fast neutron with water phantoms	57
5	Response of diamond detector using TCT-Acqiris digital system	65
5.1	Pulse-height analysis processing	66
5.2	Experiment	68
5.2.1	Energy resolution	68
5.2.2	High-dose rate γ -ray response experiment	68
5.2.3	Thermal-neutron response and detection efficiency	68
5.2.4	Application of TCT-Acqiris digital system using compact accelerator-based neutron sources	69
5.3	Simulation	71
5.4	Results and discussion	72
5.4.1	Energy resolution	72
5.4.2	High-dose rate γ -ray response experiment	73
5.4.3	Thermal-neutron response and detection efficiency	76
5.4.4	Application of TCT-Acqiris digital system using compact accelerator-based neutron sources	77
6	Application of response functions of Bonner sphere spectrometer	84
6.1	Simulation of response functions of BBS	85
6.2	Application of response functions of Bonner sphere spectrometer	88
6.2.1	Experiment	88
6.2.2	Simulation	91
6.2.3	Results and discussion	91
7	Conclusion	98
A	Input files of the simulation on diamond detector using PHITS102	
A.1	Flux simulation in STF tunnel	102
A.2	Energy deposition using KEK graphite pile	105
A.3	Response functions of Bonner sphere	108
A.4	Response of thermal neutron with different thicknesses	110
B	Input file of the SANDII	112

List of Figures	114
List of Tables	118
Bibliography	119
Acknowledgment	124
Declaration	125

Chapter 1

Introduction

1.1 Background

With the rapid development of nuclear physics technology and its applications, harsh radiation environments with high energy and high flux rates have become widespread, e.g., nuclear power plants(NPP) and state-of-the-art high-intensity particle accelerators.

For example, for the decommissioning of the Fukushima NPP following the accident caused by the 2011 tsunami, fuel debris needs to be characterized. Figure 1.1 shows a concept drawing of the removal of fuel debris in the pressure vessel with a neutron detector for criticality prevention [1]. Figure 1.2 shows the sediments on the fuel debris [2]. As shown in Figs. 1.1 and 1.2, the precise location and radioactive composition of the fuel debris are important for the decommissioning process. The environment around the fuel debris is submerged, making it difficult to survey the main containment vessel.

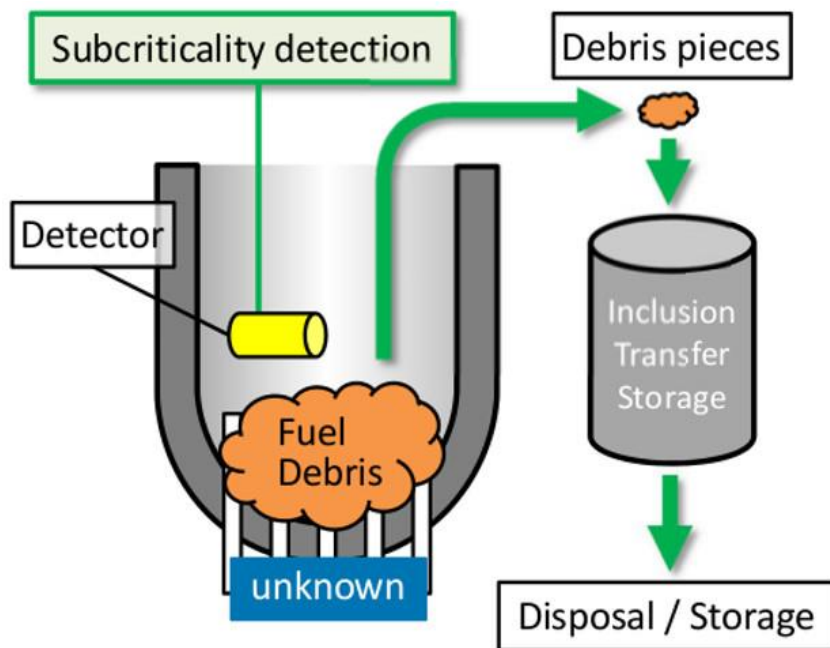


Figure 1.1: Concept of criticality prevention [1].



Figure 1.2: Sediments on the fuel debris [2].

According to IAEA report, the dose rates is expected to reach 1000 Gy/h in close proximity to fuel debris in the Fukushima NPP [3]. Under this condition, neutron detection is necessary for estimating the precise location and radiological composition of the fuel debris. In particular, monitoring of the thermal-neutron flux intensity is important for preventing critical chain reactions.

In 2018, the RIDERS project was launched (Remote Inspection of Debris under Extreme Radiation by Diamond Sensor Integrated with SONAR Systems) to develop a prototype of a submerged remotely operated vehicle (ROV) integrated with a neutron detector and sonars in collaboration with the Japanese experts from the High Energy Accelerator Research Organization (KEK), the National Institute for Materials Science (NIMS), and the National Maritime Research Institute (NMRI), targeting the onsite localization and characterization of the fuel debris at the NPP. In this project, a neutron detector with a low γ -ray sensitivity is needed for use with the ROV in the harsh radiation environment.

In an accelerator tunnel, monitoring of the neutron flux is effective for estimating the accelerator beam loss. The beams are accelerated in the accelerator along the calculated orbit. Part of particles will deviate the orbit and hit the beam pipe, the radiation is generated caused by the interaction with media. Therefore, the beam loss results from the unintended interaction of the accelerated particles with the medium. The purpose of beam-loss monitoring is to quantify the loss. Moreover, the location and temporal structure of the loss are also important. If the loss level endangers equipment, a beam shutdown could be resulted in. Feedback can be provided to improve the beam tuning. Figure 1.3 shows Livingston chart of accelerators, which indicates the development of the maximum energy [4]. With an increase in the maximum energy, the beam intensity increases significantly. Losses of energy and beam intensity have catastrophic effects on the accelerator and the environment. Beam-loss monitoring is important for the stable operation of accelerators. Beam loss produces numerous γ -rays and neutrons, leading to a harsh radiation environment. Hence, a neutron detector that can operate in harsh radiation environments is required. For example, in the SuperKEKB electron-positron collider and the Belle II experiment, a radiation field from electron and positron beam collision with a luminosity of $8 \times 10^{35} \text{ cm}^{-2}\text{s}^{-1}$ will be produced [5][6][7].

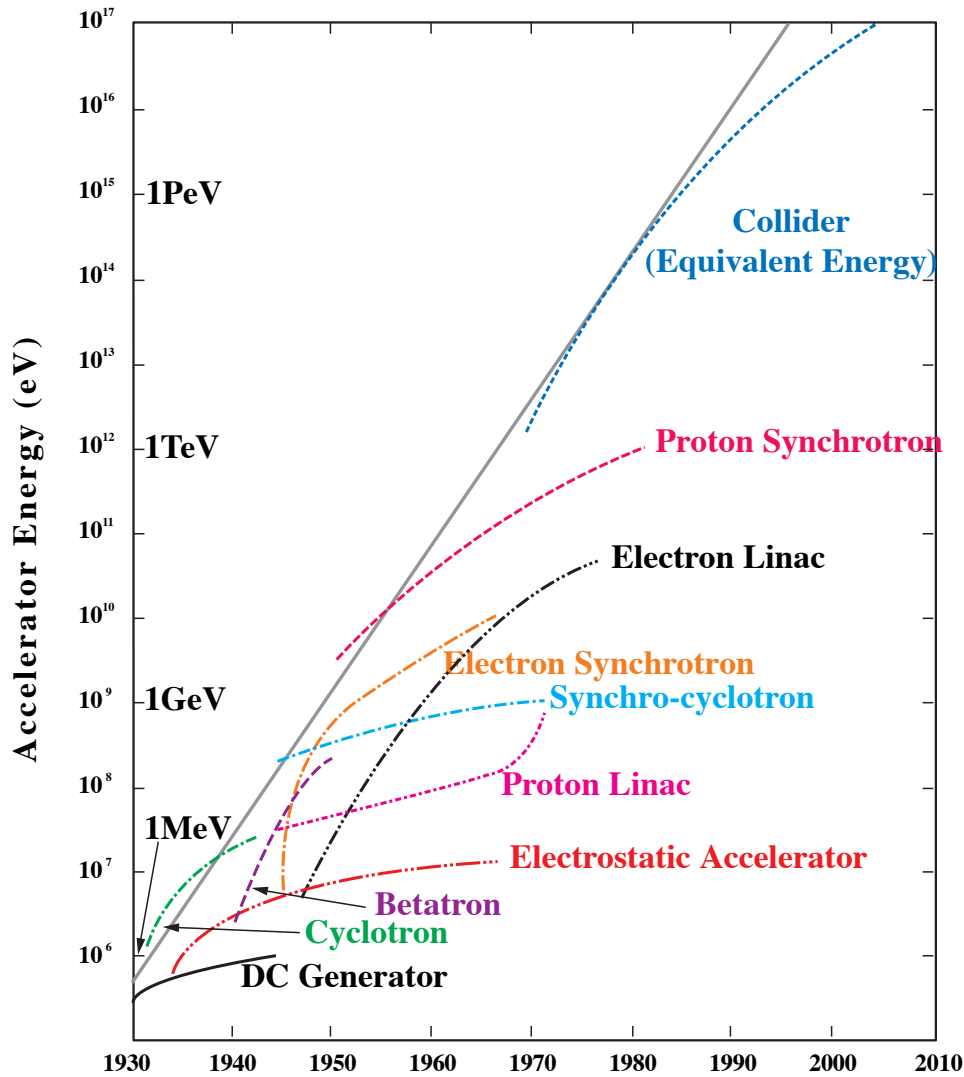


Figure 1.3: Livingston chart of accelerators [4].

Neutron detection in harsh radiation environments (including NPPs and accelerators) is challenging because of the limitations of neutron detectors, such as the poor robustness to radiation damage, low count rate capability, and improper operation at high temperatures and with a strong background of γ -rays. Therefore, the requirements for detector systems are as follows: a high radiation hardness, a low sensitivity to γ -rays, low sensitivities to light and temperature, a fast time response, and stable operation for thermal- and fast-neutron detection. According to these requirements, several candidate radiation detectors are compared in the following section.

1.2 Short review of neutron detectors used in harsh radiation environments

Table 1.1 presents the advantages, disadvantages, and radiation tolerances of different types of neutron detectors. The fission chamber has a low sensitivity to γ -rays and good radiation tolerance. However, the slow response leads to a high probability of pile-up effects at high dose rates. The organic scintillator and high-Z semiconductor have high sensitivities to γ -rays, and pulse-shape discrimination (PSD) is difficult at high dose rates owing to signal pile-up. The diamond detector has a fast response, a low sensitivity to γ -rays, and good radiation tolerance at dose rates of >4 MGy [8].

Table 1.1: Candidate sensors and their radiation tolerance.

Detectors	Advantage, disadvantage	Radiation tolerance
Fission chamber	High energy resolution Low sensitivity for BG- γ Good n/ γ discrimination Slow response Large detector size	Good tolerance
Organic Scintillator (NE213 etc.)	Fast response Good n/ γ discrimination High sensitivity for γ -rays Large detector size	Dose rate >9.9 Gy/h, Doesn't keep normal operation
High-Z Semiconductor (CdZnTe etc.)	High energy resolution High sensitivity for γ -rays	After 30 kGy irradiation, Out of order [9]
Diamond detector	Fast response Good energy resolution Low sensitivity for γ -rays Good n/ γ discrimination Small detector size	Operated stably after 4 MGy irradiation

Table 1.2 presents the properties of the diamond detector and other semiconductor detectors. SiC and diamond semiconductor detectors have recently emerged as attractive devices for harsh radiation environments.

Table 1.2: Properties of the diamond detector and other semiconductor detectors [2].

Material of semiconductor device	Si	Diamond	SiC(4H)	GaN	GaAs
Bandgap (eV)	1.12	5.48	3.27	3.39	1.42
ϵ value (eV)	3.6	13	7.8	8.9	4.6
Electron mobility (cm^2/Vs)	1500	1800	1000	1200	9200
Hole mobility (cm^2/Vs)	450	1500	115	~ 30	320
Dielectric constant	11.9	5.7	9.7	8.9	12.4
Thermal conductivity ($\text{W}/\text{cm}/^\circ\text{C}$)	1.5	20.9	4.9	1.3	0.46

A device with a large bandgap has a low leakage current, providing a stable state for variable temperature and illumination conditions. This corresponds to a low noise level during the measurement. The ϵ value indicates the pair creation energy, i.e., the minimum energy needed to create an electron–hole pair. A lower ϵ value corresponds to a larger signal; hence, a high signal-to-noise ratio can be achieved more easily. A high electron and hole mobility results in a fast response. For a device with a small dielectric constant, the particle detector has a small capacitance, corresponding to a low noise level. A high thermal conductivity corresponds to efficient heat transfer and a high radiation hardness [10].

As indicated by Table 1.2, the diamond detector has a large bandgap and high thermal conductivity, which results in good radiation tolerance. Silicon has a low electron–hole generation rate, which results in a high signal-to-noise ratio. The SiC detector can also be used as a high-radiation detector. The GaN detector has similar properties to the SiC detector but has a lower thermal conductivity. The GaAs detector has a high electron mobility and thus a fast response to electrons, but its radiation hardness is worse than that of the diamond detector.

In summary, the diamond detector is suitable for neutron detection in harsh radiation environments.

1.3 Overview of diamond detector

Diamond detectors have been widely used because of their excellent properties, such as their low leakage currents arising from their large bandgaps, their fast responses due to their high electron and mobilities and saturation drift velocities, and their high radiation hardness due to the low atomic number of Carbon.

Since the 1940s, diamond was proposed as a solid counter in a nuclear physics experiment [11]. Diamonds were used as neutron counters in nuclear reactors in the 1950s [12]. In the 1980s, diamonds have been grown via chemical vapor deposition (CVD) [13]. Polycrystalline diamonds and high-pressure, high-temperature (HPHT) diamonds have been used in radiation detectors since the 1990s [14][15].

1.3.1 Classification based on crystal structure

According to their crystal structures, diamond detectors can be classified as single-crystal diamond, heteroepitaxial CVD diamond, or polycrystalline CVD diamond. These types of diamonds are described in the following paragraphs.

Single-crystal diamond

The single-crystal diamonds currently available are natural diamonds, HPHT diamonds, and CVD diamonds.

The natural diamond detector consists of metal (Au/Ti/Mo/Au) contacts and a high pure natural diamond. This type of detector was widely studied in the 1970s [16]. However, because of its high costs and rarity, researchers turned their attention to the CVD and HPHT diamond detectors.

The HPHT diamond detector is produced via the HPHT method using a Ni-based sol-vent-catalyst [17][18]. Many studies on HPHT diamond detectors were performed in the 2000s.

The CVD diamond detector is produced via the aid of using a way of CVD. Owing to its excellent crystal uniformity, CVD diamond detector offer the good energy resolution and superior timing properties [19][20]. Its size of only a few square millimeters becomes a disadvantage. Therefore, the only option for the most demanding applications is the single crystal CVD diamond.

Heteroepitaxial CVD diamond

The heteroepitaxial CVD diamond detector is produced via epitaxial growth of diamond on substrates such as SiC, c-BN, BeO, Ni, Cu, and

graphite using CVD. The heteroepitaxial diamond detectors offer the advantage of large wafer size, and the disadvantage of the heteroepitaxial diamond is its high dislocation density [21].

Polycrystalline CVD diamond

The Polycrystalline CVD diamond is produced via CVD growth on the Si substrates or metals. Its advantages are excellent timing, large sensitive areas, and good tracking results[22][23]. The disadvantages are the charge trapping at grain boundaries and the non-uniformity of electric fields.

A single-crystal CVD diamond detector was proposed as a radiation detector with excellent radiation durability [24], high count rate capabilities (>1 MHz) [25], low electronic noise [26], and the capability of operating at high temperatures [27]. Because of these properties, the detector has been applied successfully as a beam loss monitor in harsh radiation environments, e.g., in the vicinity of beam pipes of high-energy, high-intensity proton–proton and electron–positron collision accelerators, i.e., the LHC and SuperKEKB, respectively [28][7][29].

1.3.2 Thermal-neutron detection

For thermal-neutron measurement, the combination of a charged-particle detector and a neutron converter has been developed [30]. For the thermal-neutron detection, a neutron converter must be used. Thus far, two converter materials— ^6Li and ^{10}B —have been proposed and tested. The reactions between these materials and neutrons are as follows:

$^6\text{Li}(n, \alpha)^3\text{H}$, with $E_\alpha = 2.05$ MeV, $E_{^3\text{H}} = 2.73$ MeV, and $Q = 4.78$ MeV, and

$^{10}\text{B}(n, \alpha)^7\text{Li}$, with $E_\alpha = 1.47$ MeV ; $E_{^7\text{Li}} = 0.84$ MeV, and $Q = 2.31$ MeV.

Figure 1.4 presents a schematic of the operation principle for a thermal-neutron detector using a ^6LiF converter layer.

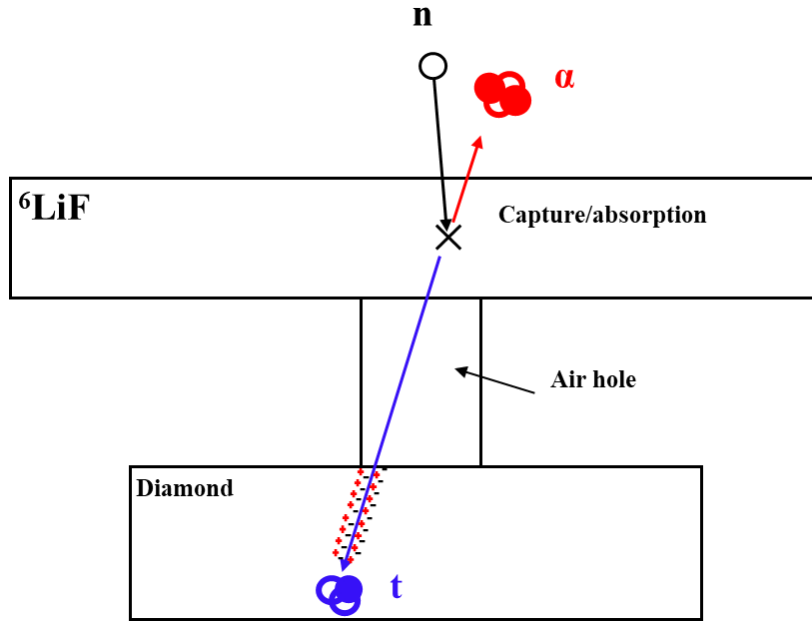


Figure 1.4: Operation principle of a thermal-neutron detector using a ${}^6\text{LiF}$ converter layer.

The ${}^{10}\text{B}(n, \alpha){}^7\text{Li}$ reaction offers a larger absorption cross section than the ${}^6\text{Li}(n, \alpha){}^3\text{H}$ reaction, while the neutron energies are <100 keV [31]. The α and ${}^7\text{Li}$ produced by the ${}^{10}\text{B}(n, \alpha){}^7\text{Li}$ reaction have lower energies than the α and ${}^3\text{H}$ produced by the ${}^6\text{Li}(n, \alpha){}^3\text{H}$ reaction. A lower energy is preferable for reducing the thickness of the diamond detector; however, it is not preferable from the viewpoint of the neutron sensitivity, because the thickness of the converter layer is limited by the large energy loss. However, the relatively high energy of tritons from the ${}^6\text{Li}(n, \alpha){}^3\text{H}$ reaction provides geometric separation between the neutron converter and the diamond detector, the advantages of which have been reported [32]. Hence, ${}^6\text{LiF}$ was selected as a neutron converter for the diamond detector in this study.

The thickness, layout, and reaction of the neutron converter were studied with regard to the neutron detection efficiency [33]. The combination has been successfully applied to the intense neutron fields around fission and fusion reactors [34][35][36]. For example, the combination was successfully applied in the vicinity of a research reactor with a thermal-neutron flux of 10^9 n/cm²/s [34]. Furthermore, it was tested for a neutron field induced by fusion plasma, with a total neutron yield reaching 10^{10} n/s [36]. Additionally, it is currently being used for hadron therapy [37].

1.3.3 Fast-neutron detection

For fast neutron measurement using diamond detectors, charged-particle production via neutron-induced nuclear reactions on carbon have been used [38]. The fast neutrons can interact directly with carbon nuclei. The type of neutron-induced reaction that occurs depends on the neutron energy [36]. The reaction channels of the $n + {}^{12}\text{C}$ reaction are presented in Table 1.3 [38].

Table 1.3: Reaction channels of the $n + {}^{12}\text{C}$ reaction.

Reactions Channels	Energy Threshold [MeV]	Q-value [MeV]
${}^{12}\text{C}(n, n){}^{12}\text{C}$	0	0
${}^{12}\text{C}(n, n'){}^{12}\text{C}^*$	4.8	–
${}^{12}\text{C}(n, \alpha){}^9\text{Be}$	6.182	-5.702
${}^{12}\text{C}(n, n')3\alpha$	7.886	-7.275
${}^{12}\text{C}(n, p){}^{12}\text{B}$	13.645	-12.587
${}^{12}\text{C}(n, d){}^{11}\text{B}$	14.887	-13.732

Another detection method for fast neutrons is the combination of a moderator and a thermal-neutron detector. Bonner sphere spectrometers (BSSs) are the most widely used systems for measuring neutron flux spectra [39][40]. The BSS consists of a thermal-neutron detector and polyethylene spheres of different diameters. Figure 1.5 shows examples of the moderators [41]. Commonly, the thermal-neutron detectors are placed at the centers of the moderated polyethylene spheres.



Figure 1.5: BSSs of different diameters [41].

In the recent years, the combination of Bonner spheres and diamond detectors has been studied for fusion neutron measurement. Z. M. Hu developed a BSS based on a designed diamond detector and evaluated its applicability to intense neutron fields in the EAST tokamak [42]. R. Bedogni investigated the neutron spectrum of Am–Be sources via Bonner sphere spectrometry [43].

1.3.4 Gamma rejection

The neutron field is always accompanied by γ -rays. Owing to the sensitivity of the diamond detector to γ -rays, the rejection of γ -ray-induced signals has been subjected in its actual application of neutron measurements. Thus, digital PSD methods have been employed, where a fast current-sensitive preamplifier was used to read out the detector pulses [35].

The pulse-shape analysis was based on the initial ionization profile of the incident particle in the diamond detector. For the charged particles, the electrons and holes produced by the ionization inside the diamond detector are distributed close to the incident surface region. Thus, the drift of electrons and holes generated by charged particles from the neutron converter results in a rectangular pulse shape for a diamond detector having a large thickness relative to the charged-particle range. However, for gamma irradiation, the Compton electrons travel through the whole diamond, generating electron–hole pairs homogeneously. Thus, their drift results in a triangular pulse shape. Figures 1.6 and 1.7 show the measured, theoretical, and ideal signals induced by a charged particle and an electron, respectively, for a 500- μm -thick diamond detector with an ^6LiF neutron converter [35].

The differences in the durations of current pulses of the same charge are used to discriminate between neutron and gamma events. A system for this is commercially available [44]. An improved PSD technique was developed via using of the full width at half maximum (FWHM) and the full width at 2/3 of the peak height (FW2/3 PH) [45].

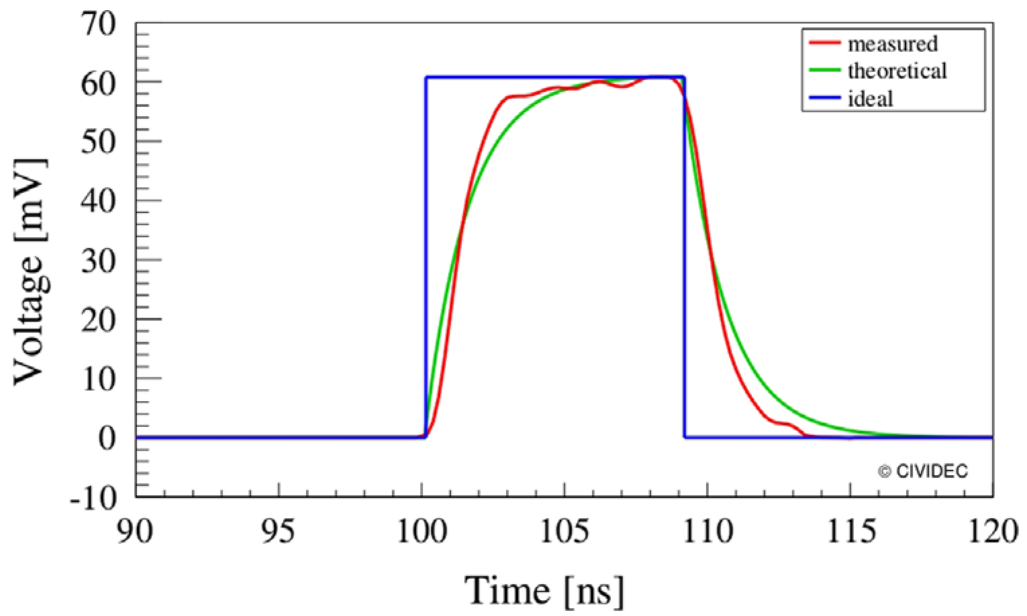


Figure 1.6: Rectangular pulse shape of an alpha particle [35].

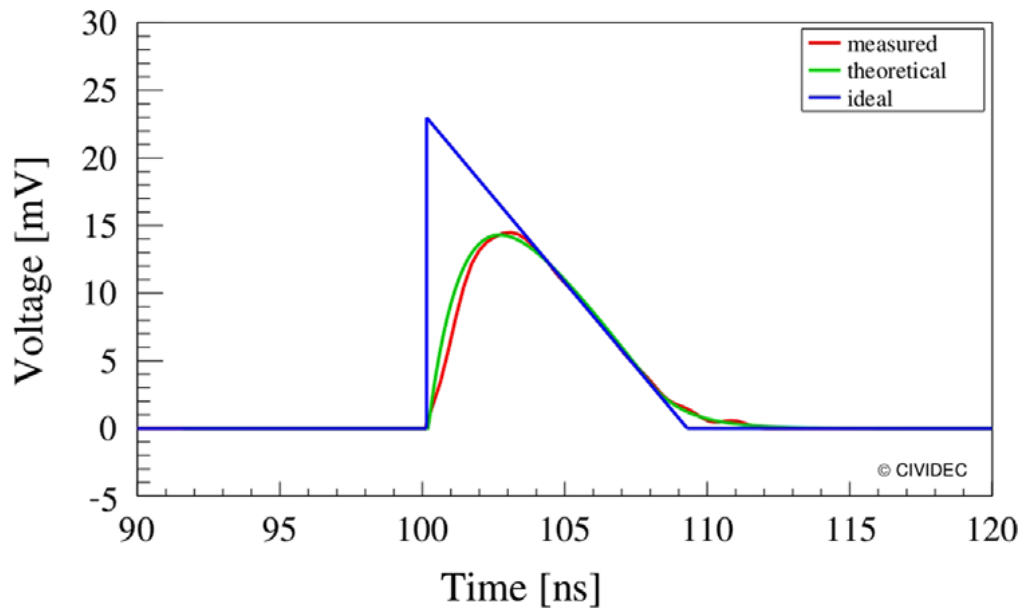


Figure 1.7: Triangular pulse shape for an electron [35].

In addition to the PSD methods, γ -rays can be easily distinguished via pulse-height discrimination. The energy deposited by charged particles from the neutron absorption reaction generally exceeds that deposited by γ -rays. However, the discrimination is limited when the amplitude of the γ -ray pulses becomes comparable to that of the neutron-induced pulses. This occurs in cases of high-energy γ -rays or the pulse pile-up of multiple gamma events. The probability of pulse pile-up is determined by the durations of the output pulses, which correspond to the charge-collection time inside the detector and the signal readout process. Reducing the detector thickness reduces the energy deposited by γ -rays and the charge-collection time. Because the amount of energy deposited by γ -rays and the probability of the pulse pile-up effect depend on the thickness of the detector, the sensitivity of a diamond detector to γ -rays can be minimized by reducing the detector thickness.

In this paper, I propose a methodology in which the neutron-gamma separation is enhanced by decreasing the gamma-pulse height through a reduction in the thickness of the diamond detector.

1.3.5 Readout system

For low-flux neutron detection with a strong gamma background, the common analogue signal readout system that consists of a charge-sensitive preamplifier is unsuitable, because it causes a significant signal pile-up effect, which makes gamma events overlap with neutron events. Thus, I employed a fast current-sensitive preamplifier and a waveform digitizer to minimize the pulse pile-up.

The transient-current technique (TCT) has been used for studying the properties of semiconductor detectors [46][47]. It is commonly used in research on the charge-carrier transport mechanism, interface trap characterization, and the electric-field distribution [48][49] owing to its direct time-resolved recorded current pulse shapes. The measurement principle of the TCT is as follows: the free carriers are generated by the incident charged particle in the detector, and then a current is induced on the electrodes by the drift of the free carriers in the detector under an applied electric field. The TCT can be used to directly measure the transient displacement current. A TCT-Acqiris digital system consists of a fast current-sensitive preamplifier (CIVIDEC C2-TCT) with a 2-GHz bandwidth and 40-dB gain and a 10-bit waveform digitizer (Agilent-Acqiris DC282), which has a bandwidth of 1.5 GHz and a sampling rate of 2 GS/s.

1.4 Objective of this study

The objective of this study was to develop a high-flux capability neutron detection system using a CVD diamond detector with a simple method for neutron/gamma discrimination in harsh radiation environments.

To achieve this, a methodology for enhancing the simple neutron-gamma separation by decreasing the gamma-pulse height through a reduction in the thickness of the diamond detector was developed. The performance of diamond detectors with different thicknesses was evaluated for thermal-neutron measurement with separation of γ -rays through response calculation. By analyzing the simulated energy-deposition spectrum, the optimal thickness was determined for neutron-gamma separation. I customized a diamond detector according to the results and then experimentally tested it in comparison with a standard diamond detector.

Because the customized detector was studied for the first time, a series of tests were performed to evaluate the current-voltage (I-V) characteristics, leakage current, and energy resolution for alpha-particles.

The γ -ray irradiation experiments were performed at dose rates ranging from 0.693 to 107 Gy/h with a conventional analog circuit to confirm the pile-up effect. To minimize the pulse pile-up events, a signal readout system was employed for measuring the transient current signals with durations of a few nanoseconds. To validate the readout system, tests were performed for alpha-particles from a mixed alpha-source (^{148}Gd , ^{241}Am , ^{244}Cm), γ -rays from a ^{60}Co source with a dose rate of 107 Gy/h, and a thermal-neutron source using the KEK graphite pile with ^{241}Am (37 GBq)-Be.

The developed detector was used for thermal- and fast-neutron measurement at an electron accelerator facility. The thermal-neutron measurement test was performed in the target room of the electron LINAC at the Institute for Integrated Radiation and Nuclear Science, Kyoto University (KURNS). With discrimination of γ -rays, the thermal-neutron flux was determined for a 30 MeV–3.5 μA electron beam incident on a tungsten target at the center of a 20-cm-thick water tank. The fast-neutron measurement test was performed behind the beam dump of the superconducting linear accelerator test facility (STF) at KEK. To obtain the neutron spectrum, a BSS with five moderator diameters—0 (bare), 40, 70, 110, and 190 mm—was used with the diamond detector. The Bonner sphere response functions were simulated using the Particle and Heavy-Ion Transport Code System (PHITS) Monte Carlo code. The neutron spectrum was obtained through the response with an unfolding process.

Chapter 2

Simulation analysis of thickness of diamond detector

Figure 2.1 shows the spectrum of thermal neutrons in a 500- μm -thick diamond detector [35]. Three components are observed: alpha, gamma, and tritons. The alpha and triton events arise from the ${}^6\text{Li}(n, \alpha){}^3\text{H}$ reaction, and the gamma events arose from the background and neutron capture reaction. The triton peak can be used for neutron measurement because it has a higher energy and energy resolution than the alpha peaks. If the energy of the γ -rays exceeds 2 MeV, pulse-height discrimination is impossible owing to the overlap of the gamma and triton components.

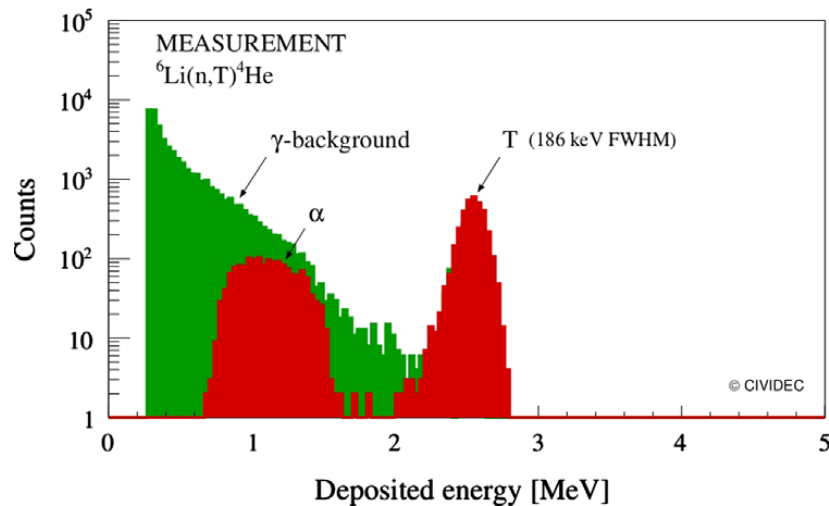


Figure 2.1: Spectrum of ${}^6\text{Li}(n, \alpha){}^3\text{H}$ reaction measured using the Cx Spectroscopic Shaping Amplifier with a 500 μm diamond detector [35].

To enhance the separation between the gamma and neutron events in the pulse-height spectrum, the pulse heights of γ -rays should be compared with those of charged particles from the converter. For maximizing the pulse heights of charged particles, the thickness of the diamond detector should exceed the maximum range of the particles.

The range of a charged particle depends on its initial energy and the converter thickness. The range of a triton with 2.73 MeV of energy in diamond with a density of 3.5 g/cm³ was calculated to be 21 μm [50]. Considering the manufacturing accuracy, a thickness of 25 μm was selected to prepare an actual detector for an experimental evaluation of its performance.

Thus, for satisfying the requirement of n/ γ discrimination, it is necessary to optimize the thickness of the diamond detector to prevent the overlap of the gamma and triton components.

To confirm the importance of the thickness of the diamond detector for n/ γ discrimination, the responses of diamond detectors of different thicknesses to neutron and gamma sources were simulated via the PHITS.

The PHITS Monte Carlo code was used for calculating the detectors' responses to neutrons and γ -rays [51]. The t-deposit tally for the cell of the diamond crystal was used to quantify the energy deposition.

2.1 Structure of diamond detector in simulation

Geometric models of the simulated diamond detector and its housing are shown in Fig. 2.2. All the materials surrounding the diamond crystal were included in the simulations, except the connector for the output signal and its mount, as they are far from the diamond crystal. The material composition and density of the diamond detector and housing used in the simulations are presented in Table 2.1.

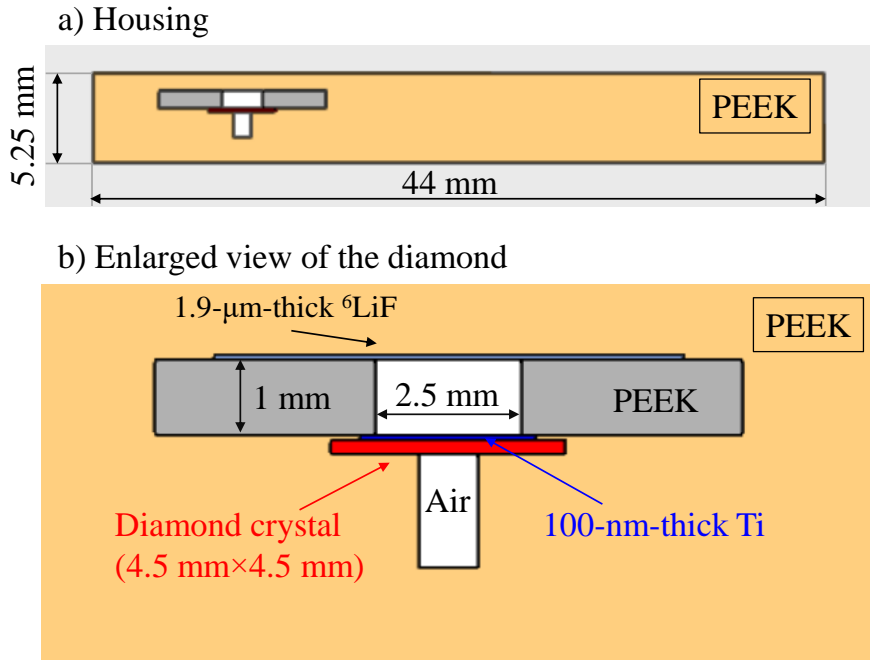


Figure 2.2: The simulation model of the CVD diamond detectors. (a) Overall and (b) enlarged views of the sensor part.

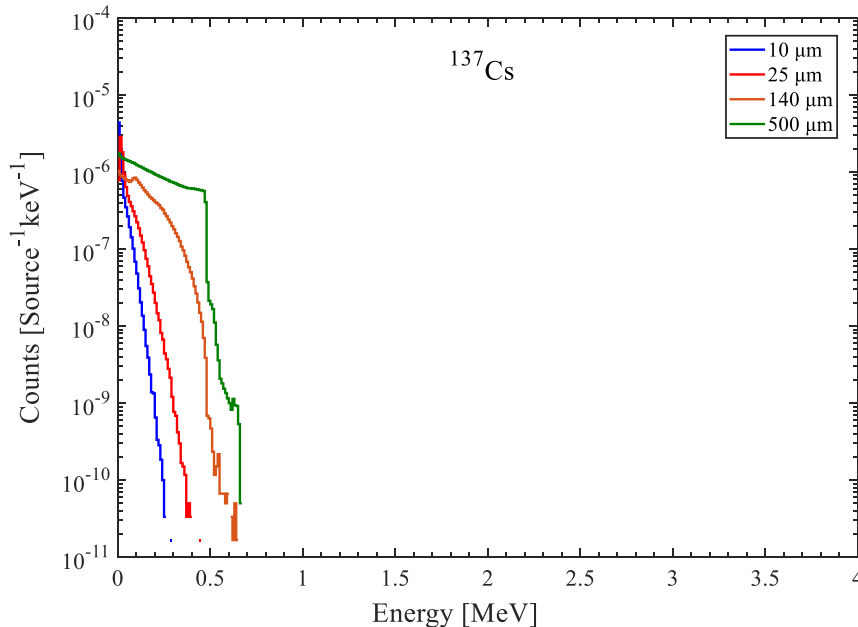
Table 2.1: Material compositions and densities (diamond detector and its housing) used in the PHITS simulation.

Material	Element	Density [g/cm ³]	Mass ratio
Diamond	C	3.5	1
Ti electrode	Ti	4.5	1
Air	N	0.0012	0.755
	O		0.232
	Ar		0.013
⁶ LiF convertor	⁶ Li	2.6	0.228
	⁷ Li		0.014
	F		0.758
PEEK cover layer (Polyetheretherketone)	Cu	1.46	0.1855
	Ni		0.0217
	Au		0.0012
	C		0.6266
	H		0.0332
	O	0.1318	

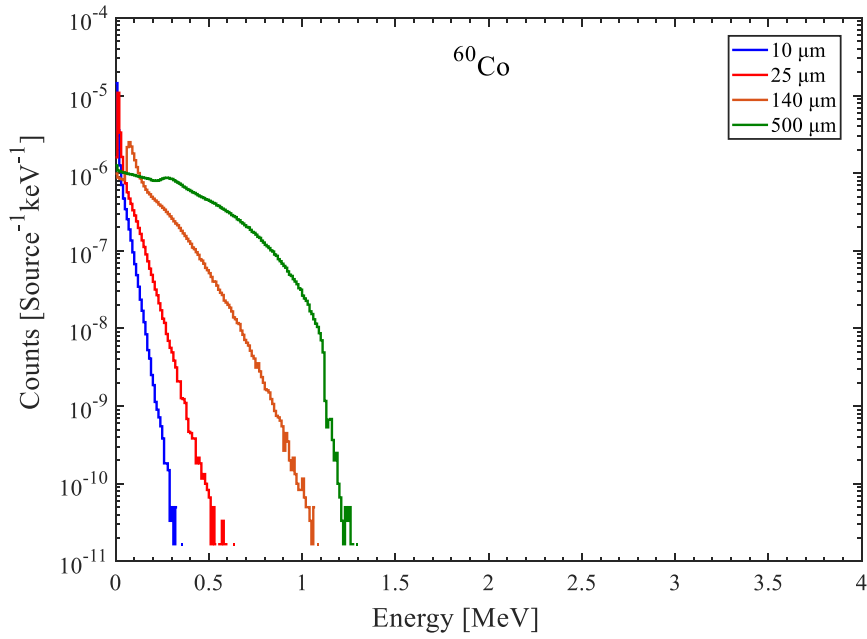
2.2 Response of diamond detector with gamma-source

In the PHITS code, the transport of photons, electrons, and positrons is simulated using the EGS5 algorithm. In the γ -ray calculations, the cutoff energy was set as 1 keV for photons, electrons, and other ions. To investigate the responses of the detectors to higher-energy γ -rays, in addition to ^{137}Cs and ^{60}Co , the responses of the detectors to 2-, 4-, and 10-MeV γ -rays were also calculated. In these simulations, the responses were calculated for detectors of four different thicknesses (10, 25, 140, and 500 μm) within the same housing as the actual 25- and 140- μm -thick detectors. The thickness of 500 μm is the common thickness of commercial diamond detectors, and the 10- μm -thick detector is an example of a very thin detector. A parallel source covering the area of the entire detector for γ -rays was considered in these calculations.

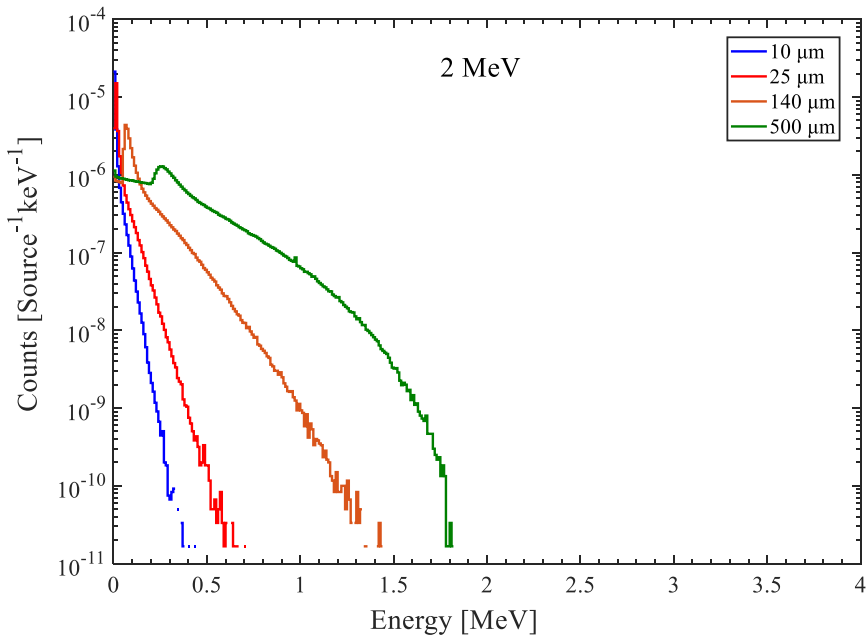
Figure 2.3 presents the calculated energy-deposition spectra of the diamond detectors with different thicknesses (10, 25, 140, and 500 μm) with pencil parallel beams of γ -rays from ^{137}Cs and ^{60}Co and photons having energies of 2, 4, and 10 MeV. The thicknesses of 10 and 500 μm were selected to represent detectors thinner than 25 μm and the typical semiconductor wafer thickness used for PSD, respectively [35].



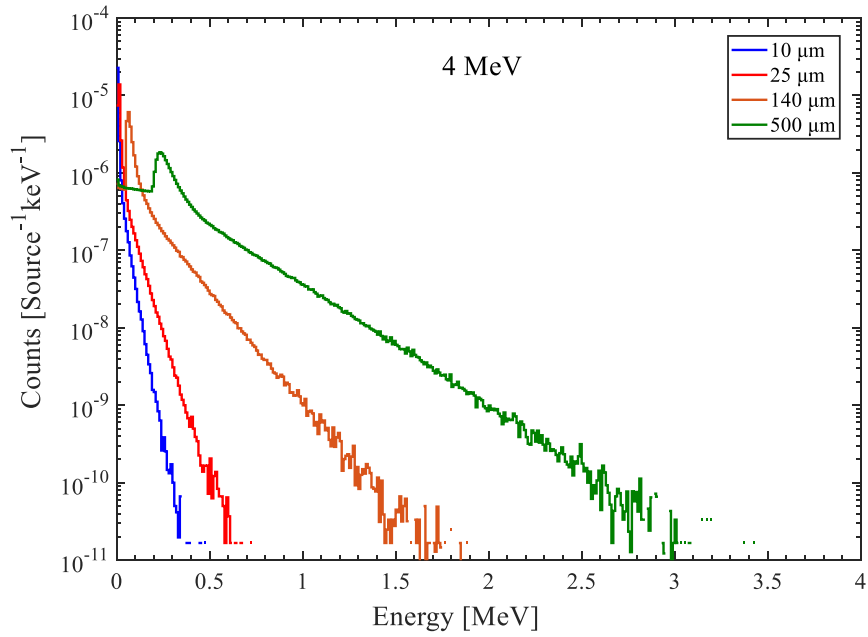
(a) Gamma source of ^{137}Cs .



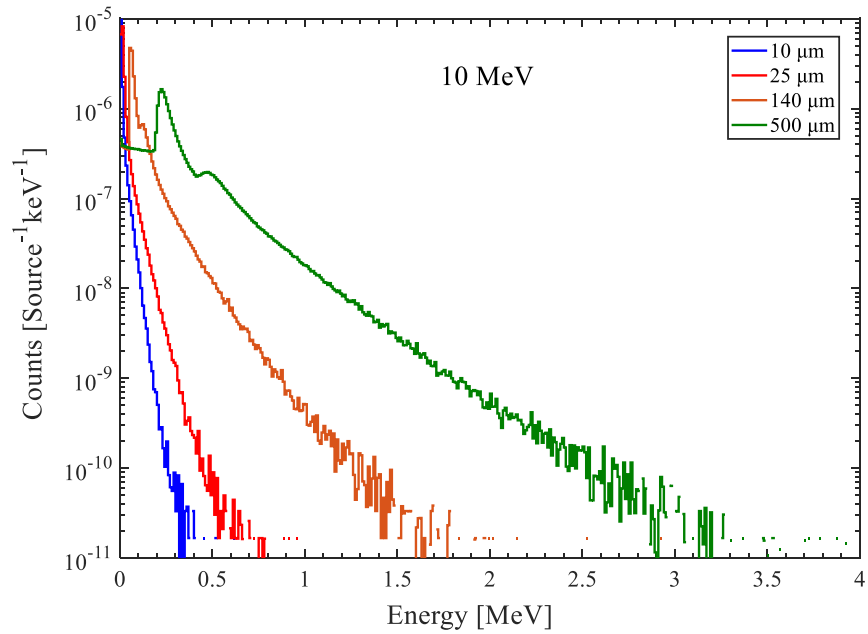
(b) Gamma source of ^{60}Co .



(c) Gamma source of 2 MeV.



(d) Gamma source of 4 MeV.



(e) Gamma source of 10 MeV.

Figure 2.3: The simulated spectrum of the diamond detector with different thickness and its housing for five photon energies.

The figure indicates the following: (1) the maximum amount of energy deposited increased with the detector thickness, (2) the energy-deposition spectra of the 10- and 25- μm -thick detectors appeared insensitive to changes in the incident photon energy, and (3) peaks at approximately 0.1 and 0.25 MeV were observed for the 140- and 500- μm -thick detectors with photon energies of >2 MeV. According to the results of additional simulations with and without the PEEK cover surrounding the detector, these peaks corresponded to backscattering photons.

Figure 2.4 shows the total number of photons for each energy level and thickness as a function of the energy of the incident γ -rays. As expected, the total number of counts increased with the detector thickness for all the energies. However, when the energy of the incident γ -rays was >2 MeV, the differences in the total counts per source among the four thicknesses decreased with an increase in the photon energy. For example, when the energies of the incident γ -rays were 0.662 and 10 MeV, the differences between the 500- and 10- μm -thick detectors were 80% and 30%, respectively. This indicates that the γ -ray sensitivity and the difference in the total counts per source between the diamond thicknesses decrease with the increasing gamma energy.

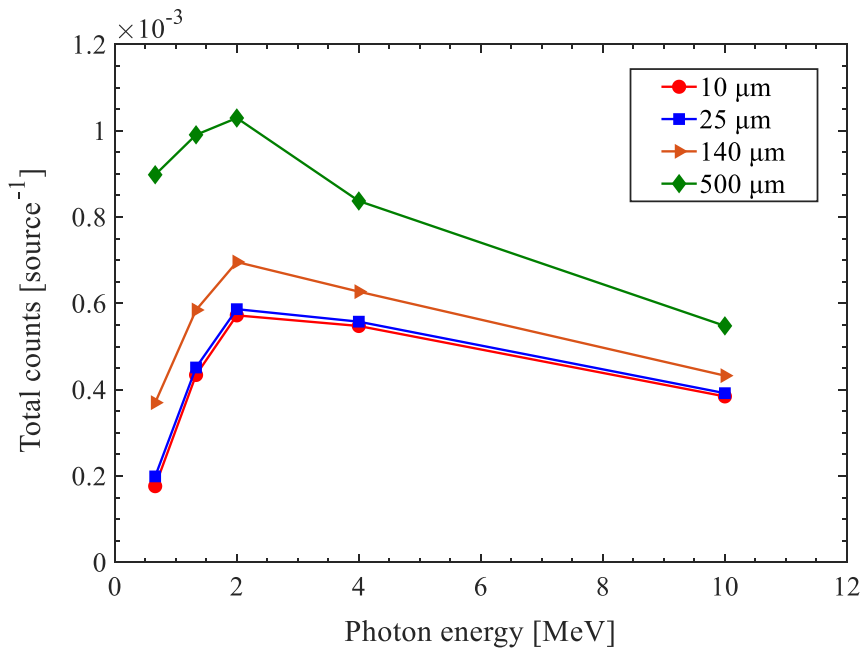


Figure 2.4: Total counts per source for diamond detectors with different thicknesses and different gamma-sources.

However, the total counts rapidly increased with the energy of the γ -rays up to 2 MeV and then decreased. The reason for this trend was the interference from γ -rays scattered from the detector housing. According to the cross section of the interaction between the γ -rays and the diamond, the total number of counts should have decreased with the increasing energy of the γ -rays regardless of the detector thickness. The results of additional simulations with and without the PEEK cover surrounding the detector indicated that the peak corresponded to recoil electrons from the PEEK cover. This indicates that the choice of the detector housing material is important for reducing the sensitivity of the detector to γ -rays.

Although the total numbers of events were almost identical among the four detectors with different thicknesses for 10-MeV photons, the maximum deposition energies differed significantly. To evaluate these differences quantitatively, the energy gives 99.99% of total events ($E_{99.99}$) is defined as follows:

$$\int_0^{E_{99.99}} C(E)dE = 0.9999 \times \int_0^{\infty} C(E)dE \quad (2.1)$$

where $C(E)$ [counts/MeV] represents the number of counts for a deposition energy of E [MeV].

Figure 2.5 shows the results for $E_{99.99}$ with respect to the energy of the incident γ -rays. The dependence of $E_{99.99}$ on the energy of the γ -rays is clearly observed. For the 10- and 25- μm -thick diamond detectors, $E_{99.99}$ was almost constant and remained below 0.5 MeV. For the 140- and 500- μm thick detectors, $E_{99.99}$ continuously increased to approximately 2 and 4 MeV, respectively, and then decreased. Even for the 500- μm -thick diamond detector, $E_{99.99}$ remained below 3 MeV. This indicates that a low sensitivity to γ -rays was achieved, as $E_{99.99}$ remained below the energy of tritons (2.73 MeV). The definition of $E_{99.99}$ implies that 0.01% of photons may exceed this energy. Some of them can overlap with triton events if the energy loss in the converter and the energy resolution of the detector are taken into account. This may hinder the separation of neutrons and γ -rays—particularly under a low neutron flux and an intense γ -ray field.

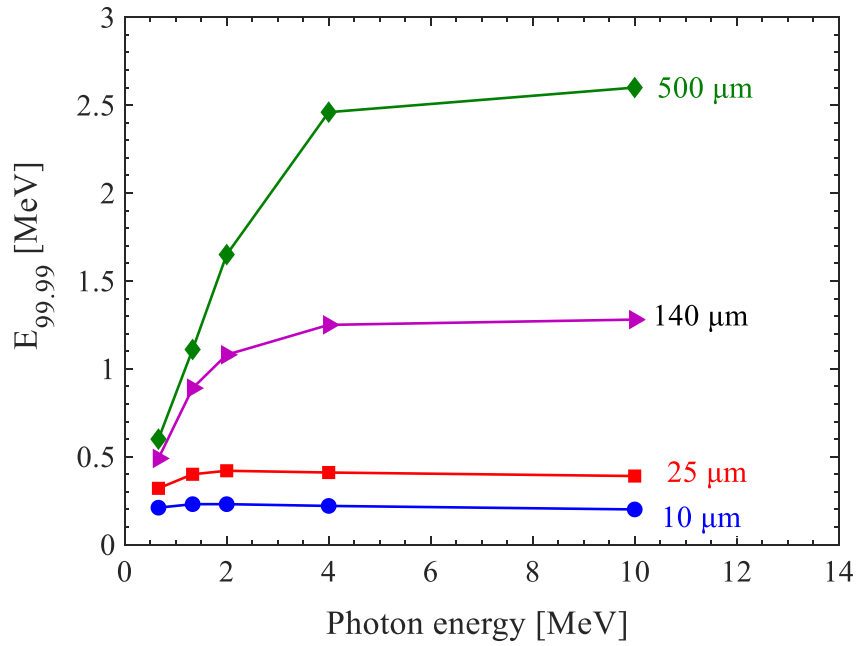


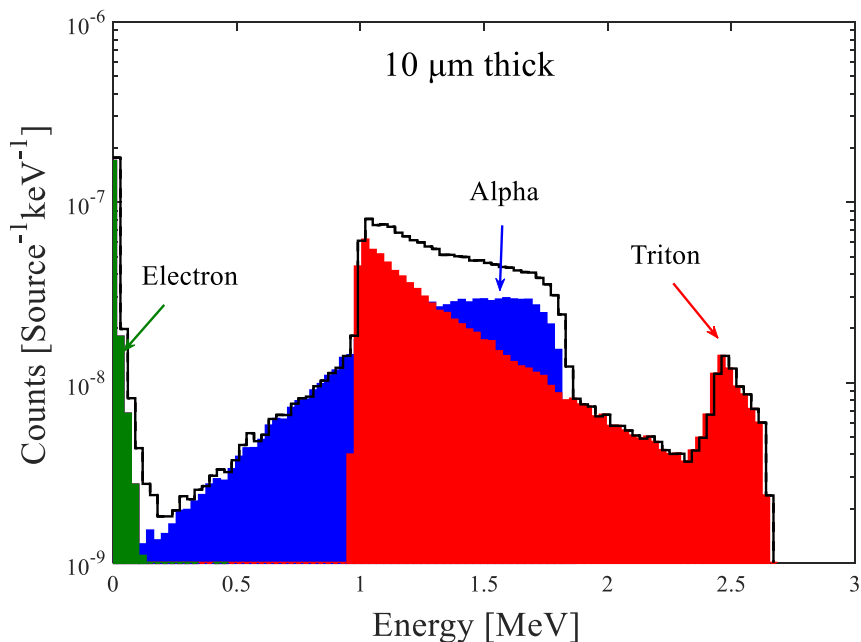
Figure 2.5: $E_{99.99}$ as a function of incident photon energy for diamond detector with different thicknesses.

The foregoing results indicate that reduction of the detector thickness is effective for reducing the photon sensitivity and the maximum deposition energy and thereby enhancing the separation between photon and neutron events.

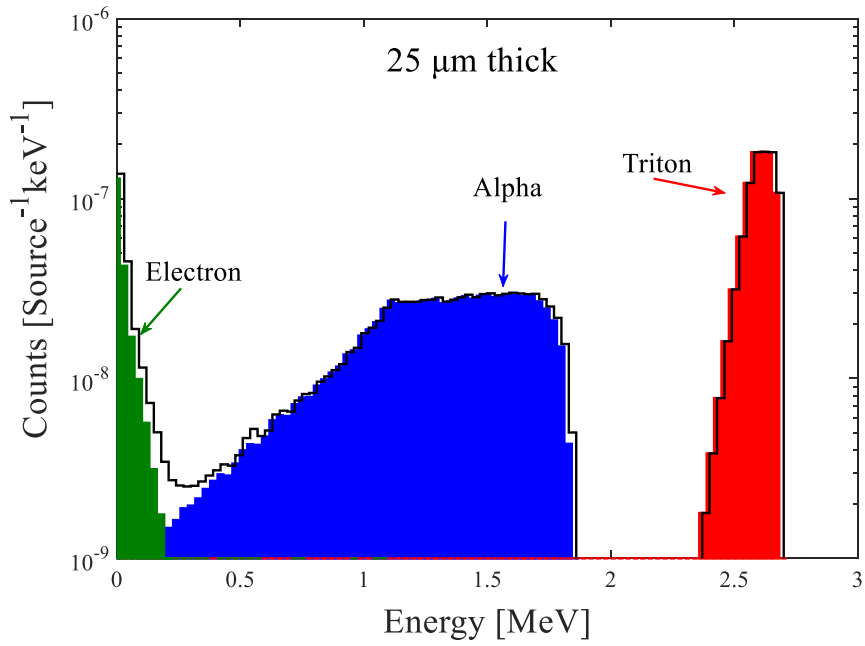
2.3 Response of diamond detector with neutron-source

In the neutron calculations, a cutoff energy of 10^{-4} eV was used for the transport of neutrons, whereas a cutoff energy of 10 keV was used for photons, electrons, and other ions. In the PHITS code, transport of neutrons below 20 MeV is based on the nuclear data library JENDL-4.0 and the Event Generator Mode (version 2). In these simulations, the responses were calculated for detectors of four different thicknesses (10, 25, 140, and 500 μm) within the same housing as the actual 25- and 140- μm -thick detectors. A parallel source covering the area of the entire detector for γ -rays was considered in these calculations.

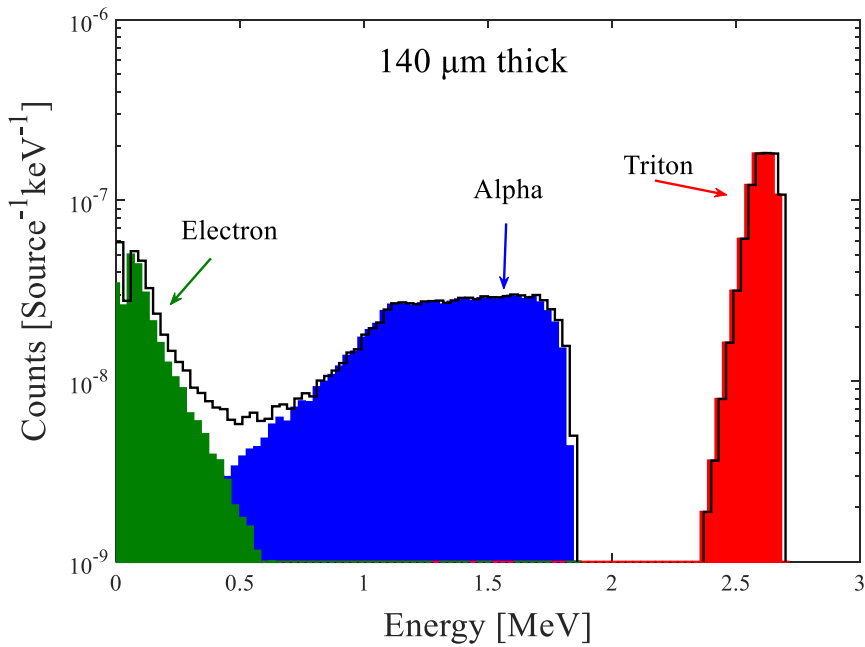
Figure 2.6 shows the simulated responses. The spectra consisted of a triton peak component, a continuous component of alpha-particles and electrons. A prominent peak at 2.7 MeV corresponding to tritons was observed in the spectra of the 25-, 140-, and 500- μm -thick detectors but not the 10- μm -thick detector. The electron distributions differed among the four detectors owing to the different sensitivities to the γ -rays. The alpha-particle components of the spectra were identical among the different thicknesses.



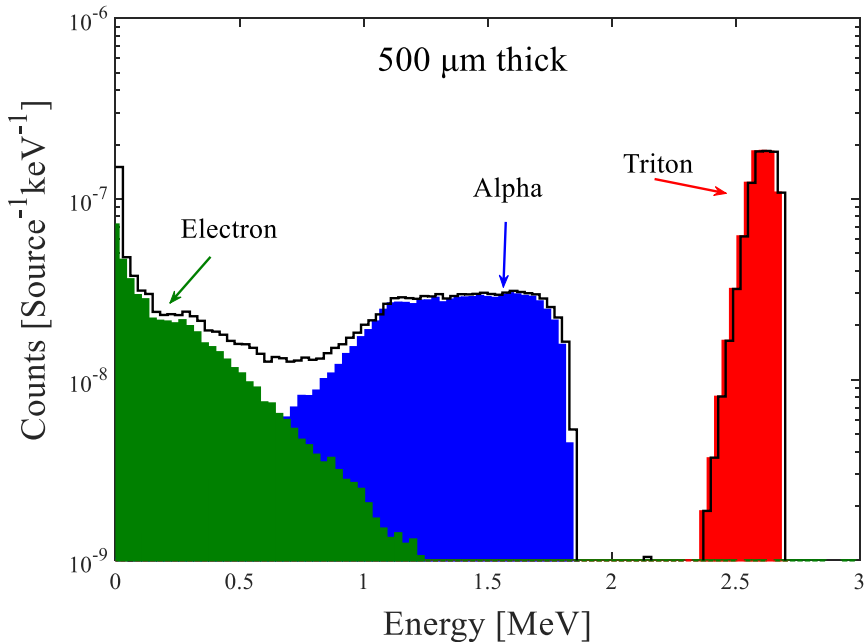
(a) 10- μm -thick diamond detector.



(b) 25- μm -thick diamond detector.



(c) 140- μm -thick diamond detector.



(d) 500- μm -thick diamond detector.

Figure 2.6: Simulated spectra for diamond detectors with different thicknesses and a neutron source.

For the 10- μm -thick detector, the triton and alpha-particle components significantly overlapped, because the detector was too thin to fully stop the tritons. In this case, by setting a threshold of <1 MeV, the significant parts of the triton and alpha components can be used for thermal-neutron flux measurement with a reduction in the gamma contribution. Using this method, it is easy to achieve gamma-rejection owing to the low sensitivity to γ -rays. However, this configuration has the following disadvantages: (1) the pulse height is reduced, and the noise interferes with the detection; (2) the charge-collection efficiency (CCE) is worsened owing to the low energy, as discussed in Section 3.2.2; and (3) it is difficult to perform energy calibration and determine whether there are contributions from other particles owing to the loss of the typical peak of tritons.

For the 25-, 140-, and 500- μm -thick detectors, the main parts of the triton peak and the alpha-particle component were identical. The triton distribution consisted of one prominent peak at 2.7 MeV and continuous low-energy components. The reason for the continuous energy components was the large energy loss due to the various pathways traveled by the particles to the diamond crystal. The low-energy region accounted for 2.3% of the count rate when the threshold was set as 2.3 MeV. Consequently, the triton peak can be

used for thermal-neutron measurement without the gamma contribution. For thermal-neutron detection, the detector thickness should exceed the range of the 2.73-MeV tritons in diamond, which is approximately 21 μm . This implies that the thickness of 25 μm is close to the optimal value for achieving a low sensitivity to γ -rays while maintaining the full deposition energy of neutron absorption reaction products.

On the low-energy side of the spectra, contributions from electrons were observed that were due to γ -rays from the thermal-neutron capture reaction in materials surrounding the diamond detector. The maximum energy of the electron component increased with the thickness of the diamond crystal.

The simulated results for the responses of the four thicknesses detectors indicate that 25 μm is close to the optimal thickness for achieving a low sensitivity to γ -rays while maintaining the full deposition energy of neutron absorption reaction products.

Chapter 3

Experimental characterization of diamond crystals

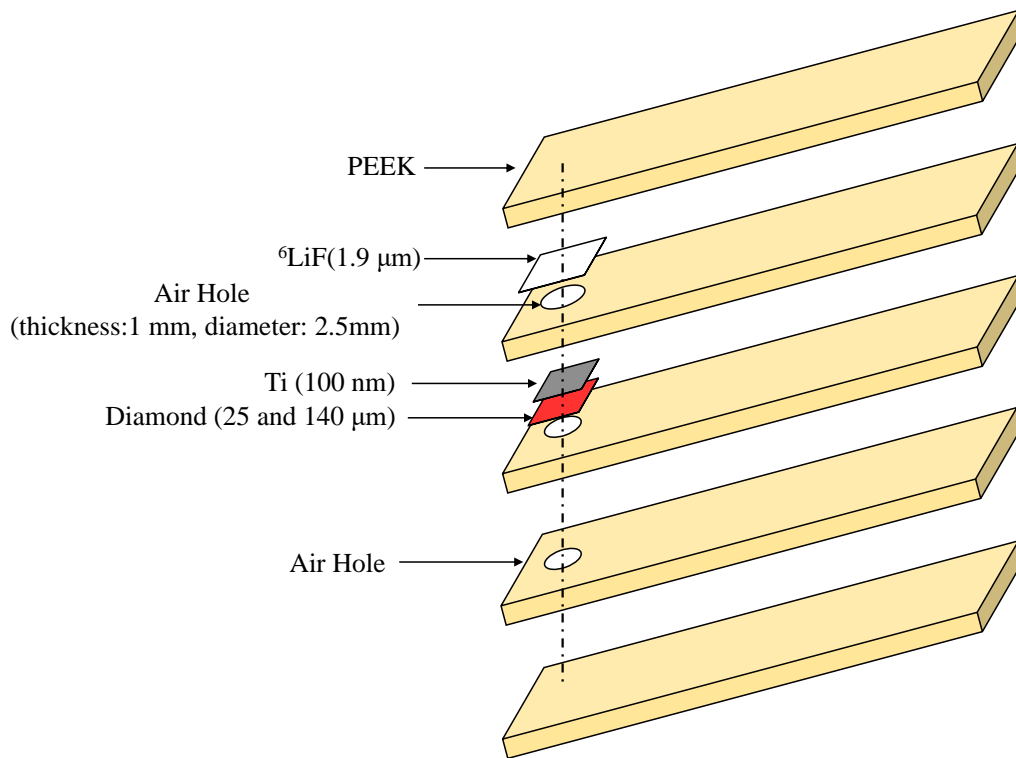
25- and 140- μm -thick CVD diamond detectors were acquired, and their performance was experimentally evaluated. First, the basic properties of the detectors were tested by measuring the current–voltage (I–V) curves and CCE. Then, the detection efficiency for thermal neutrons and the pulse-height response for neutrons and γ -rays were measured. In this section, the apparatus used for these tests is described in detail.

The CVD diamond detectors with different thicknesses were prepared by CIVIDEC. The 25- μm -thick detector was prepared specially according to the aforementioned design. The 140- μm -thick detector was selected from the product catalogue (model number B6-C) [44].

Figure 3.1 shows the photograph and structure of the detector housing. The packages of the 25- and 140- μm -thick diamond detectors were identical except for the thicknesses. The area of the diamond crystals was $4.5 \times 4.5 \text{ mm}^2$. Additionally, 100-nm-thick titanium electrodes were attached to the cathodes of the crystals. The housing contained a 95% enriched ${}^6\text{LiF}$ thermal-neutron converter with a thickness of 1.9 μm and a PEEK plate with a 2.5-mm-diameter circular opening window for mounting the ${}^6\text{LiF}$ layer and the diamond with a distance of 1 mm. The ${}^6\text{LiF}$ converter side of the diamond detector was connected to the ground and functioned as the cathode when a positive voltage was applied to the other side. The size of the entire package was $56.25 \times 9.5 \times 5.25 \text{ mm}^3$. It consisted of five PEEK plates metallized with Cu, Ni, and Au.



(a) Photograph of the CVD diamond detectors.



(b) Structure of the CVD diamond detectors.

Figure 3.1: The photograph and structure of the CVD diamond detectors.

3.1 Current–voltage characteristics

The leakage current of the detectors is important, as it determines the level of electronic noise. The I–V curves of the detectors were measured using an experimental setup consisting of a source measure unit (SMU) that supplied the voltage and measured the current with a high accuracy of 0.012%, along with a vacuum chamber. The detector was placed inside the vacuum chamber. The bias voltages were varied from -40 to 40 V and -120 to 120 V for the 25- and 140- μm -thick detectors, respectively. These voltage spans corresponded to the maximum electric-field strengths of ± 16 and ± 8.6 kV/cm in the 25- and 140- μm -thick detectors, respectively.

Figure 3.2 shows the I–V curves of the 25- and 140- μm -thick diamond detectors. The I–V curve of the 140- μm -thick detector exhibited a nonlinear trend, indicating a Schottky contact. The Schottky contact is similar to the p–n junction and shares many of its characteristics. In contrast, the I–V curve of the 25- μm -thick detector exhibited a linear trend, indicating an ohmic contact. A low-resistance ohmic contact allows carriers to flow easily in both directions and is critical for the accuracy and reliability of a diamond detector.

From the I–V curve, the average intrinsic resistivity of the 25- μm -thick detector was estimated to be $1.79 \times 10^{14} \pm 6.97 \times 10^{13} \Omega \cdot \text{cm}$. The intrinsic resistivity was sufficient for obtaining a low level of electronic noise.

The leakage current of the 140- μm -thick detector remained below 20 pA for electric-field strengths ranging from -2 to 5 kV/cm. For the 25- μm -thick detector, the leakage current was <10 pA for electric-field strengths ranging from -4 to 7 kV/cm. These leakage currents are lower than those reported in the literature [26][52].

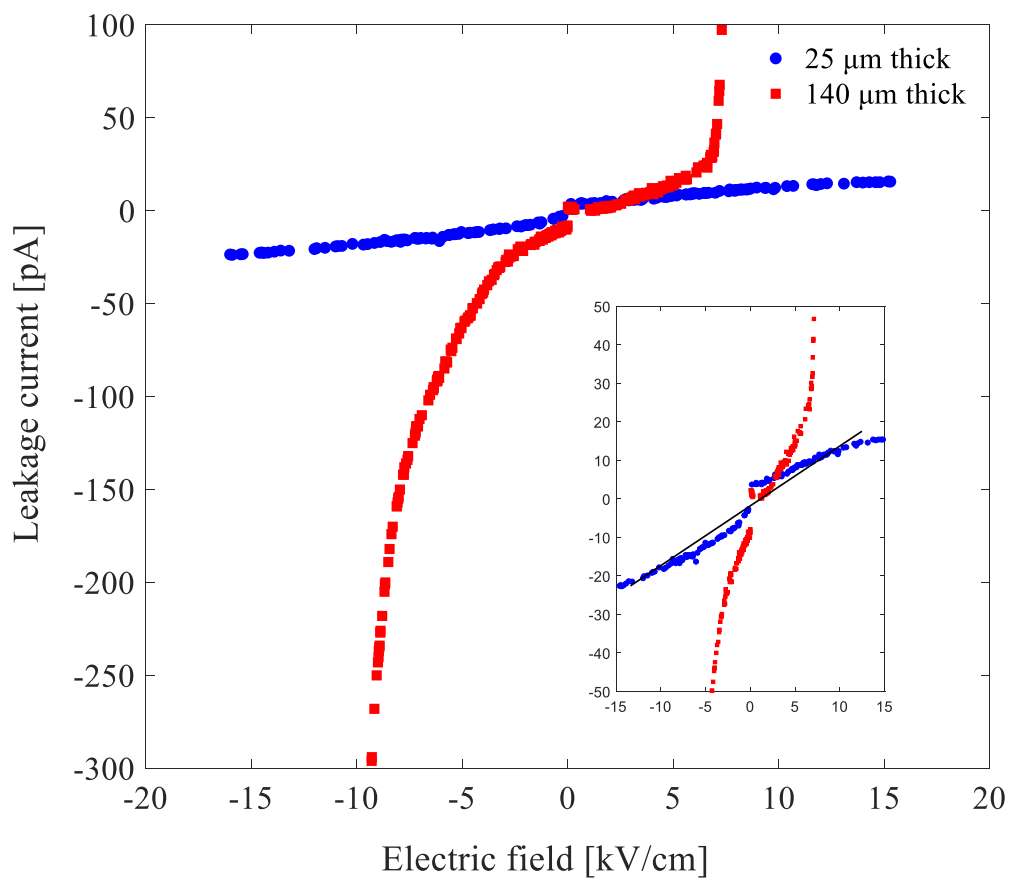


Figure 3.2: I–V curves of the 25- and 140- μm -thick diamond detectors. The straight line is the linear fitting line for the 25- μm -thick detector.

3.2 Charge collection efficiency (CCE)

The measurement system is illustrated in Fig. 3.3. The CCEs of the detectors were measured using a mixed alpha-source, which was composed of ^{148}Gd (3.183 MeV), ^{241}Am (5.486 MeV), and ^{244}Cm (5.805 MeV), in a vacuum chamber. The radioactivity was 292 ± 10 , 367 ± 13 , and 325 ± 11 Bq for the alpha-sources of ^{148}Gd , ^{241}Am , and ^{244}Cm , respectively. The source deposited on the platinum backing was sealed by a thin Au coating of $100 \mu\text{g}/\text{cm}^2$. The detectors were individually exposed to the alpha-particles from the anode side. One PEEK plate was removed to allow the alpha-particles to reach the diamond surface.

For the signal readout system, the detectors were connected to a charge-sensitive preamplifier (CAEN A1422), a shaping amplifier (CAEN N968) with a shaping time constant of $0.5 \mu\text{s}$, and a computer-based multichannel analyzer (MCA 8000D) to record the pulse-height distribution. The CCEs were determined from the peak channels of the alpha-particles as a function of the electric-field strength. Assuming a CCE of 100% [53], a silicon PIN photodiode (S3590-09, Hamamatsu Photonics K.K.) was used as a reference for measuring the CCEs of the diamond detectors. A precision nuclear pulse generator was used to determine the gradient and y-intercept value for the diamond and silicon detectors.

The following calibration formula was used for the CCE values of the diamond detectors [10]:

$$CCE_{Dia} = \frac{Peak_{ch_{Dia}} - C_{Dia}}{Peak_{ch_{Si}} - C_{Si}} \times \frac{\epsilon_{Dia}}{\epsilon_{Si}} \times \frac{m_{Si}}{m_{Dia}} \times \frac{E - \epsilon_{loss_{Si}}}{E - \epsilon_{loss_{Dia}}} \times 100\% \quad (3.1)$$

where $Peak_{ch_{Dia}}$ and $Peak_{ch_{Si}}$ represent the peak channels of the diamond and silicon detectors, respectively; $C_{Dia}(C_{Si})$ and $m_{Dia}(m_{Si})$ represent the y-intercept value and gradient for the diamond (silicon) detector, respectively; ϵ_{Dia} and ϵ_{Si} represent the generation energy of electron-hole pairs for the diamond (13.1 eV) and silicon (3.62 eV) detectors, respectively; and $\epsilon_{loss_{Dia}}(\epsilon_{loss_{Si}})$ represents the energy loss of alpha-particles for the diamond (silicon) detector.

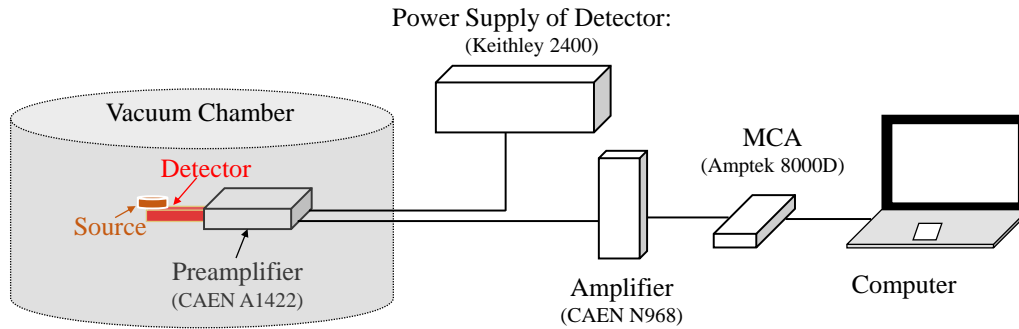


Figure 3.3: Measurement system for CCE.

Figure 3.4 shows the CCE as a function of the electric-field strength. With an increase in the electric-field strength, the CCE initially increased and then became saturated. For both detector thicknesses, saturation was observed above 6 kV/cm for particles with an energy of 3.183 MeV and above 2 kV/cm for the other energies. The 140- μm -thick detector exhibited slower saturation but a slightly higher CCE than the 25- μm -thick detector for all the alpha-particle energies. The saturation values of the 140- μm -thick detector for alpha-particles of 3.183, 5.486, and 5.805 MeV were measured as 91.4%, 96.6%, and 96.9%, respectively, and those of the 25- μm -thick detector were 91.0%, 95.6%, and 95.9%, respectively. The value for 3.183 MeV was approximately 5% lower than those for 5.486 and 5.805 MeV. The amounts of missing charges corresponded to 0.27, 0.19, 0.18 MeV for alpha-particles of 3.183, 5.486, and 5.805 MeV, respectively. This indicates that the CCEs of both the detectors depend on the energy of the alpha-particles.

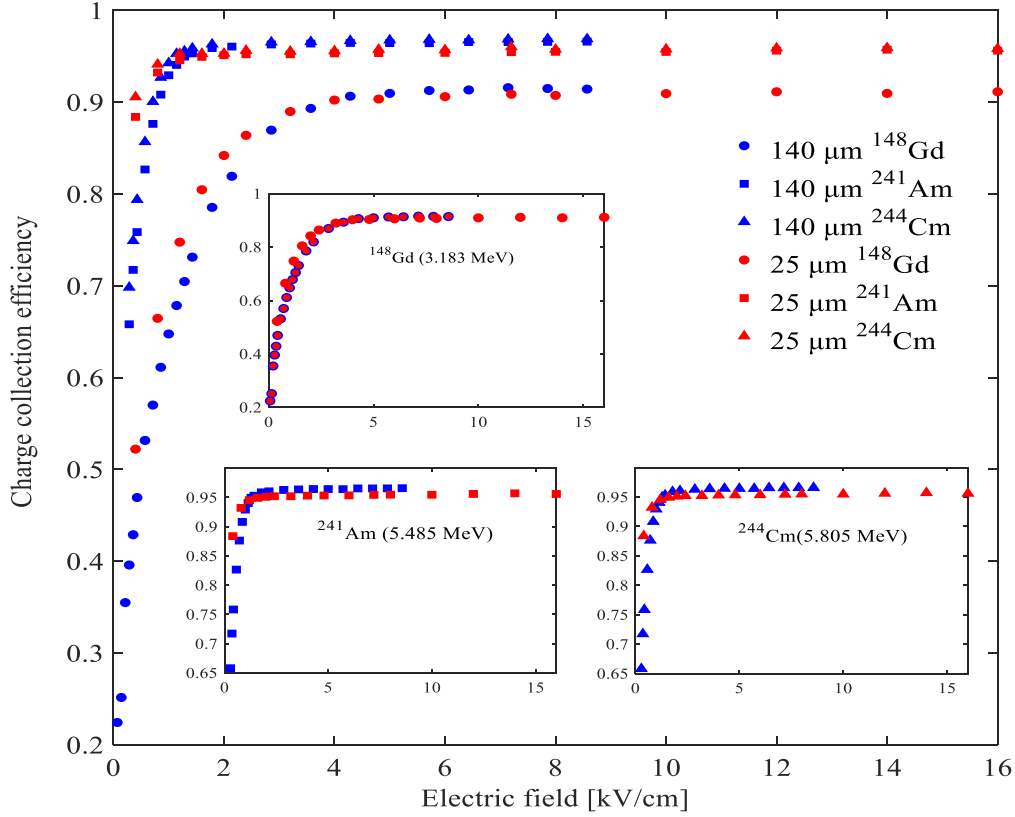


Figure 3.4: CCEs of the 25- and 140- μm -thick diamond detectors with respect to the electric- field strength.

The ranges of the alpha-particles with energies of 3.183, 5.486, and 5.805 MeV were 6.27, 13.63, and 14.85 μm , respectively. The ranges were all shorter than the distance between the electrodes for the 25- and 140- μm -thick detectors. Thus, the alpha-particles deposited all their energy in the detectors.

The hole drift distance was approximately 10 times longer than the electron drift distance for the 140- μm -thick detector because the alpha-particles were injected into the detector from the anode side and the range of the alpha-particles was approximately 1/10 of the total thickness. In contrast, the electron and hole drift distances were comparable for the 25- μm -thick detector. This difference did not result in a significant difference in the CCE values, implying that there was no significant charge loss due to the long hole drift distance. Because of the layout of the converter, charged particles from the converter were injected into the opposite side of the detector, implying

that the electron drift was dominant for the 140- μm -thick detector.

The possible reasons for the charge loss are as follows: (i) electron–hole recombination around the Bragg peak where high-density plasma existed and (ii) a dead layer on the surface of the diamond detector. The effects of (i) were mitigated for relatively light particles, such as tritons from the ${}^6\text{Li}(n, \alpha){}^3\text{H}$ reaction, and the effects of (ii) were estimated via energy-loss calculations. These calculations indicated an insensitive diamond layer with a thickness of 0.7 μm (0.9 μm Ti equivalent). This thickness exceeded the Ti thickness specified by the manufacturer (0.1 μm). It led to approximately 0.06-MeV energy loss for 2.73-MeV tritons from the ${}^6\text{Li}(n, \alpha){}^3\text{H}$ reaction.

According to the CCE measurements, the 25- and 140- μm -thick detectors were operated under bias voltages of 20 and 80 V, respectively, for further data collection. Because of the alpha-particle energy dependence, a low CCE value was expected for alpha-particles from the ${}^6\text{Li}(n, \alpha){}^3\text{H}$ reaction, which had an energy of <2.05 MeV.

Chapter 4

The response of diamond detector with traditional analog system

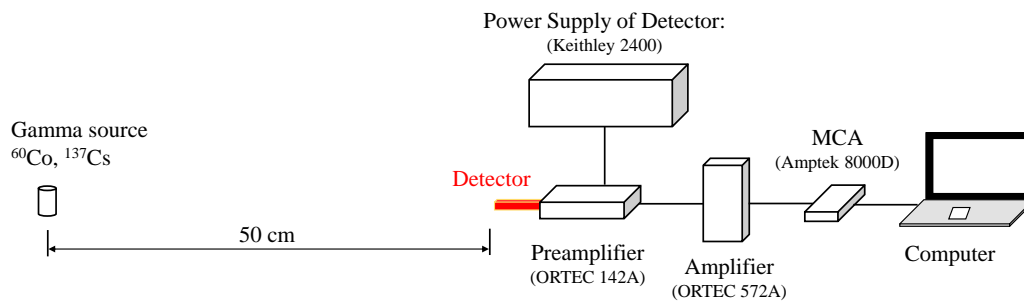
4.1 Experiment

4.1.1 Energy resolution

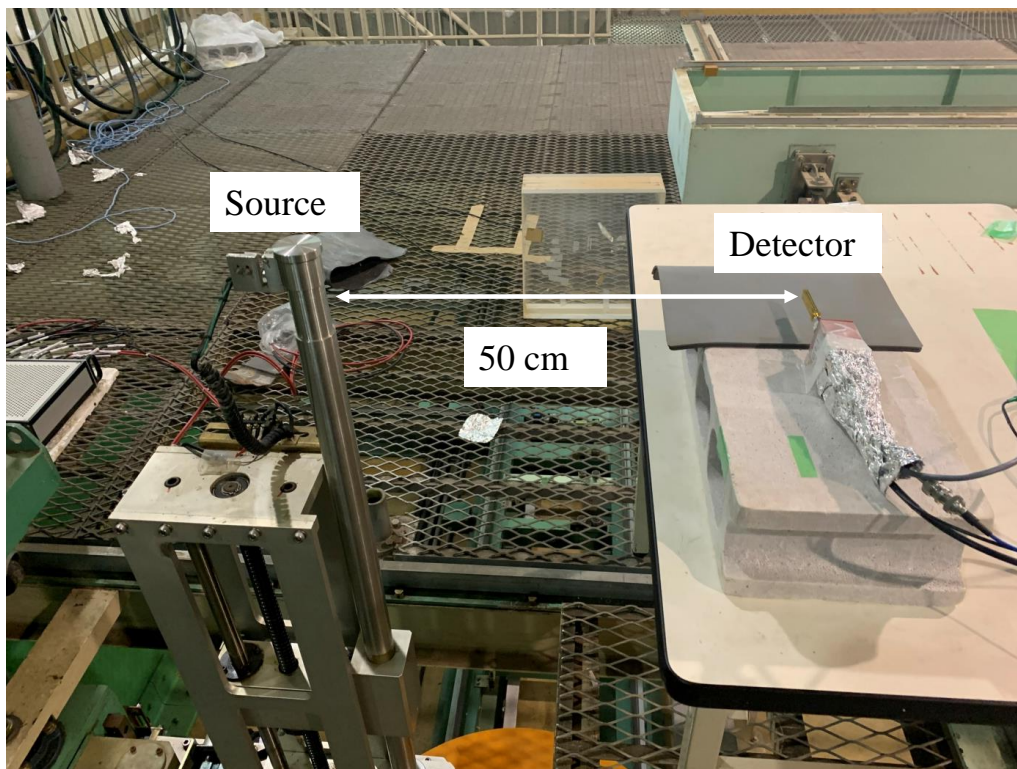
A high energy resolution is important for precise measurement of the neutron-induced reaction products (alpha-particles and tritons), which are discriminated from the interfering background γ -rays. The energy resolution was determined from the peak width of the alpha-particle spectrum obtained using this setup. The widths of the peaks were obtained as percentages of the full width at half maximum (FWHM) to the peak energy.

4.1.2 Response for Moderate activity γ -ray

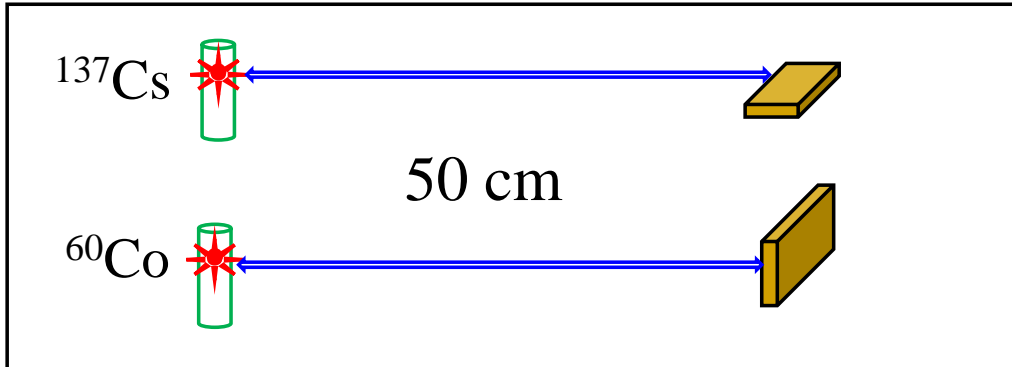
To obtain γ -ray responses for the detectors with their housings, ^{137}Cs (662 keV) and ^{60}Co (1173 and 1332 keV) γ -ray sources were used at the radiation calibration facility of KEK, Japan [54]. Figure 4.1 shows schematics and a photograph of the experimental setup. The source was 50 cm from the detector surface and was inside a vertical stainless-steel tube. The detector was placed on a polystyrene block, which was kept on a wooden table. In the experiment with the ^{60}Co source, the diamond detectors were set as shown in Fig. 4.1 (b), but for the ^{137}Cs source, the diamond detectors were rotated by 90° , so that the anode side faced the ground. Details regarding the gamma-source are presented in Table 4.1. The radioactivity values in Table 4.1 were measured on the day of the experiment.



(a) Measurement system.



(b) Photograph of experimental setup.



(c) Installed direction of detector.

Figure 4.1: Layout for the moderate-activity γ -ray response experiment.

Table 4.1: Details regarding the gamma source used in the experiment.

Source	Energy of the γ -rays [MeV]	Radioactivity [GBq]
^{60}Co	1.173, 1.332	14.2 ± 2.8
^{137}Cs	0.662	16.8 ± 3.4

The 25- and 140- μm -thick detectors were biased at 20 and 80 V, respectively, using the SMU. These bias voltages were based on the CCE results obtained prior to this experiment. A charge-sensitive preamplifier (ORTEC 142 A) connected to a shaping amplifier (ORTEC 572 A, shaping time of 0.5 μs) was used for signal readout. The pulse-height output of the amplifier was analyzed using a multichannel analyzer (MCA: Amptek 8000D). The mixed alpha-source was used for energy calibration. The threshold level of the MCA was set as 0.05 MeV. The irradiation time of each source for the 25- and 140- μm -thick detectors was 10 min for obtaining a total of 38400 and 221400 counts, respectively, to confirm the channel with the maximum pulse height.

4.1.3 High dose rate γ -ray responses experiment

To investigate the responses of the diamond detectors in the presence of a strong background of γ -rays, an intense ^{60}Co gamma-source at the ^{60}Co γ -ray irradiation facility of the Institute for Integrated Radiation and Nuclear Science, Kyoto University (KURNS) was used [55]. The source used for the high-dose rate γ -ray response experiment is shown in Fig. 4.2. The detectors were placed 30, 50, 70, 110, 170, 260, 350, and 500 cm from the center of the

^{60}Co source and exposed to intense γ -rays at dose rates ranging from 0.693 to 107 Gy/h. The 25- and 140- μm -thick detectors were biased at 20 and 80 V, respectively. In this experiment, a traditional analog detection system was used.

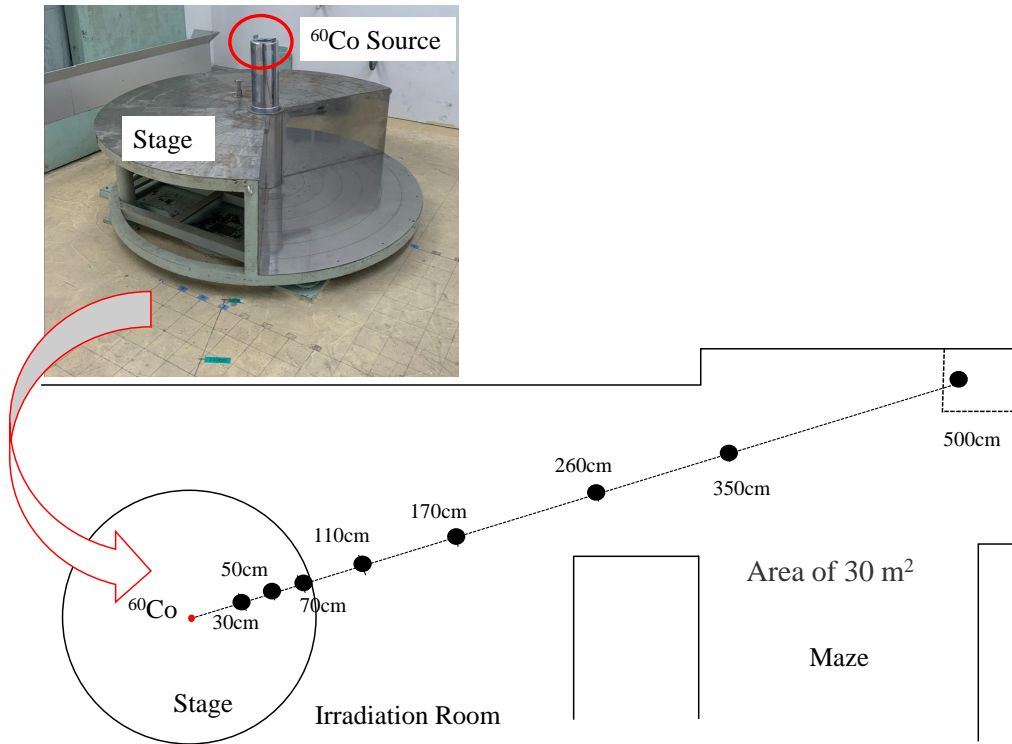


Figure 4.2: Photograph and plan view of the experimental setup for high-dose rate γ -ray response measurement.

4.1.4 Thermal-neutron response and detection efficiency measurement

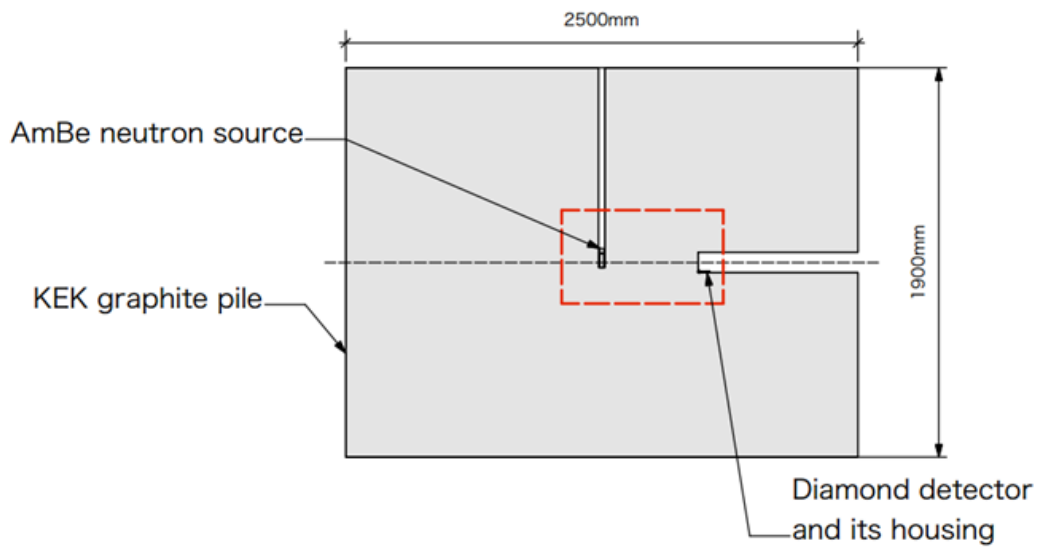
The response to thermal neutrons was obtained, i.e., the pulse-height spectrum and detection efficiency were measured, using the thermal-neutron field at KEK. The thermal-neutron field consisted of a ^{244}Am -Be neutron source with intensity of 37 GBq and a graphite pile [56]. Figure 4.3 shows a photograph and schematics of the experimental setup.

The neutron source was set at the center of the graphite pile, which consisted of high-purity reactor-grade graphite blocks. The dimensions of the graphite pile were $250 \times 190 \times 190 \text{ cm}^3$. One of the graphite blocks with

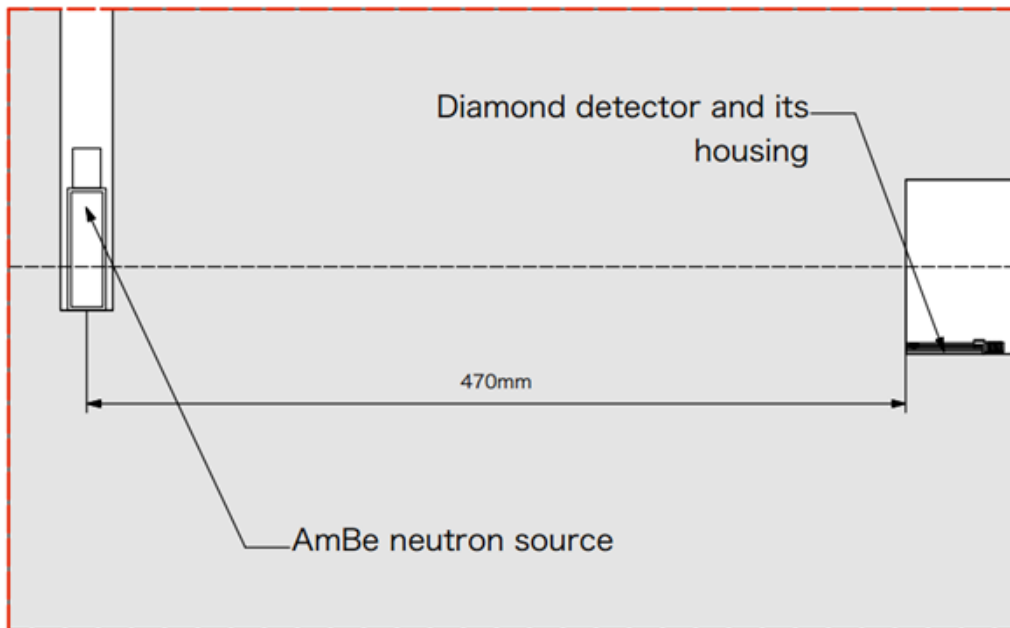
a size of $10 \times 10 \times 78 \text{ cm}^3$ at the center of the $190 \times 190 \text{ cm}^2$ surface was removed to insert the diamond detector into the pile. The distance from the center of the source to the center of the detector was 47 cm. At this point, the thermal-neutron flux was estimated to be $1171 \pm 8.46\% [\text{cm}^{-2}\text{s}^{-1}]$ through interpolation of previously reported values [56].



(a) Photograph of experiment setup.



(b) Vertical cross section of KEK graphite pile.



(c) Detail view of neutron source and detector.

Figure 4.3: Schematics and photograph of the experimental setup for thermal-neutron response measurement.

4.1.5 Fast neutron

The fast-neutron irradiation experiment was performed at the Facility of Radiation Standards (FRS) of the Japan Atomic Energy Agency (JAEA). The diamond detectors were irradiated with monochromatic energy neutrons. The irradiation conditions of the FRS neutron calibration field are presented in Table 4.2. A photograph of the irradiation system is shown in Fig. 4.4 [57]. The experimental layouts are presented in Fig. 4.5. The measurement circuit used is shown in Fig. 4.6.

Table 4.2: Irradiation conditions of the FRS neutron calibration field.

Energy [MeV]	Fluence [n/cm ²]	Geometry	Irradiation time [s]	Distance [cm]	Reaction
0.144	3.07×10^6 $\pm 1.1 \times 10^5$	Albedo	3640	130	p-Li
	3.38×10^6 $\pm 1.2 \times 10^5$	Sandwich	3761		
0.565	7.63×10^6 $\pm 2.1 \times 10^5$	Albedo	3629	130	p-Li
	7.11×10^6 $\pm 1.9 \times 10^5$	Sandwich	3619		
1.2	1.89×10^6 $\pm 7 \times 10^4$	Albedo	6014	110	p-T
	1.42×10^6 $\pm 6 \times 10^4$	Sandwich	4225		
5	9.47×10^6 $\pm 3.5 \times 10^5$	Albedo	4444	131	d-D
	7.58×10^6 $\pm 2.8 \times 10^5$	Sandwich	3616		
14.8	7.05×10^6 $\pm 4.3 \times 10^5$	Albedo	4594	110	d-T
	4.81×10^6 $\pm 2.2 \times 10^5$	Sandwich	3631		

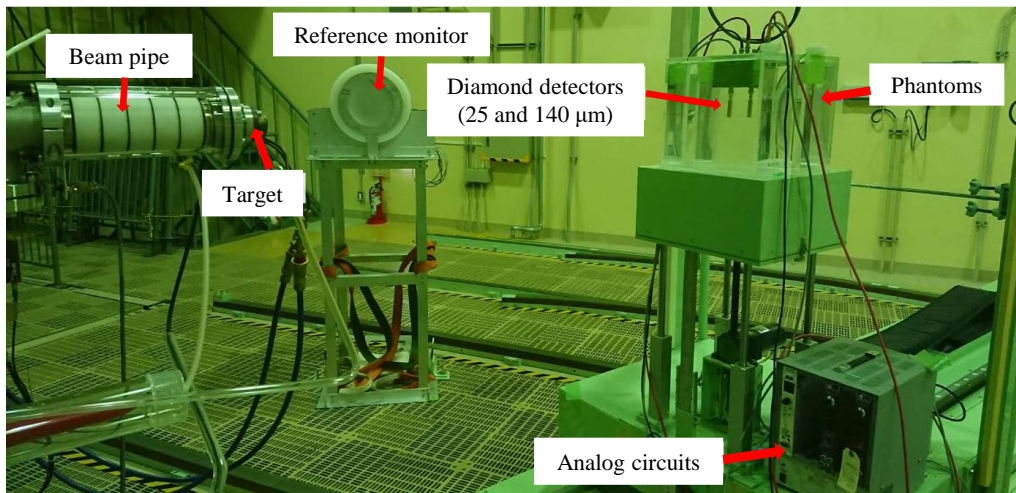


Figure 4.4: Monochromatic neutron irradiation system at FRS [57].

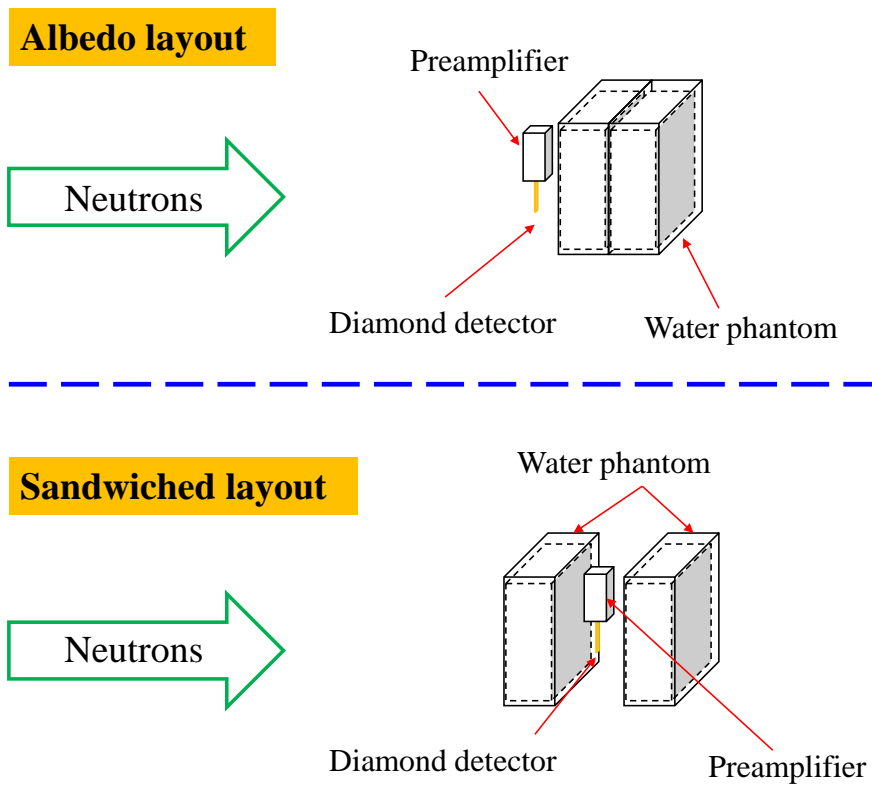


Figure 4.5: Moderator installation during neutron irradiation.

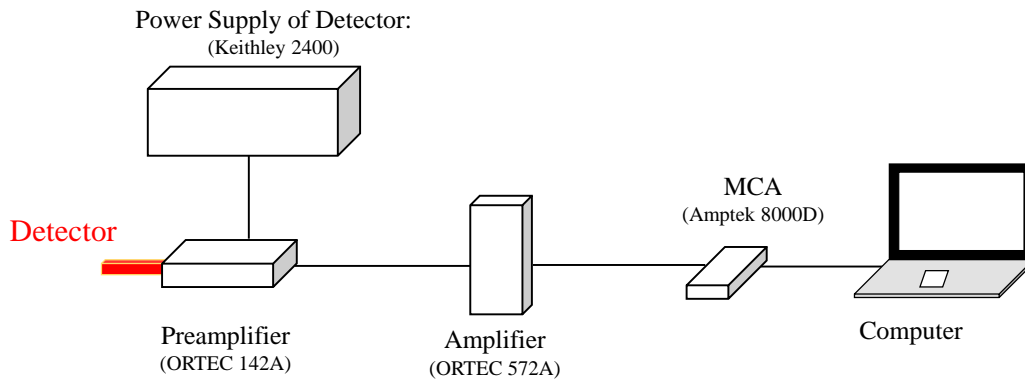


Figure 4.6: Measurement system for neutron irradiation.

In the neutron irradiation experiment, the fast neutrons were slowed by water in cuboid polymethyl methacrylate containers with sizes of $30 \times 30 \times 15 \text{ cm}^3$. Two experimental layouts were adopted to measure the fast-neutron responses of the diamond detectors with an ^6LiF converter in a light-water-moderated system. In the first layout (albedo), the 25- and 140- μm -thick diamond detectors were placed on the surface of the two-stacked light-water moderator. In the second layout (sandwiched), the two diamond detectors were placed between the two moderators. The size of the irradiation room was 16.5 m (width) \times 11.5 m (depth) \times 12.3 m (height). The centers of the detectors and the neutron source were set at the beamline height of 120 cm on the grating hatch, which was 5 cm thick, made of aluminum, and set at a height of 200 cm from the floor. The distances between the neutron target and the detectors were 115 and 130 cm in the first and second layouts, respectively.

4.2 Simulation

The PHITS code (version 3.11) was used to simulate the responses of the diamond detectors to γ -rays. Photons, electrons, and positrons were transported using the EGS5 algorithm. A cutoff energy of 10^{-4} eV was used for the transport of neutrons, but a cutoff energy of 1 keV was used for photons, electrons, and other ions. The t-deposit tally for the cell of the diamond crystal was used for calculating the spectrum of the energy deposition due to γ -rays.

As the thicknesses of the diamond crystals had uncertainty, four additional thicknesses (20, 30, 135, and 145 μm) were simulated, representing uncertainties of 5 μm for the thicknesses of 25 and 140 μm . The ^{60}Co and ^{137}Cs gamma-sources were set at a distance of 50 cm from the diamond detectors in the simulation. The cables and other equipment were ignored in the simulation. The covers of the sources, supporting structure, and room wall and floor were ignored. The mother volume of the simulation was filled with air, similar to the experiment.

A point 4π isotropic ^{241}Am -Be neutron source was placed at the center of the graphite pile. The neutron energy spectrum was obtained from ISO8529. The γ -ray emissions from the source were ignored for both 4.4 MeV and 60 keV. The library of the thermal scattering law, i.e., $S(\alpha, \beta)$, for graphite at room temperature (296 K) was used. The $S(\alpha, \beta)$ material card is an important card that considers the effects of the chemical bonds and crystal structure on neutron transport in the thermal energy region.

The dimensions of the graphite pile in the simulation were identical to those of the real graphite pile: $250 \times 190 \times 190 \text{ cm}^3$. Additionally, a graphite block with a size of $10 \times 10 \times 78 \text{ cm}^3$ at the center of the $190 \times 190 \text{ cm}^2$ surface was removed. The detector with its housing was placed in the hole, 47 cm from the source. Below the graphite pile was a concrete base, which contained 15 concrete blocks with sizes of $20 \times 20 \times 20 \text{ cm}^3$. The concrete base was covered with stainless steel having a thickness of 2.5 cm. The floor (concrete with a thickness of 50 cm) and wall (insulated composite steel plate with a thickness of 1.5 cm) outside the graphite piles with a distance of 170 cm were set. The material compositions and densities used in the PHITS simulation are presented in Table 4.3.

Table 4.3: Material compositions and densities used in the PHITS simulation.

Material	Element	Density [g/cm ³]	Mass ratio
Carbon	C	1.75	1
	H		1.844
Concrete	O	2.2	0.517
	Na		0.00238
	Mg		0.0091
	Al		0.052
	Si		0.124
	Ca		0.0024
	Fe		0.0192
	C		0.105
	Cr		0.195
Stainless steel	Fe	7.8	0.705
	Ni		0.1

4.3 Result and discussion

4.3.1 Energy resolution

Figure 4.7 shows the energy spectra of the mixed alpha-source for the two diamond detectors with an analog system. The spectra exhibited three peaks with energies of 3.183, 5.486, and 5.805 MeV. The electronic noise was well below the energy level of ~ 0.04 MeV. The ranges of the alpha-particles were smaller than the thicknesses of the detectors, which ensured the full deposition energy in the detectors. The energy resolutions (defined as the ratio of the FWHM to the full energy peak) for the 25- μm -thick detector were measured to be 1.6%, 1.0%, and 1.1% for ^{148}Gd , ^{241}Am , and ^{244}Cm , respectively, and those for the 140- μm -thick detector were 1.7%, 1.0%, and 1.1%, respectively. The energy resolutions of both the detectors were comparable to the results in the literature for 5.48-MeV alpha-particles (1.0–3.0%) [26][52].

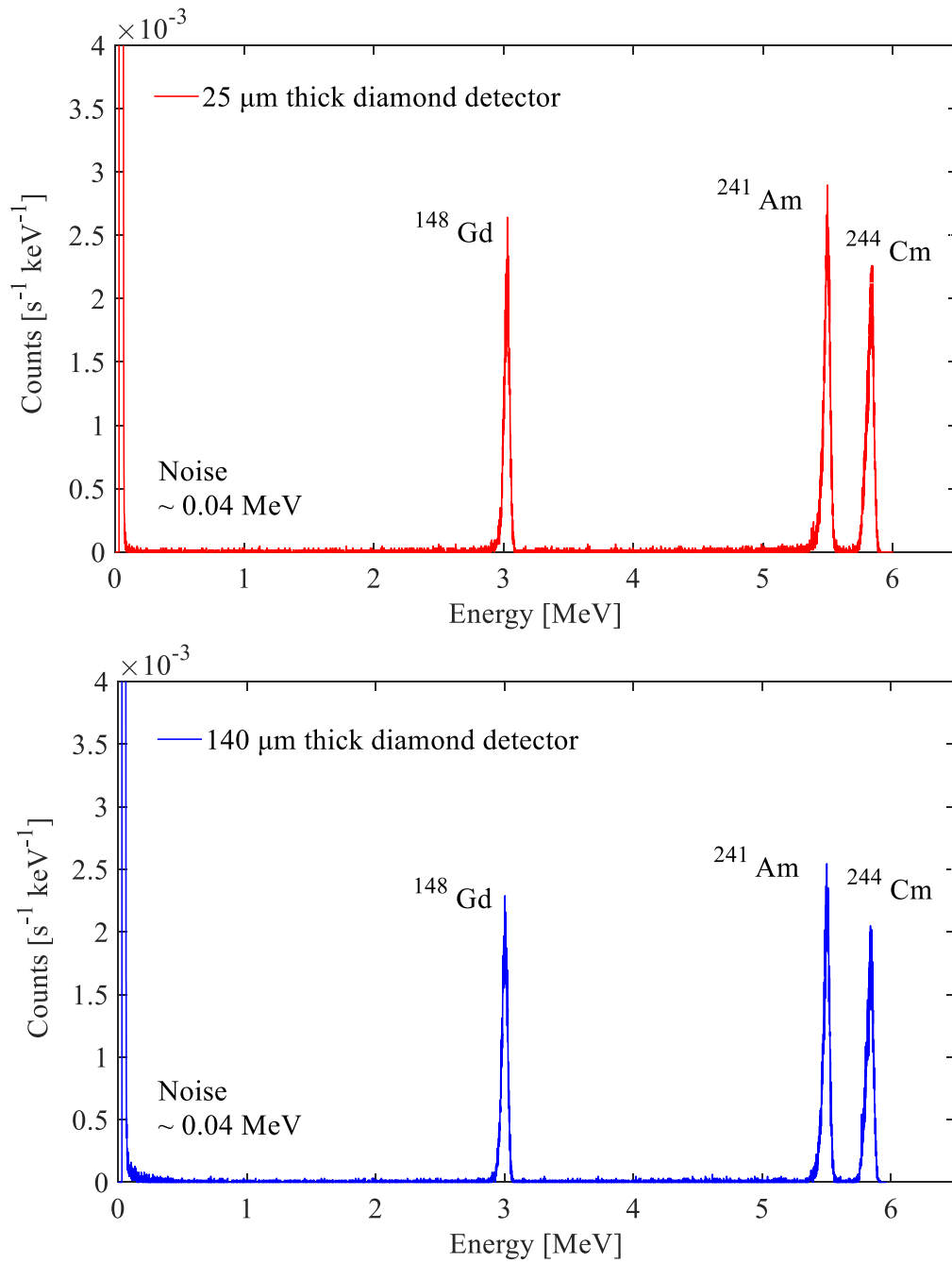


Figure 4.7: The energy spectra of the mixed alpha-source for the two diamond detectors with analog system. The bias voltages of the 25- and 140- μm -thick detectors were, respectively, 20 and 80 V.

4.3.2 Response to moderate-activity gamma-source

Figures 4.8 and 4.9 show the experimental energy spectra for the ^{137}Cs and ^{60}Co gamma sources together with the simulated results. The experimental and simulated results agreed well for both detectors with regard to the shape of the energy spectra and the maximum amount of energy deposition. The differences between the simulated and measured spectra were attributed to the uncertainties in the geometry and the material of the detector housing. The 25- and 140- μm -thick detectors exhibited differences in the shape of the energy spectra and the maximum amount of energy deposition. Owing to the small size of the detectors relative to the detector housing, the energy deposition in the detector mainly resulted from the interactions of the scattered γ -rays from the detector housing. The dominant interaction of γ -rays with the detectors in this energy range was the Compton scattering. The maximum energies of the Compton electrons were 477 keV for ^{137}Cs , 1118 keV, and 963 keV for ^{60}Co . A clear Compton edge of the ^{137}Cs source was observed with the 140- μm -thick detector, because the side of the detector faced the source. The 25- μm -thick detector exhibited a completely different spectrum for the ^{137}Cs source, indicating that most of the electrons escaped from the diamond and only partially deposited their energy. This phenomenon significantly reduced the γ -ray sensitivity, according to a pulse-height analysis. For the ^{60}Co source, the 25- and 140- μm -thick detectors exhibited similar behavior owing to the higher energy of the Compton electrons.

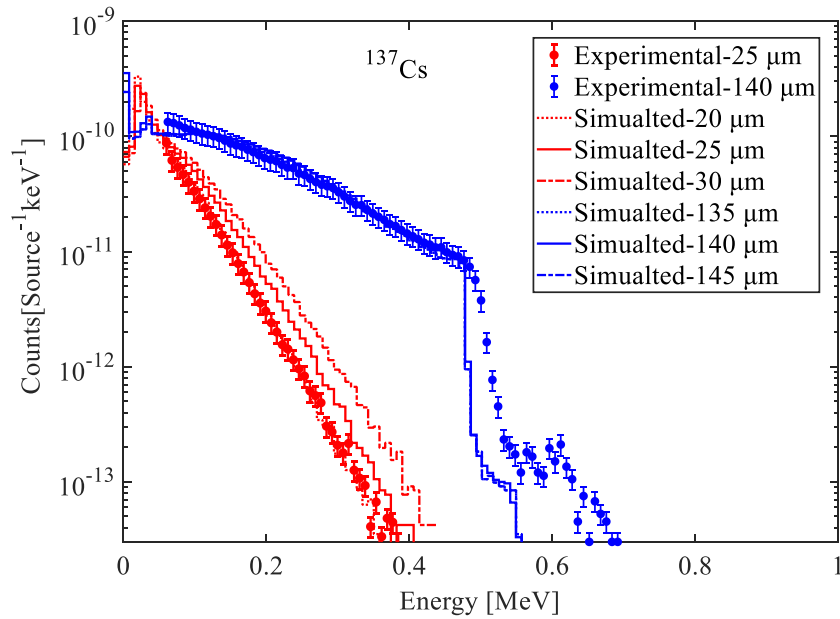


Figure 4.8: Measured and simulated responses of the 25- and 140- μm thick diamond detectors to ^{137}Cs γ -rays

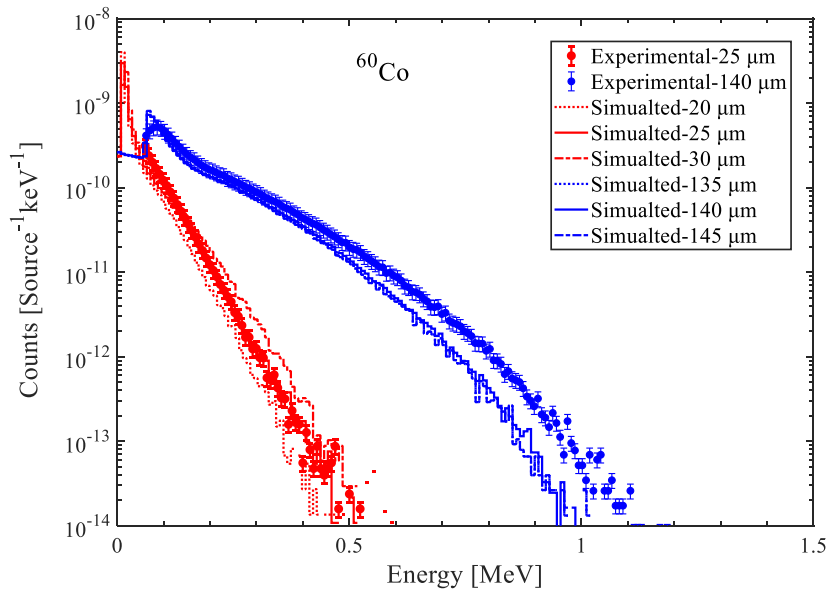


Figure 4.9: Measured and simulated responses of the 25- and 140- μm -thick diamond detectors to ^{60}Co γ -rays.

The simulated and experimental results for the count rate, maximum deposition energy, and response are presented in Tables 4.4 and 4.5. The response and count rate were calculated by setting a threshold of >0.056 MeV. The count rate and response varied with respect to the thickness and energy. The 140- μm -thick detector was significantly higher than the 25- μm -thick detector, even up to several times, indicating that the 25- μm -thick detector was up to 5 times less sensitive to γ -rays. The simulated and experimental maximum deposition energies for the two detectors were almost identical, considering the error range. As expected, the maximum deposition energy also varied with respect to the thickness and energy. The maximum deposition energies of the 25- μm -thick detector were significantly lower than those of the 140- μm -thick detector and significantly lower than the expected deposition energies for the neutron-induced ${}^6\text{Li}(n, \alpha){}^3\text{H}$ reaction: $E_t = 2.73$ MeV, $E_\alpha = 2.05$ MeV. Comparing the results for the count rate, maximum deposition energy, and response revealed that the γ -ray energy had a less significant effect on the response for the 25- μm -thick detector than for the 140- μm -thick detector.

Table 4.4: Experimental results of count rate, maximum deposition energy, response.

Source	Detector	Count rate [s^{-1}] (>0.056 MeV)	Response [cm^2] (>0.056 MeV)	Maximum deposition energy [MeV] ($E_{99.99}$)
${}^{137}\text{Cs}$	25 μm	6.4×10^1 ± 1.2	8.3×10^{-5} $\pm 1.9 \times 10^{-5}$	4.2×10^{-1} $\pm 1.0 \times 10^{-1}$
	140 μm	3.7×10^2 ± 7.3	4.8×10^{-4} $\pm 1.1 \times 10^{-4}$	6.4×10^{-1} $\pm 2.2 \times 10^{-1}$
${}^{60}\text{Co}$	25 μm	2.0×10^2 ± 8.7	3.8×10^{-4} $\pm 7.8 \times 10^{-5}$	4.6×10^{-1} $\pm 9.2 \times 10^{-2}$
	140 μm	1.0×10^3 ± 37.8	1.9×10^{-3} $\pm 3.9 \times 10^{-4}$	9.7×10^{-1} $\pm 2.2 \times 10^{-1}$

Table 4.5: Simulated results of count rate, maximum deposition energy, response.

Source	Detector	Count rate [s^{-1}] (>0.056 MeV)	Response [cm^2] (>0.056 MeV)	Maximum deposition energy [MeV] ($E_{99.99}$)
^{137}Cs	25 μm	8.7×10^1 $\pm 2.3 \times 10^{-1}$	9.6×10^{-5} $\pm 1.9 \times 10^{-5}$	4.1×10^{-1} $\pm 8.0 \times 10^{-2}$
	140 μm	4.1×10^2 $\pm 4.9 \times 10^{-2}$	4.6×10^{-4} $\pm 9.0 \times 10^{-5}$	5.3×10^{-1} $\pm 1.6 \times 10^{-2}$
^{60}Co	25 μm	1.6×10^2 $\pm 9.0 \times 10^{-2}$	3.1×10^{-4} $\pm 6.4 \times 10^{-5}$	4.9×10^{-1} $\pm 8.0 \times 10^{-2}$
	140 μm	1.1×10^3 $\pm 1.2 \times 10^{-2}$	2.1×10^{-3} $\pm 4.3 \times 10^{-4}$	8.9×10^{-1} $\pm 1.6 \times 10^{-2}$

4.3.3 Response to high dose rate γ -ray

The results of the intense γ -ray irradiation experiments at KURNS are shown in Fig. 4.10. The dose rates and count rates of the detectors are presented in Table 4.6. As shown, the maximum values in the pulse-height distributions increased with the dose rate—particularly for the 140- μm -thick detector. This effect resulted from the pile-up of output pulses, which increased the amplitude of the registered event. Figure 4.10 shows the maximum values of the pulse-height distributions at count rates above 0.1 $keV^{-1}s^{-1}$. The amplitudes of the pulses from the 140- μm -thick detector exceeded the energy of the peak corresponding to the tritons (2.73 MeV) produced in the $^6Li(n, \alpha)^3H$ reaction at dose rates above 6.36 Gy/h, whereas for the 25- μm -thick detector, the maximum pulse amplitude remained below the energy of the peak corresponding to the tritons even at a high dose rate of 107 Gy/h.

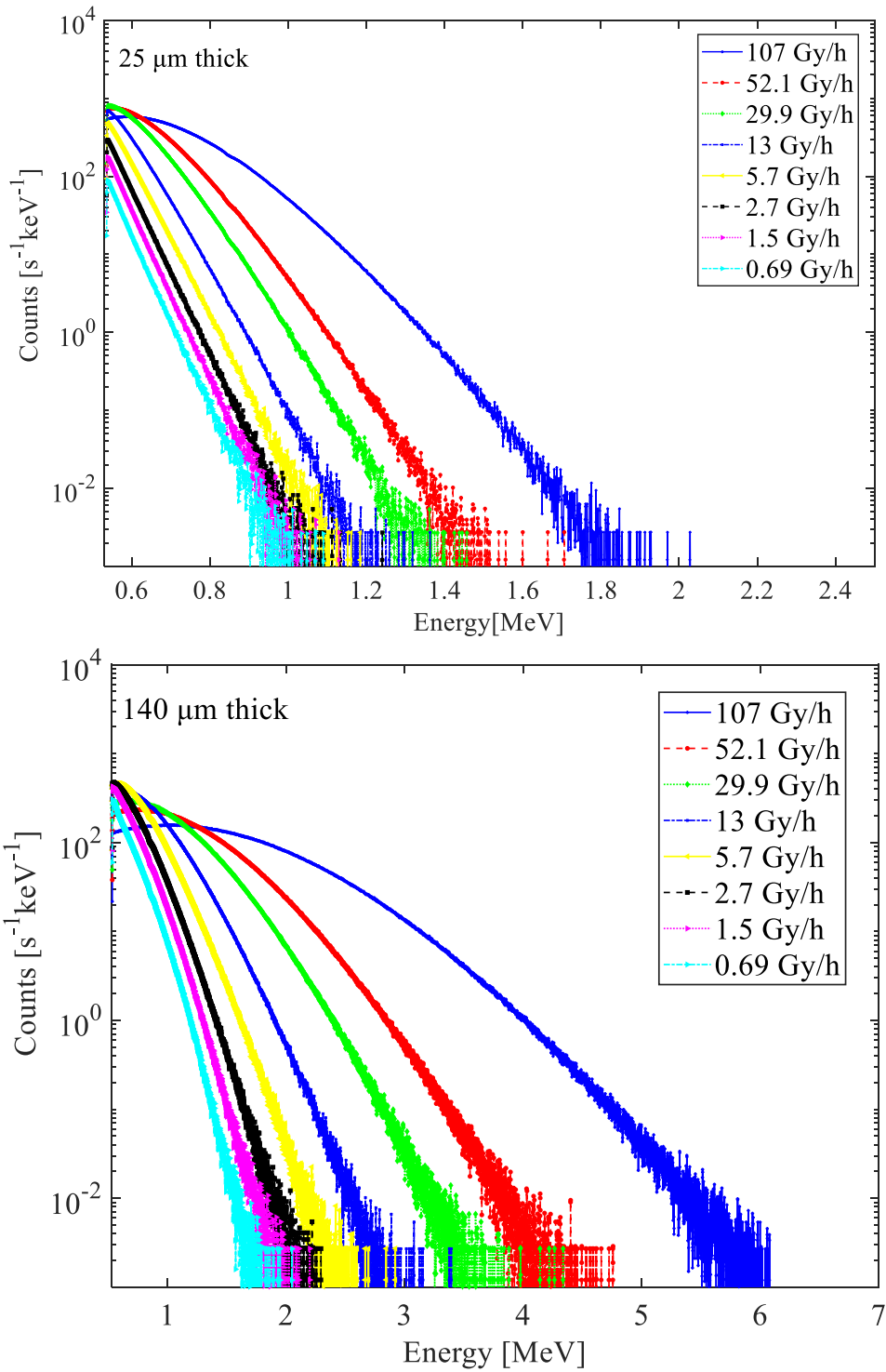


Figure 4.10: Measured spectra for the 25- and 140- μm -thick detectors exposed to ^{60}Co γ -rays with respect to the air absorbed dose rate.

Table 4.6: Measured gamma-source dose rate and count rate.

Distance from the ^{60}Co source [cm]	Air absorbed dose rate [Gy/h]	Count rate of the 25 μm thick detector [s^{-1}]	Count rate of the 140 μm thick detector [s^{-1}]
30	107	2.13×10^5	4.30×10^5
50	52.1	1.39×10^5	3.42×10^5
70	29.9	1.01×10^5	3.07×10^5
110	13.0	5.16×10^4	2.52×10^5
170	5.73	2.63×10^4	1.93×10^5
260	2.72	1.31×10^4	1.23×10^5
350	1.51	7.42×10^3	8.07×10^4
500	0.69	3.58×10^3	4.28×10^4

4.3.4 Thermal-neutron response and detection efficiency

Figure 4.11 shows the experimental and simulated results for the pulse-height distributions of the 25- and 140- μm -thick detectors with their housings in a thermal-neutron field. The experimental spectrum exhibited one prominent triton peak at 2.7 MeV, along with a continuous component attributed to energy deposition by alpha-particles and electrons below 2 MeV. The tritons and alpha-particles came from the $^6\text{Li}(n, \alpha)^3\text{H}$ reaction at the converter, and the electrons came from γ -rays produced by the thermal-neutron capture reaction.

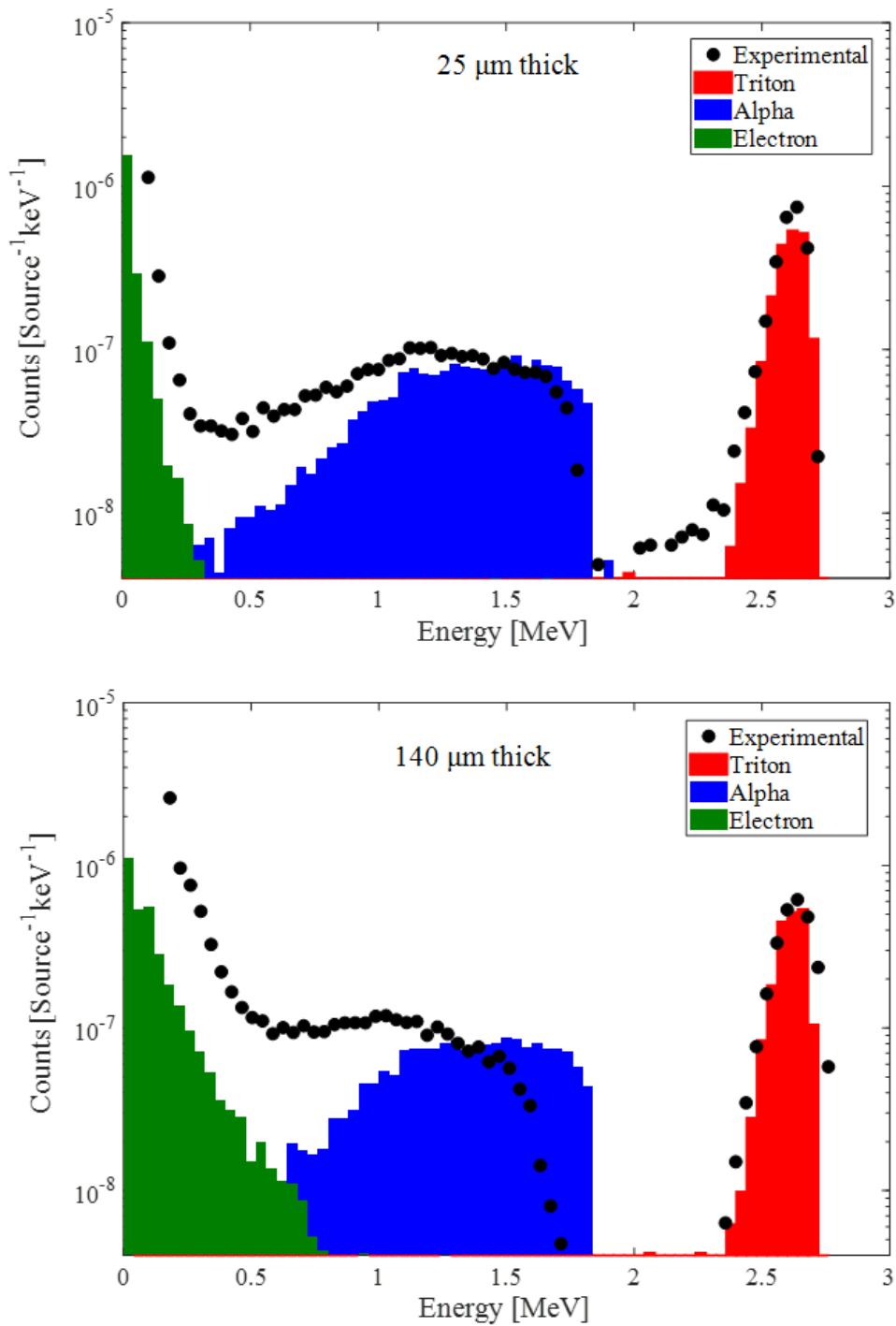


Figure 4.11: The simulated and experimental spectrum for thermal neutron detection in KEK graphite pile by the 25- and 140- μm -thick diamond detectors.

The triton peak, whose energy was 2.73 MeV, was clearly separated from the other components. For the 25- μm -thick detector, the FWHM and full width at tenth maximum (FWTM) of the peak were 120 and 280 keV, respectively. For the 140- μm -thick detector, the FWHM and FWTM of the peak were 140 and 340 keV, respectively. The widths were well reproduced by the PHITS simulation considering the ^6LiF converter thickness, the diameter of the through-hole, and the distance from the converter to the detector.

The experimental alpha component was shifted to a lower energy compared with the simulated spectrum—particularly for the 140- μm -thick detector. In contrast to the electron and alpha distributions, the experimental and simulated results agreed well for the triton region for both detectors. Thus, the triton peak can be used for thermal-neutron measurement by setting a threshold using the diamond detector.

Below 2 MeV, alpha-particles with an initial energy of 2.05 MeV were observed as a continuous energy component because of the relatively large energy loss in the converter and the air between the converter and the detector. On the high-energy side of the continuous component, the energy of alpha-particles in the experimental data is lower than that in the calculated one for a few hundreds of keV. This can be explained by the results of the CCE measurements where it was shown that a charge-loss of approximately 10% was observed for 2.05 MeV alpha-particles in the electric fields of 8 and 5.7 kV/cm for the 25- and 140- μm -thick detectors.

Below the continuous energy component of alpha-particles, another low-energy component mainly having energy of <0.4 MeV was observed. This component was ascribed to electrons, on the basis of the simulated results shown in Fig. 4.11. The electron distribution in the simulated spectrum was due to γ -rays from the thermal-neutron capture reaction. In comparison, in the experimental spectrum, the electron distribution was higher, because the simulation did not include the γ -rays from the ^{241}Am -Be source (60 keV and 4.4 MeV). The difference between the simulated and experimental spectra was larger for the 140- μm -thick detector than for the 25- μm -thick detector, which can be explained by the fact that diamond detectors with different thicknesses have different sensitivities to γ -rays.

Table 4.7 presents the measured count rate of triton peaks and efficiency. The neutron detection efficiency was calculated as follows:

$$\text{Efficiency} = \frac{N_{\text{detection}}}{N_{\text{total}}} = \frac{\text{Count rate}}{\text{Flux} \times \text{Area}} \quad (4.1)$$

The active area of diamond detector is 10 mm².

Table 4.7: Measured count rate and efficiency.

Diamond detector thickness	Thermal neutron flux [$\text{cm}^{-2}\text{s}^{-1}$]	Count rate [s^{-1}]	Efficiency
25 μm	$1171 \pm 8.5\%$	$0.12 \pm 1.00\%$	$1.04 \times 10^{-3} \pm 9 \times 10^{-5}$
140 μm	$1171 \pm 8.5\%$	$0.12 \pm 1.00\%$	$1.03 \times 10^{-3} \pm 9 \times 10^{-5}$

The uncertainty of the count rate of triton peaks was determined using statistics. The neutron emission rate ($2.1 \times 10^6 \pm 3\%$ n/s) was obtained from a reference [56]. The neutron emission rate of the source was previously determined using gold-foil activation detectors and the Cd difference method.

The thermal-neutron flux was determined at the detector position in the graphite pile. When the distance was set as 47 cm, the thermal-neutron detection efficiencies of the 25- and 140- μm -thick detectors were $1.04 \times 10^{-3} \pm 8.87 \times 10^{-5}$ and $1.03 \times 10^{-3} \pm 8.83 \times 10^{-5}$, respectively.

4.3.5 Response of the fast neutron with water phantoms

Fast neutrons can directly interact with diamond. Detection of fast neutrons is based on measurement of the charged particles generated via neutron-induced nuclear reactions on ^{12}C . The reaction channels of the $n + ^{\text{nat}}\text{C}$ reaction are presented in Table 1.3. The cross sections for different $n + ^{\text{nat}}\text{C}$ and $n + ^6\text{Li}$ reaction channels are shown in Figs. 4.12 and 4.13, respectively [58].

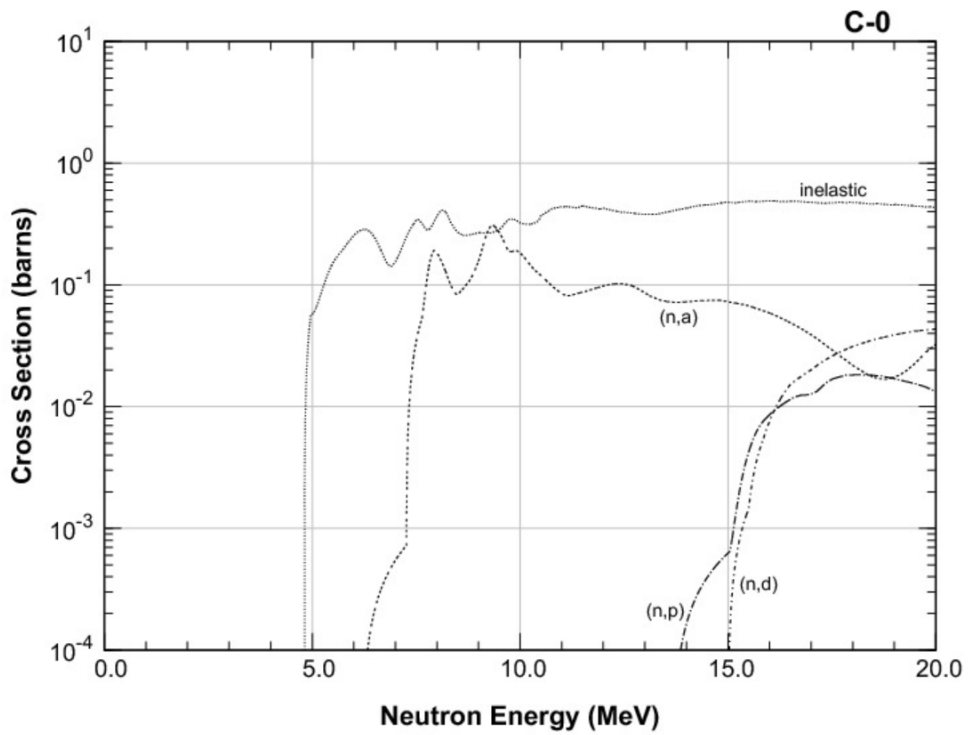
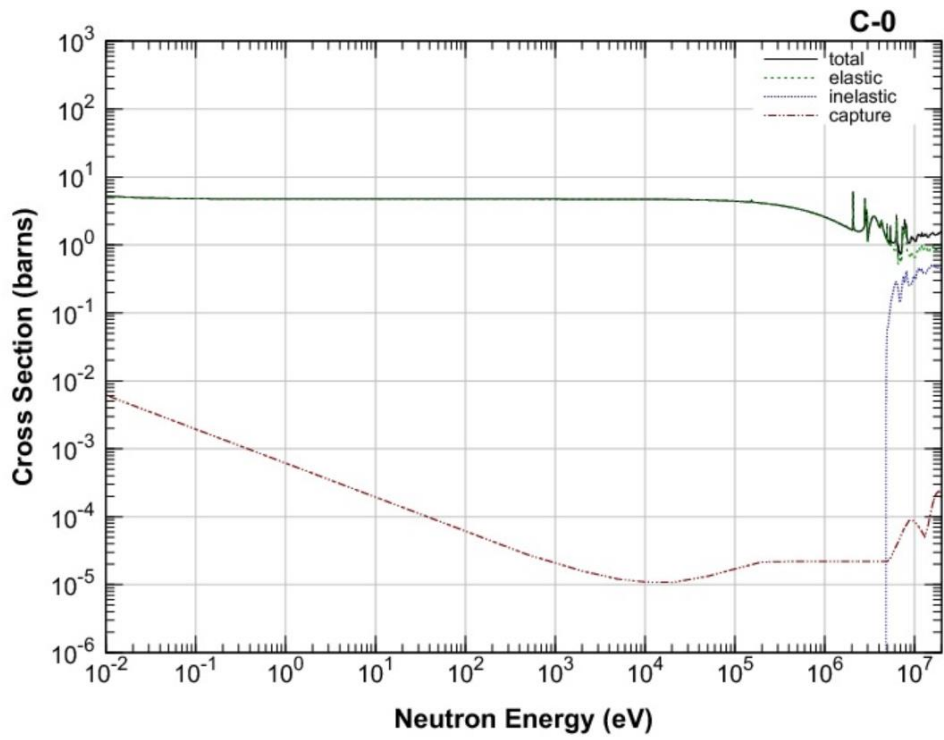


Figure 4.12: The cross-section for different $n + {}^{\text{nat}}\text{C}$ reaction channels [58].

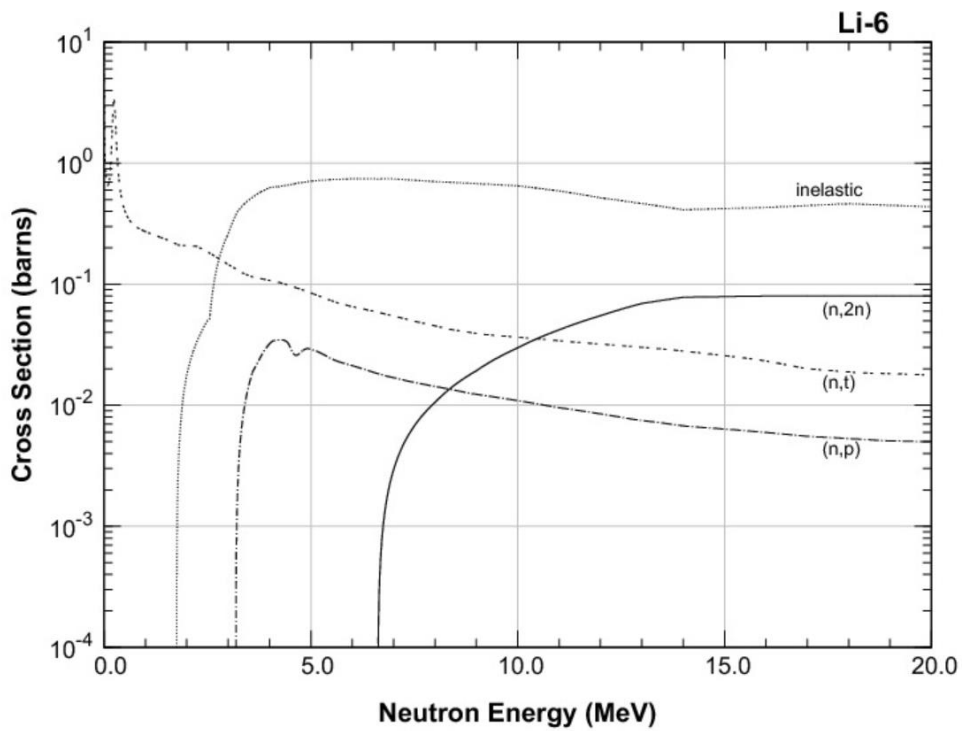
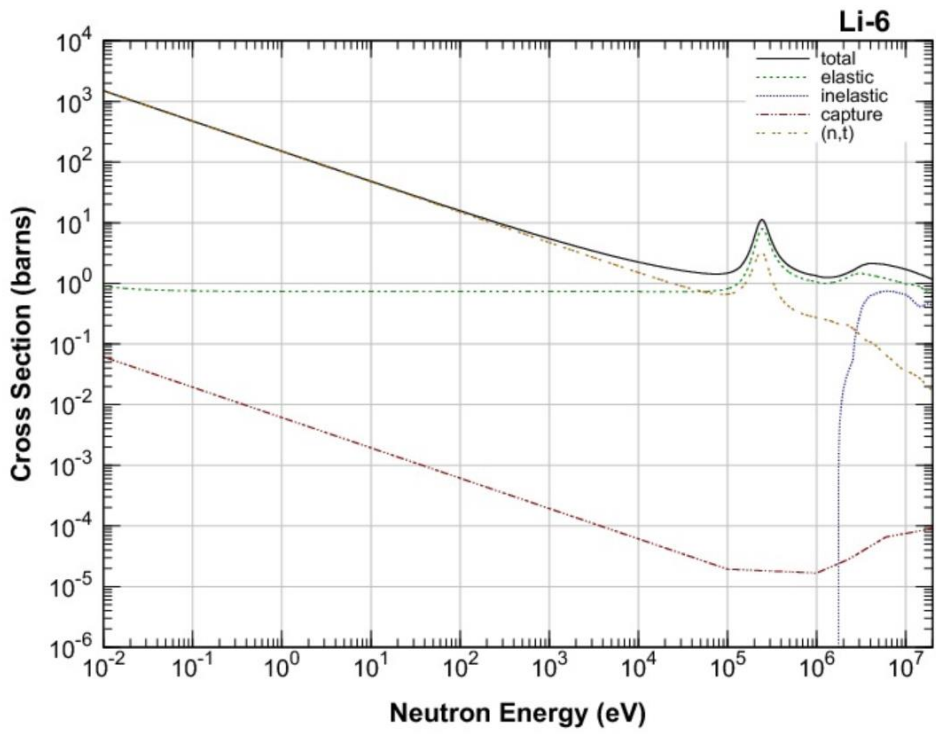


Figure 4.13: The cross-section for different $n + {}^6\text{Li}$ reaction channels [58].

Figures 4.14~4.18 show the experimental spectra measured using the 25- and 140- μm -thick diamond detectors for each energy and irradiation system.

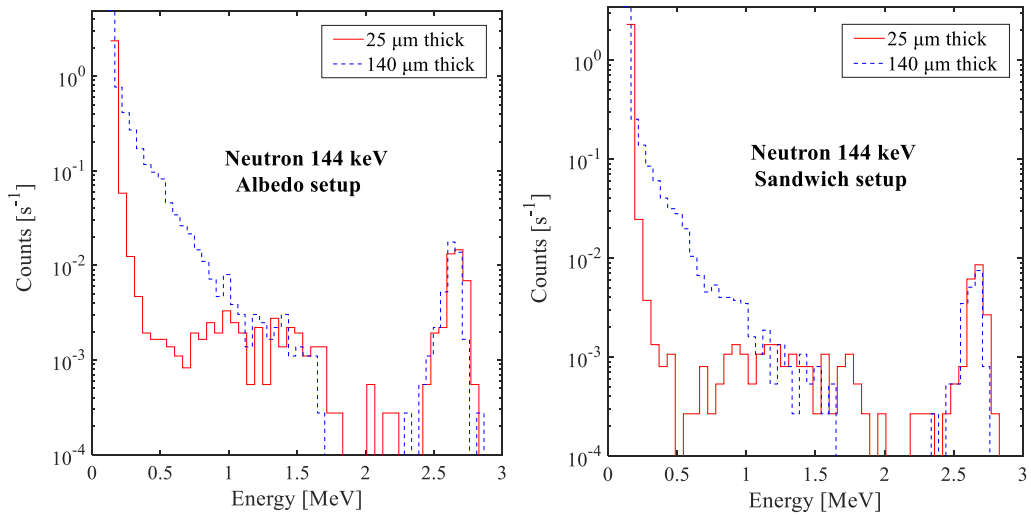


Figure 4.14: Experimental spectra for 144-keV neutron irradiation (left, albedo layout; right, sandwich layout).

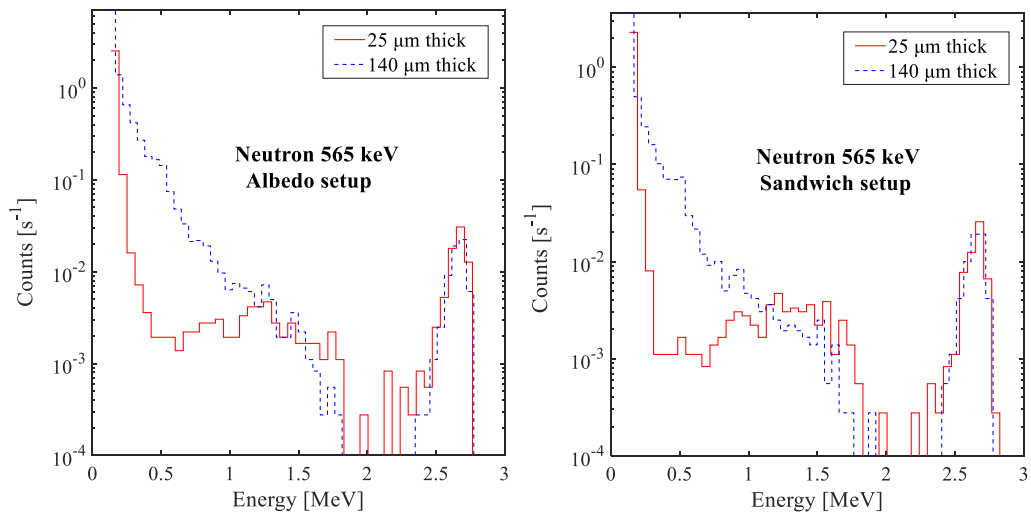


Figure 4.15: Experimental spectra for 565-keV neutron irradiation (left, albedo layout; right, sandwich layout).

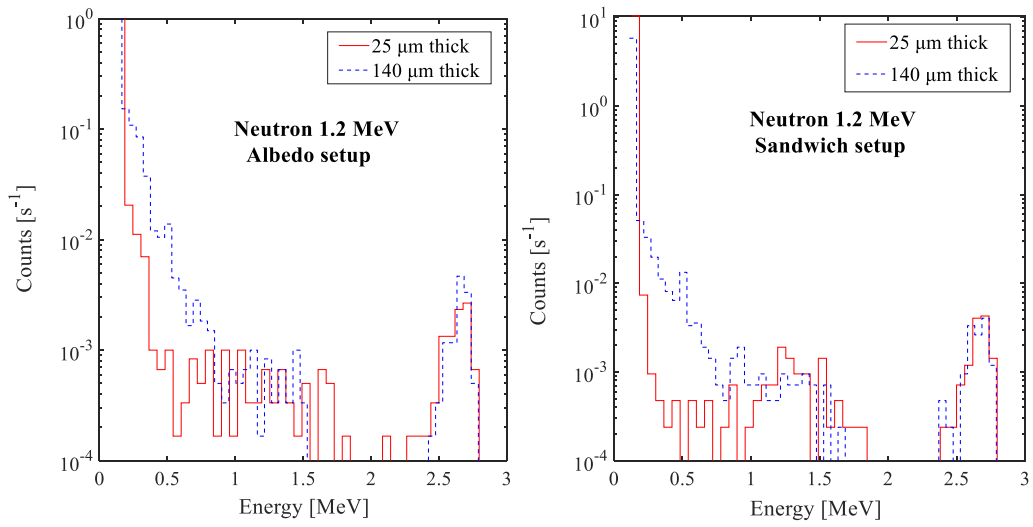


Figure 4.16: Experimental spectra for 1.2-MeV neutron irradiation (left, albedo layout; right, sandwich layout).

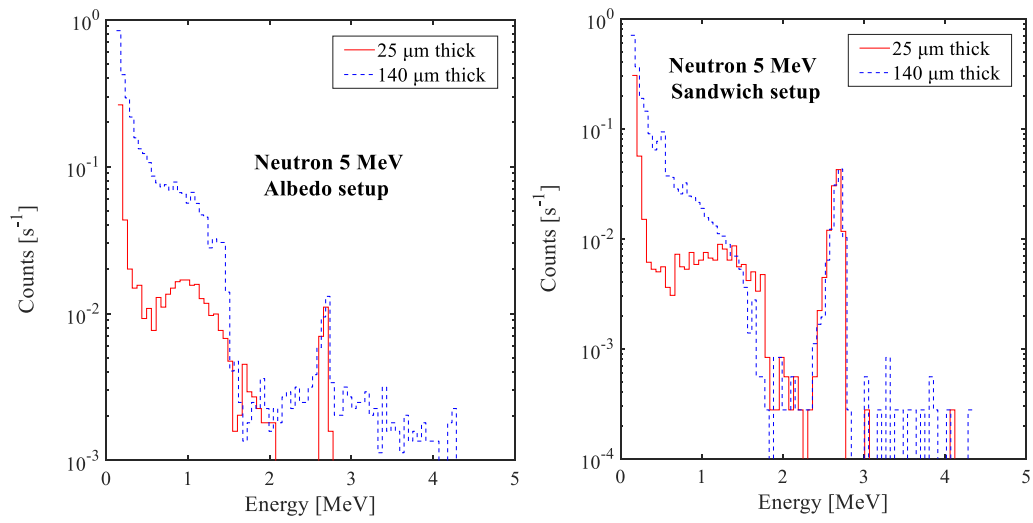


Figure 4.17: Experimental spectra for 5-MeV neutron irradiation (left, albedo layout; right, sandwich layout).

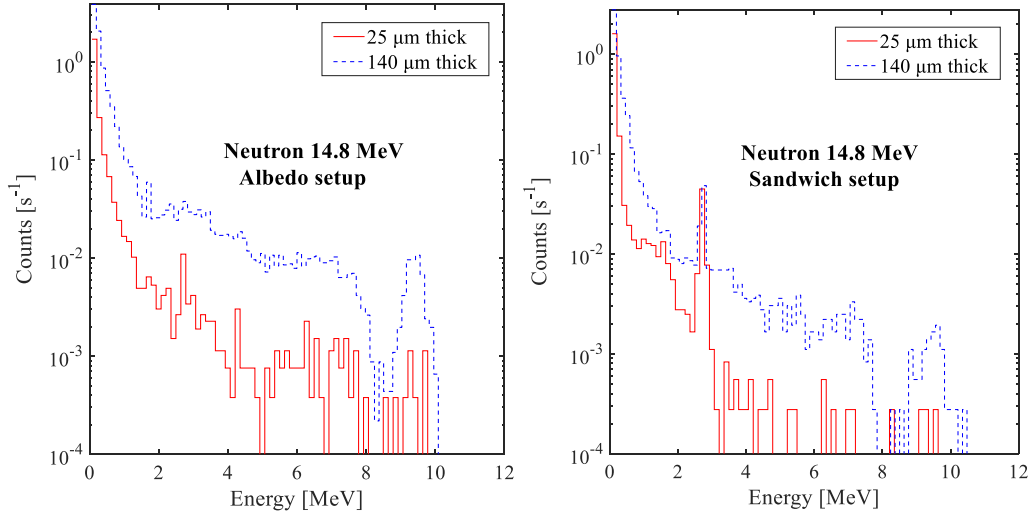


Figure 4.18: Experimental spectra for 14.8-MeV neutron irradiation (left, albedo layout; right, sandwich layout).

Figures 4.14~4.16 present the energy-deposition spectra for incident energies of <1.2 MeV. As shown, peaks corresponding to 2.73-MeV tritons from ${}^6\text{Li}(n, \alpha){}^3\text{H}$ were clearly observed. The energy spectrum was similar to that for thermal-neutron irradiation (Fig. 4.11). However, in the energy spectrum of the 140- μm -thick detector, the electronic distribution overlapped with the alpha part. This difference is attributed to the fact that the cross section of ${}^6\text{Li}(n, \alpha){}^3\text{H}$ decreased with an increase in the neutron energy.

However, from Fig. 4.17 (which shows the energy-deposition spectra for an incident energy of 5 MeV), the high-energy neutrons directly interacted with the diamond and underwent continuous energy deposition owing to the elastic scattering. Hence, the energy spectrum of the 5-MeV neutrons reflected not only the product of the ${}^6\text{Li}(n, \alpha){}^3\text{H}$ reaction but also those of the (n, p), (n, t), inelastic reaction involving ${}^6\text{LiF}$ and the inelastic reaction from diamond. The triton peak was clearly observed in the energy spectrum for the 25- μm -thick detector but not for the 140- μm -thick detector.

As shown in Fig. 4.18, at a neutron energy of 14.8 MeV, a peak of the ${}^{12}\text{C}(n, \alpha){}^9\text{Be}$ reaction (Q-value: -5.7 MeV) was observed near 9 MeV, in addition to the ${}^3\text{H}$ peak caused by thermal neutrons at 2.73 MeV. The component of the direct reaction between neutrons and carbon was prominent in the energy spectrum for the 140- μm -thick detector, but it was small for the 25- μm -thick detector. This indicates that the thickness of 25 μm is unsuitable for high-energy neutron detection.

The deposition energy of direct interaction was lower for the sandwich layout than for the albedo layout. This can be explained by the fact that the moderator played an important role in slowing the fast neutrons and thereby converting them into thermal neutrons.

Figure 4.19 shows the efficiency for the triton peak components measured by the 25- and 140- μm -thick diamond detectors for each irradiation system. In the albedo system, a higher neutron energy corresponded to a lower sensitivity of the diamond detector, but in the sandwich system, the sensitivity was highest near 5 MeV. This indicates that the 5-MeV neutrons were decelerated by the 15-cm-thick water phantom, which can be explained by the simulated results. The PHITS Monte Carlo simulation indicated that in the albedo system, the total neutron flux decreased from 90% to 20% with an increase in the energy from 144 keV to 14.8 MeV owing to the slowing effect of the 15-cm-thick water phantom. Additionally, 4%~19% of the neutrons were in the thermal-neutron range with the neutron energy ranging from 144 keV to 14.8 MeV. This indicates that the slowing effect for fast neutrons in the albedo system becomes weaker with an increase in the neutron energy. This can be explained by that a higher energy corresponds to a lower sensitivity of the diamond detector. For the sandwich system, the total neutron flux decreased with an increase in the incident energy in the range of ≤ 1.2 MeV and decreased from 18% to 6% as the incident energy increased from 5 to 14.8 MeV. Additionally, 33.3%~96.5% of the neutrons were in the thermal-neutron range with the neutron energy ranging from 144 keV to 14.8 MeV. This indicates that the slowing effect for fast neutrons was better for the sandwich system than for the albedo system, and the sandwich system exhibited the optimal performance at a neutron energy of 5 MeV.

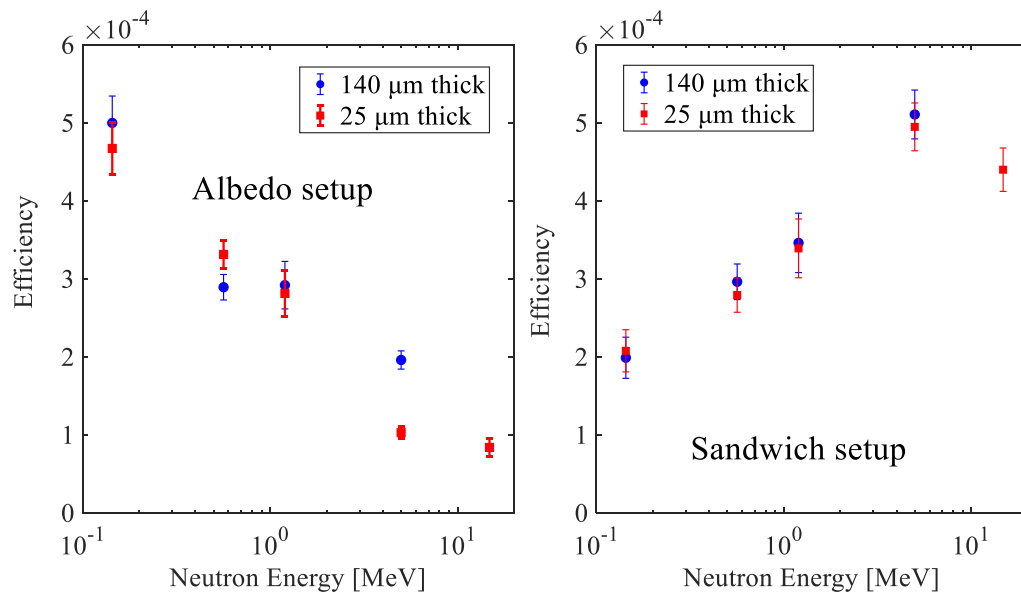


Figure 4.19: Fast-neutron detection efficiencies with different energies (left, albedo layout; right, sandwich layout).

Chapter 5

Response of diamond detector using TCT-Acqiris digital system

As discussed in previous chapters, the separation of γ -rays from neutrons can be performed via simple pulse-height analysis when there is no signal pile-up effect and the pulse height of the γ -rays is significantly smaller than that of the charged particles from the reaction.

As mentioned in Chapter 2, the pulse heights of γ -rays are determined by not only their energy but also the thickness of the diamond detector, because the thickness determines the maximum deposition energy of the electrons from the γ -rays. The separation of γ -rays from neutrons can be performed via simple pulse-height analysis because of the positive Q-value of the converter reaction. However, owing to signal pile-ups, the separation worsens when the pulse heights of the γ -rays are close to that of the charged particles from the reaction ${}^6\text{Li}(n, \alpha){}^3\text{H}$. Therefore, a fast current-sensitive preamplifier and a waveform digitizer were employed to avoid pulse pile-up events.

5.1 Pulse-height analysis processing

Figure 5.1 presents the typical signals of an ^{241}Am alpha source from TCT system with the 25- and 140- μm -thick CVD diamond detectors. As shown, the full width of each pulse was <10 ns. This indicated that the TCT-Acqiris digital system provided a fast response. The signal of the 25- μm -thick detector exhibited slightly jagged noise and a long tail compared with the 140- μm -thick detector. The rise time was shorter for the 25- μm -thick detector than for the 140- μm -thick detector. This was due to the drift velocity of the electron carriers in the diamond crystal. For the same detector, the pulse height was significantly higher for the alpha source than for the gamma source. This indicates that pulse-height analysis can be used for the discrimination of γ -rays and neutrons.

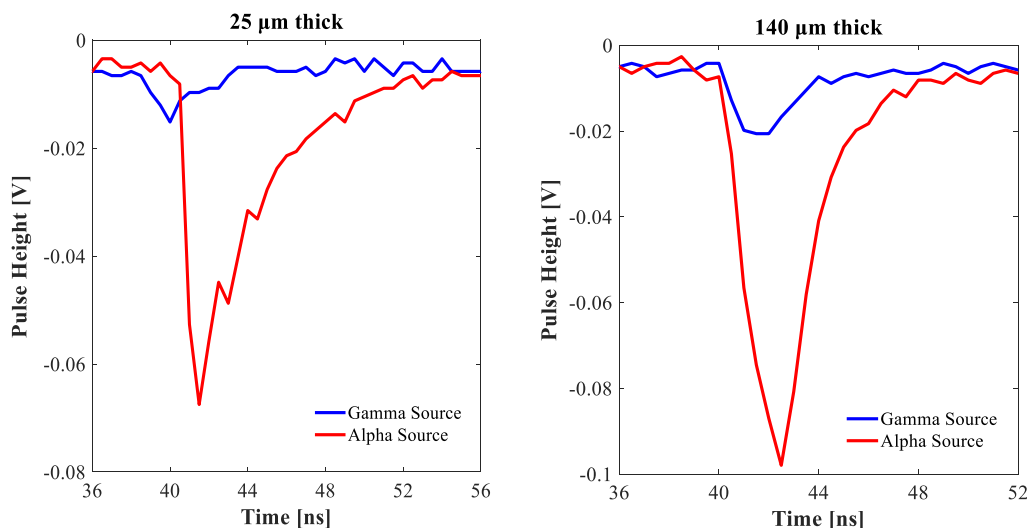


Figure 5.1: Typical signals of an ^{241}Am alpha source from TCT-Acqiris digital system with the 25- and 140- μm -thick CVD diamond detectors under bias voltages of 20 and 80 V, respectively.

Figures 5.2 and 5.3 shows the flowchart and schematic of the pulse-height analysis method used in this study, respectively. In the pulse-height analysis method, the original data are read; next, the peak height and position of each pulse are evaluated. Then, by setting the pulse-height threshold and section window of the pulse peak, the data filtering of the pulse top position and pulse height is conducted. Finally, Construct energy spectrum using pulse-height data.

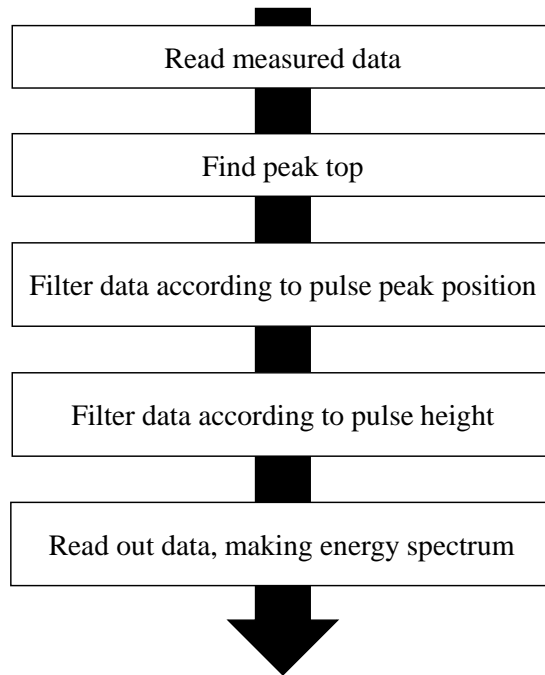


Figure 5.2: Flowchart of the pulse-height analysis method used in this study.

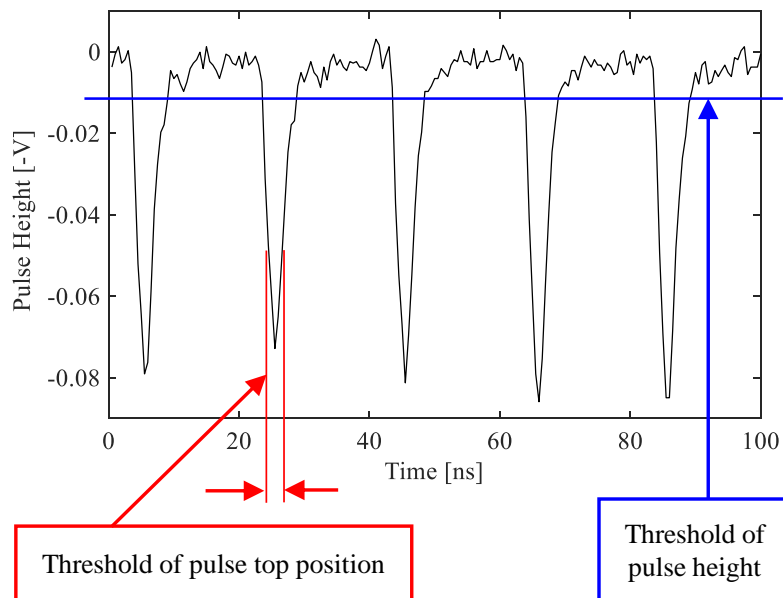


Figure 5.3: Pulse-height analysis method.

5.2 Experiment

5.2.1 Energy resolution

Figure 5.4 shows the experimental layout for energy-resolution measurement using the TCT-Acqiris digital system. The mixed alpha-source and vacuum chamber were identical to those used in the aforementioned CCE experiments. For signal readout, the TCT-Acqiris digital system was used.

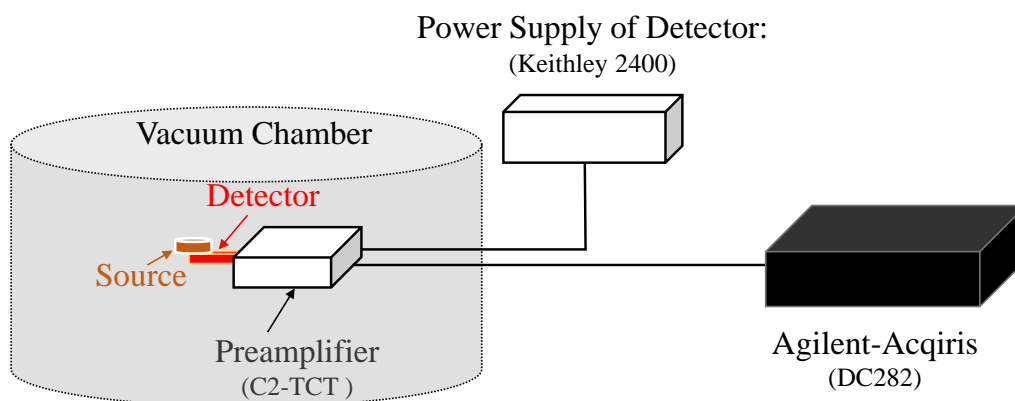


Figure 5.4: Measurement system of energy resolution using the TCT-Acqiris digital system.

5.2.2 High-dose rate γ -ray response experiment

A high-dose rate γ -ray response experiment with the TCT-Acqiris digital system was conducted at the ^{60}Co γ -ray irradiation facility of KURNS. The detectors were placed 30 cm from the center of the ^{60}Co source and exposed to intense γ -rays at a dose rate of 107 Gy/h. The 25- and 140- μm -thick detectors were biased at 20 and 80 V, respectively.

5.2.3 Thermal-neutron response and detection efficiency

Thermal-neutron response and detection efficiency measurement experiments with the TCT-Acqiris digital system were conducted using the KEK graphite pile. Excluding the detection system, the experimental setup was identical to that for the analog system.

5.2.4 Application of TCT-Acqiris digital system using compact accelerator-based neutron sources

The irradiation experimental measurements were performed at the electron linear accelerator facility of KURNS to investigate the responses of the diamond detectors in a mixed source composed of neutrons and a strong background of γ -rays. The Kyoto University Compact Accelerator-based Neutron Source (KURNS-LINAC) was used in the experiment. The KURNS-LINAC was installed at the Kyoto University Research Reactor Institute for Nuclear Science as a neutron source for generating pulsed neutrons in 1965. It is an L-band (1.3 GHz) accelerator, and the electron beam is generated by a thermionic gun. The maximum energy of the electron beam is 46 MeV, the pulse width can be changed from 2 to 4 μ s, the maximum peak current is approximately 500 mA, and the maximum pulse repetition frequency is approximately 100 Hz [34].

Figure 5.5 shows the experimental setup. For the present measurements, the energy of the electron beam was 30 MeV, the peak current range was 180 mA~4 A, the pulse repetition frequency range was 10~100 Hz, and the pulse-width range was 0.1~4 μ s. A water-cooled target composed of 12 sheets of Ta plates was set in a 5-cm-diameter and 6-cm-long cylindrical titanium case. The total thickness of the Ta plates was 29 mm, and the target was set at the center of a 20-cm-diameter and 30-cm-high cylindrical water tank, which was used to obtain thermal neutrons. To suppress photons, the detectors were surrounded by lead bricks ($5 \times 10 \times 20$ cm³). The detector was placed 95 cm below the center of the water tank. The measurements were performed at room temperature. The analog system used in the thermal-neutron experiment and the TCT-Acqiris digital system were used in this experiment. For comparison, the thermal-neutron flux in the KURNS target room was measured using gold-foil activation detectors via the Cd difference method [59].

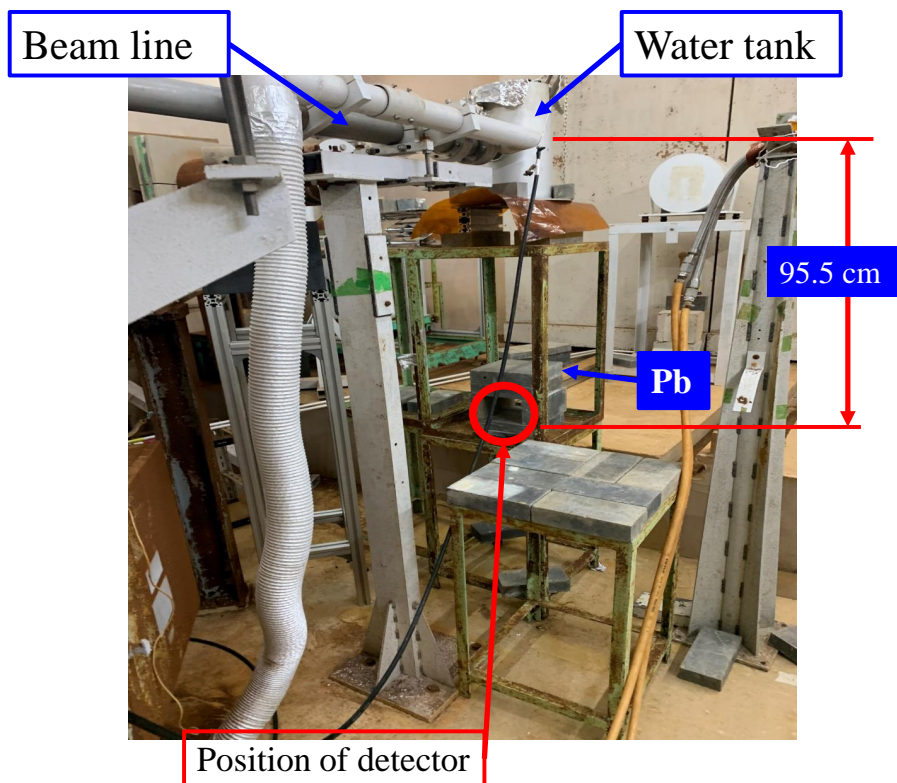
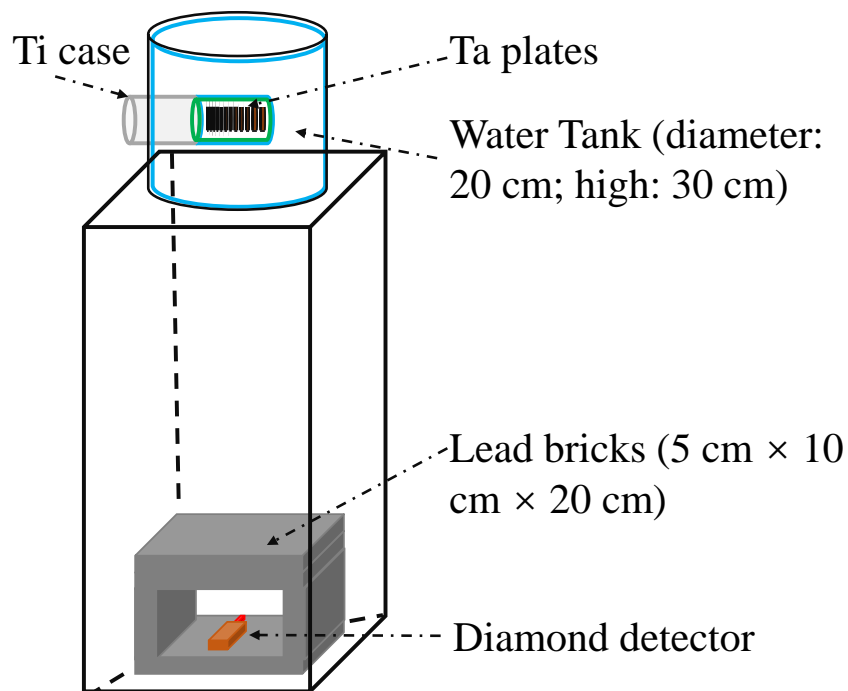


Figure 5.5: Experimental setup in the target room.

5.3 Simulation

The simulation of the electron-beam irradiation experiment was conducted using the PHITS Monte Carlo code (version 3.20). The EGS5 option implemented in the PHITS code was used to calculate the electromagnetic cascade reaction in the diamond detectors. The simulated results were compared with the experimental results. In the simulation, the detectors were modeled using the design report provided by CIVIDEC. Figure 5.6 shows the geometry of the simulation.

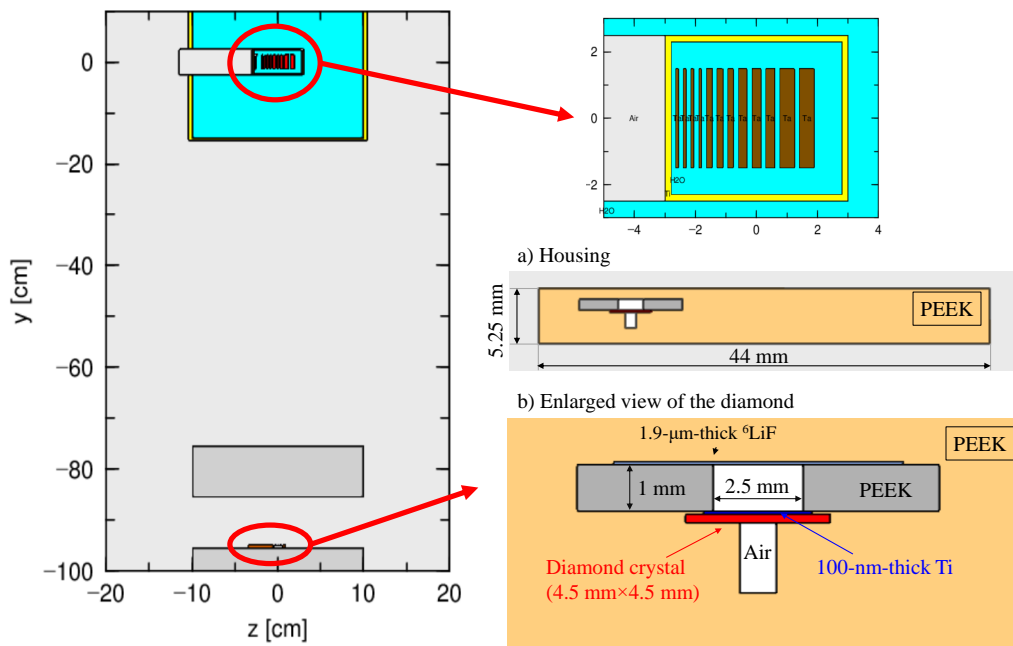


Figure 5.6: Geometry of the simulation.

5.4 Results and discussion

5.4.1 Energy resolution

Figure 5.7 shows the energy spectra of the mixed alpha-source for the two diamond detectors with the TCT-Acqiris digital system. The spectra exhibited three peaks with energies of 3.183, 5.486, and 5.805 MeV. A 3.9% energy resolution of the 25- μm -thick detector were measured under ^{241}Am alpha-source, while those for the 140- μm -thick detector were 2.8%, respectively. Comparing with the analog system, the energy resolution become worse; nonetheless, it was sufficient for n/ γ discrimination.

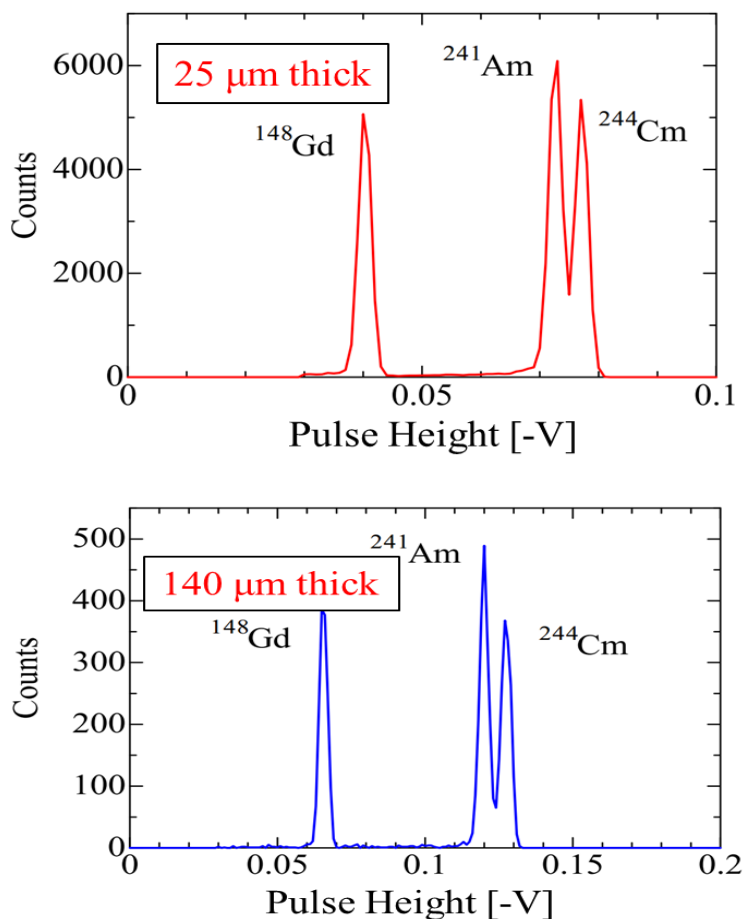


Figure 5.7: Energy spectra of the mixed alpha-source for the two diamond detectors with the TCT-Acqiris digital system. The bias voltages of the 25- and 140- μm -thick detectors were 20 and 80 V, respectively.

5.4.2 High-dose rate γ -ray response experiment

The pulse-height distributions for the intense γ -ray irradiation experiments at KURNS are presented in Fig. 5.8. The pulse height for the 25- μm -thick diamond detector was far smaller than that for the 140- μm -thick detector. For both detectors, a peak at approximately -0.016 V was observed in every spectrum, in contrast to the analog system (Fig. 4.10). The reason for this is that a threshold was set in the experiments using the analog system, causing small pulses to be lost.

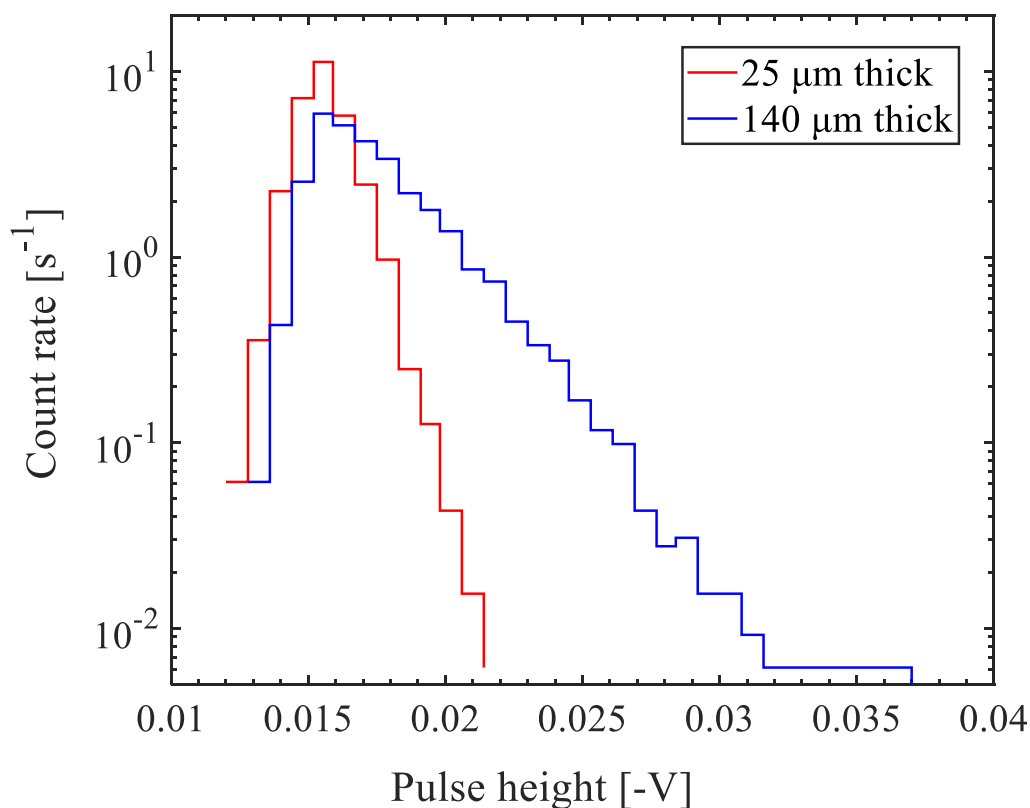


Figure 5.8: Pulse-height distributions obtained via the TCT-Acqiris digital system with the 25- and 140- μm -thick diamond detectors for ^{60}Co γ -rays with a dose rate of 107 Gy/h.

To determine whether a pile-up effect occurred, the shapes of the largest-pulse height signals obtained via the TCT-Acqiris digital system with the 25- and 140- μm -thick diamond detectors were examined, as shown in Fig. 5.9. The pulse shapes were identical to those shown in Fig. 5.1, indicating that

there was no pile-up effect, even under irradiation with a 107-Gy/h dose rate of γ -rays using the TCT-Acqiris digital system.

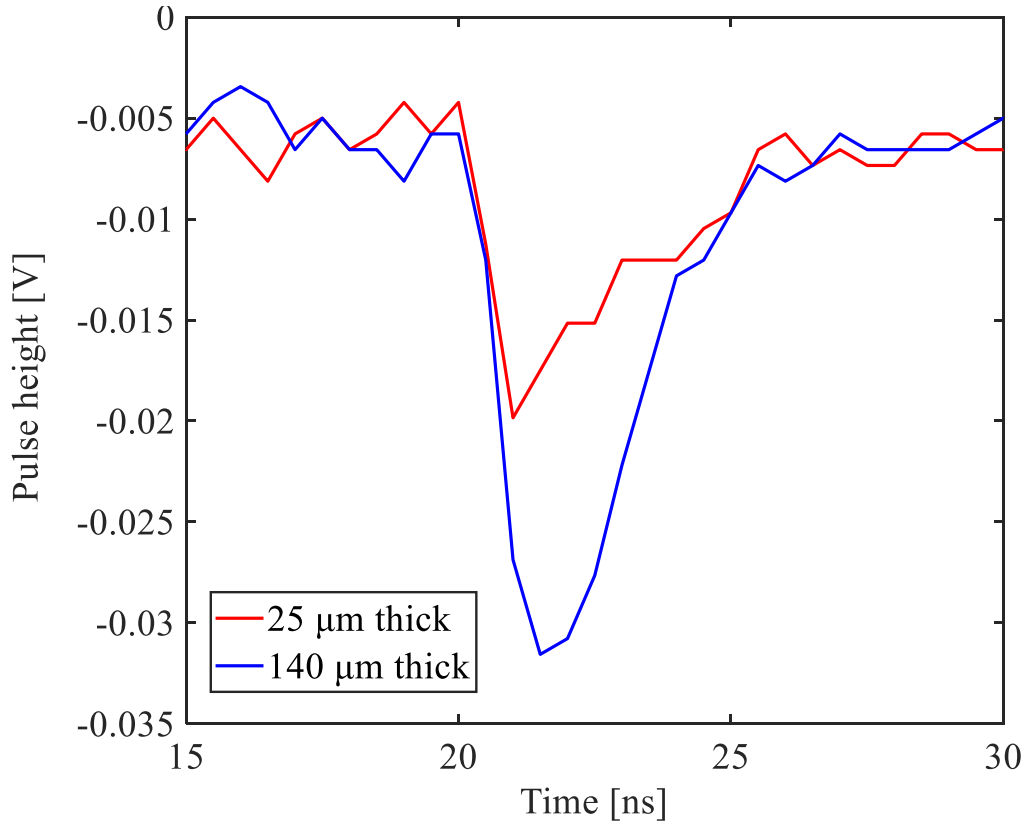


Figure 5.9: Largest-pulse height signals of the electrons from the TCT-Acqiris digital system with the 25- and 140- μm -thick diamond detectors.

Figure 5.10 shows the typical signal shape of the alpha particles from the analog system with the 25- μm -thick diamond detector. The full pulse width for the analog system was 3 μs , whereas it was only 10 ns for the TCT-Acqiris digital system. The TCT-Acqiris digital system provided a fast response (300 times faster than the analog system). As mentioned in Section 4.3.3, the pile-up effect occurred with dose rates up to 107 Gy/h ($8.2 \times 10^{10} \text{ cm}^{-2}\text{s}^{-1}$) when the analog system was used. However, for the 25- μm -thick diamond detector, the maximum deposition energy was $<2 \text{ MeV}$. This indicates that even with the analog system, the gamma and neutron events could be separated.

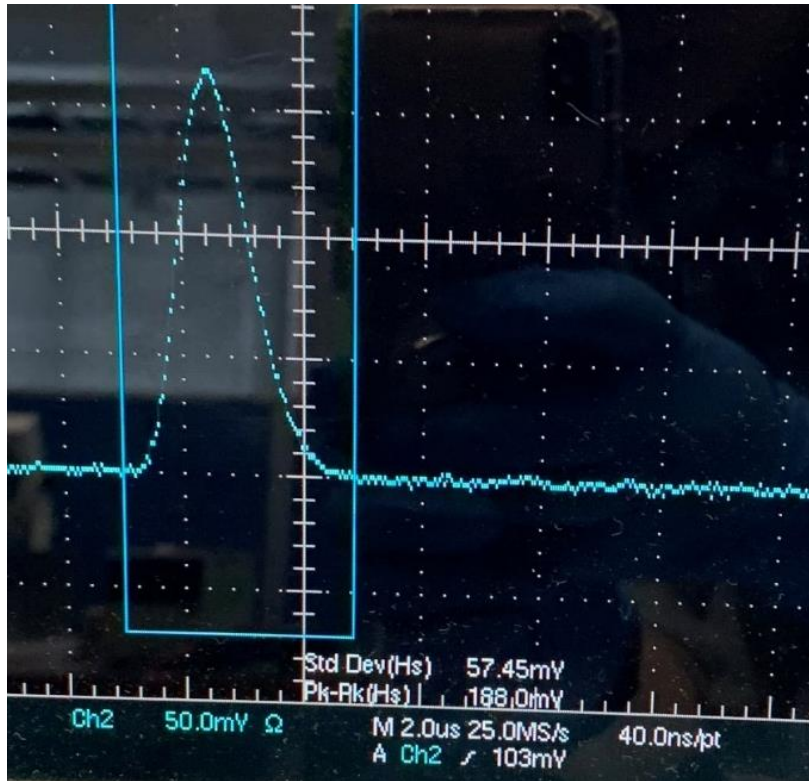


Figure 5.10: Typical signal shape of the alpha particles for the analog system with the 25- μm -thick diamond detector.

Because the maximum deposition energy of γ -rays depends on the total number of incident γ -rays, it is important to determine the n: γ flux ratio for n/ γ discrimination.

Accordingly, the maximum detection dose rate of γ -rays was estimated while the TCT-Acqiris digital system was used. In the experiment using the analog system, the measurement time was 300 s. If an uncertainty of 10% (1%) is expected for neutron measurement, at least 100 (10000) counts should be measured in 300 s in this situation. The thermal-neutron detection efficiency was 1×10^{-3} ; thus, the minimum detection flux for neutrons is $100 \div 300 \text{ s} \div (1 \times 10^{-3} \times 0.1 \text{ cm}^2) = 3.3 \times 10^{-4} \text{ cm}^{-2}\text{s}^{-1}$. Hence, the n: γ flux ratio is $1 : 2.5 \times 10^6 (1 : 2.5 \times 10^4)$. Therefore, for the analog system, the maximum detection capability for gamma rejection was 107 Gy/h, while the experimental n: γ flux ratio was $1 : 2.5 \times 10^6 (1 : 2.5 \times 10^4)$. Because the full width of the TCT system was 300 times smaller than that of the analog system, for the TCT system, the maximum detection capability for gamma

rejection was $107 \text{ Gy/h} \times 300 = 32 \text{ kGy/h}$, while the experimental $n:\gamma$ flux ratio was $1 : 2.5 \times 10^6$.

5.4.3 Thermal-neutron response and detection efficiency

The simulated and experimental results for the analog system and TCT digital system with the $25\text{-}\mu\text{m}$ -thick CVD diamond detector are shown in Fig. 5.11. The experimental and simulated spectra agreed well.

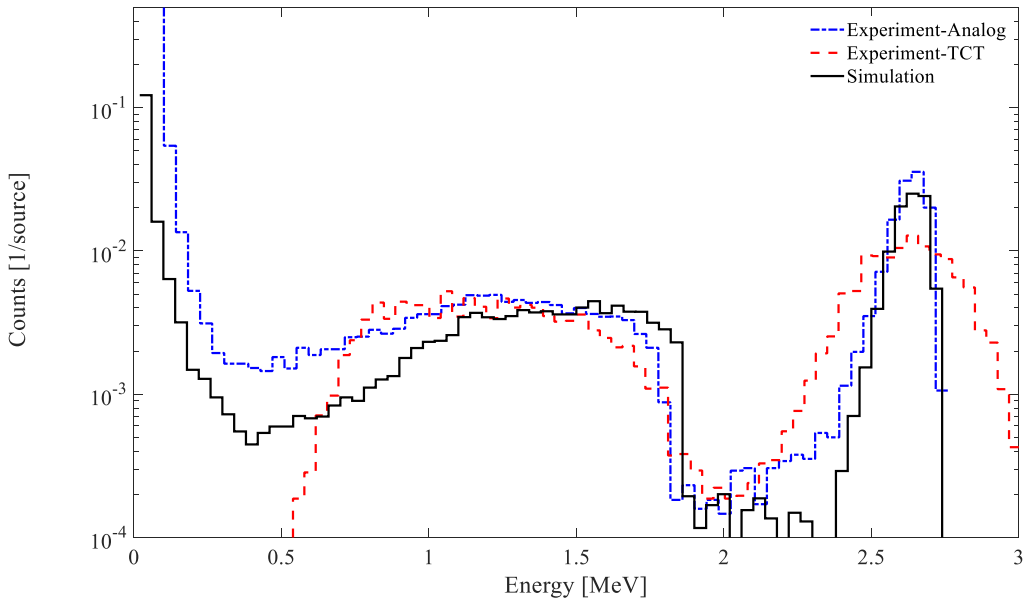


Figure 5.11: Measured pulse-height distributions for thermal-neutron detection in the KEK graphite pile with the $25\text{-}\mu\text{m}$ detector.

Compared with traditional analog detection systems, broader triton peak was observed for the TCT-Acqiris digital system, as shown in Fig. 5.11, indicating a lower energy resolution for neutron detection. The electron distribution was lost during the pulse-height analysis process. TCT-Acqiris digital system exhibited a fast response for detection. Despite its poor energy resolution, the TCT-Acqiris digital system is effective for n/γ discrimination when a proper threshold is set.

Table 5.1 presents the measured count rate and efficiency for the TCT-Acqiris digital system. When the distance between source and the surface of detector was set as 47 cm, the thermal-neutron detection efficiency of the $25\text{-}\mu\text{m}$ -thick diamond detector with the TCT-Acqiris digital system was

$1.00 \times 10^{-3} \pm 9 \times 10^{-5} \text{ cm}^2$. When the distance was set as 70 cm, the thermal-neutron detection efficiency of the 25- μm -thick diamond detector with the TCT digital system was $9.85 \times 10^{-4} \pm 1.09 \times 10^{-4}$. The thermal-neutron detection efficiencies were almost identical between the analog system and the TCT digital system. Even when the distance was increased to 70 cm, only a small ($\sim 5\%$) difference was observed in the measured efficiency. The similar detected efficiencies between the analog system and the TCT digital system indicate that the pulse-height processing method of the TCT-Acqiris digital system is reasonable.

Table 5.1: Measured thermal-neutron fluxes and efficiencies for the TCT-Acqiris digital system (25 μm).

Distance	Thermal neutron flux [$\text{cm}^{-2}\text{s}^{-1}$]	Count rate [s^{-1}]	Efficiency
47 cm	$1168 \pm 8.46\%$	$0.117 \pm 0.87\%$	$1.00 \times 10^{-3} \pm 9 \times 10^{-5}$
70 cm	$666 \pm 8.63\%$	$0.06 \pm 6.97\%$	$9.85 \times 10^{-4} \pm 1.1 \times 10^{-4}$

For estimating the allowable maximum neutron detection flux, the dead time was taken into account. The dead time τ is defined as follows: $n - m = nm\tau$ [60], where n represents the true interaction rate, and m represents the recorded count rate. Because the full pulse width in the TCT system is < 10 ns, the dead time (τ) can be assumed as 10 ns. An acceptable dead-time fraction of 5% can be also assumed, the true interaction rate of $5.26 \times 10^6 \text{ s}^{-1}$ is obtained. Through dividing by the thermal-neutron detection efficiency, the allowable maximum detection flux without pile-up effects was estimated as $5.26 \times 10^6 \text{ s}^{-1} \div 1.0 \times 10^{-3} \div 0.1 \text{ cm}^2 = 5.26 \times 10^{10} \text{ cm}^{-2}\text{s}^{-1}$.

It takes a long time to measure low-flux thermal neutrons; however, the low efficiency and narrow pulse width (< 10 ns) of the diamond detector provide a high-flux detection capability.

5.4.4 Application of TCT-Acqiris digital system using compact accelerator-based neutron sources

Figures 5.12 and 5.13 show the pulse-height distributions of TCT-Acqiris digital system with the 25- and 140- μm -thick diamond detectors, respectively, based on the KURNS-LINAC accelerator. The energy of the electron beam was 30 MeV, the pulse width was 4 μs , the maximum peak current was approximately 180 mA, and the pulse repetition frequency was approximately

10 Hz. In Fig. 5.11, a continuous region and a sharp peak corresponding to alpha particles and tritons from the ${}^6\text{Li}(n, \alpha){}^3\text{H}$ reaction are observed. As the alpha particles underwent larger energy losses in air, the peak corresponding to alpha particles was broader than the peak corresponding to tritons. The dominant interaction between the γ -rays and diamond was Compton scattering, and both CVD diamond detectors were sufficiently thin that the Compton-scattered photons and electrons easily escaped from them without full energy deposition. Thus, the pulse corresponding to γ -rays was significantly smaller than those corresponding to alpha particles and tritons.

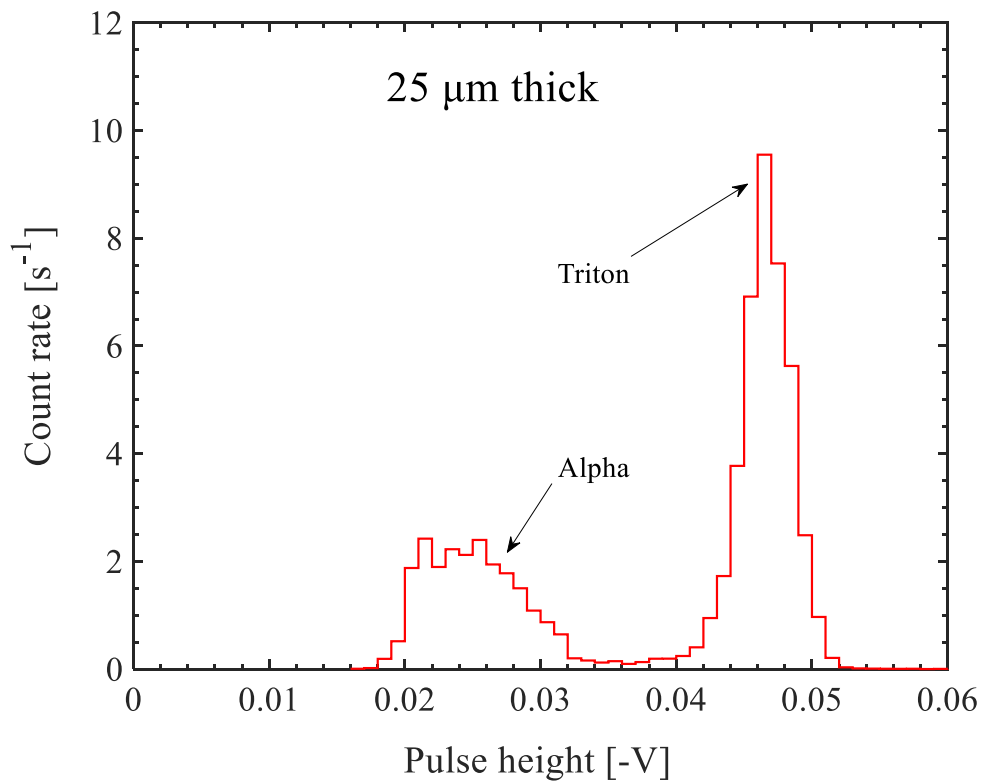


Figure 5.12: Pulse-height distribution of TCT-Acqiris digital system with the 25- μm -thick CVD diamond detector for a mixed source based on the electron linear accelerator.

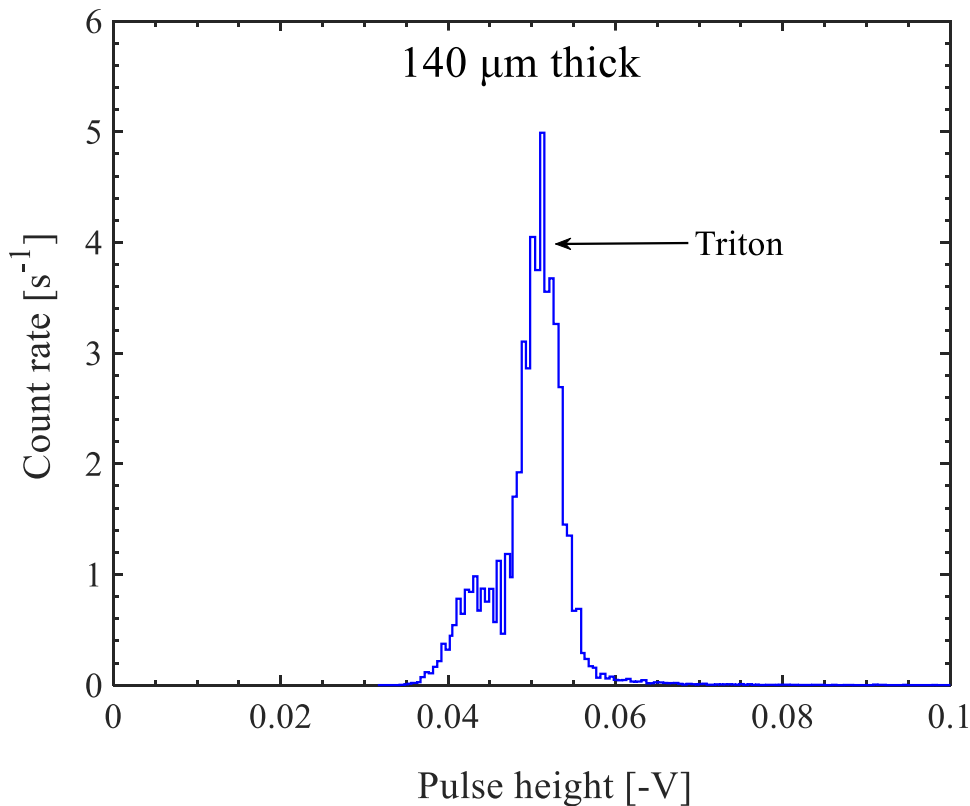
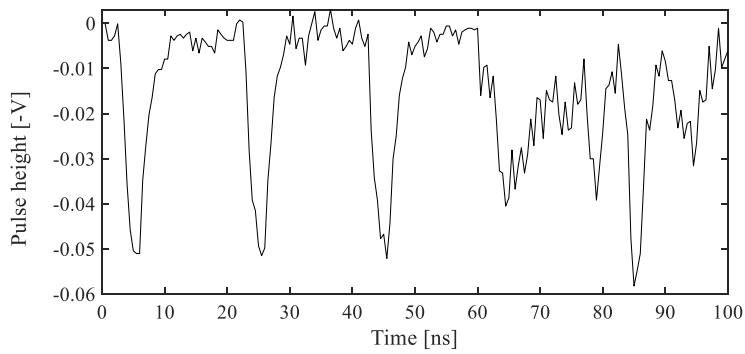
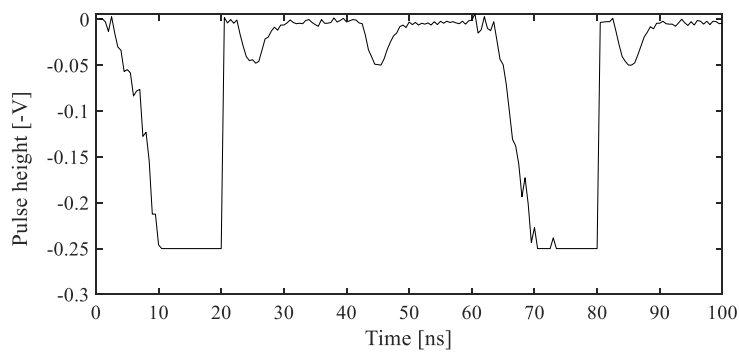


Figure 5.13: Pulse-height distribution of TCT-Acqiris digital system with the 140- μm -thick diamond detector for a mixed source based on the electron linear accelerator.

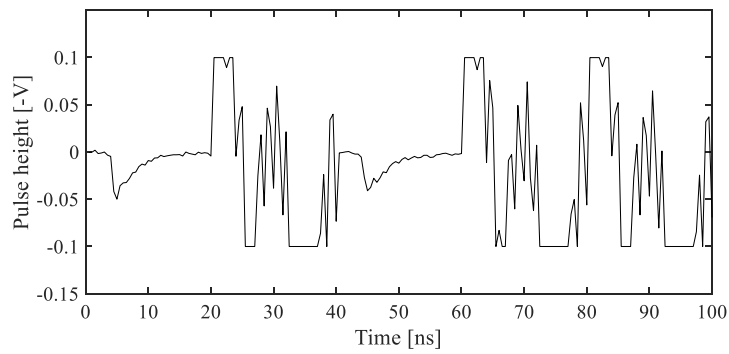
Owing to the long cables used in the experiment, the electron-distribution part was lost in the spectrum. Thus, the electronic noise and electron distribution produced by gamma events were not reflected in the pulse-height distributions. The spectra of the alpha particles and tritons could be separated from the gamma background through pulse-height analysis for the 25- μm -thick diamond detector. However, for the 140- μm -thick diamond detector, because of the interference of the background noise in the pulse-height distributions, the peaks corresponding to alpha particles and tritons could not be separated well. The signal was affected by the background noise—particularly under the irradiation of the high-intensity accelerator. The typical noise shape is shown in Fig. 5.14. Some of the noise has a regular shape and repeats, making it easy to remove. However, if the shape of the noise resembles the topmost curve in Fig. 5.14, the noise may be mistaken for a pulse.



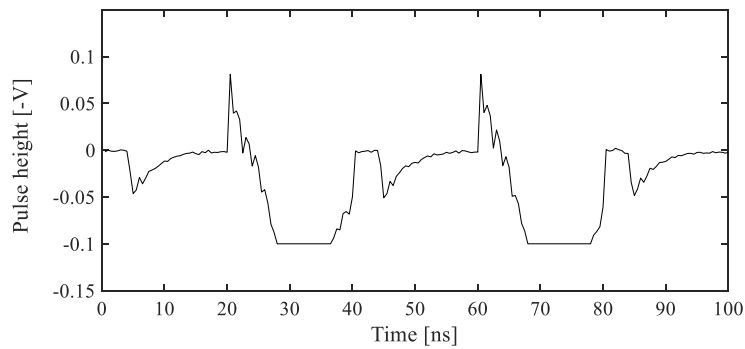
140- μm -thick
Beam information
 Width: 4 μs
 Repetition: 10 Hz
 Peak current: 180 mA



140- μm -thick
Beam information
 Width: 0.1 μs
 Repetition: 10 Hz
 Peak current: 4 A;



25- μm -thick
Beam information
 Width: 0.1 μs
 Repetition: 100 Hz
 Peak current: 4 A



25- μm -thick
Beam information
 Width: 0.1 μs
 Repetition: 10 Hz
 Peak current: 4 A

Figure 5.14: Typical noise shape.

Therefore, alpha-particle pulses were sometimes mistaken for triton pulses in the pulse-height analysis. Hence, a pulse-area analysis was performed for discriminating the alpha particles and tritons. Figure 5.15 shows the area distribution for the 140- μm -thick diamond detector. The triton peak is clearly observed, indicating that pulse-area analysis can be also used for neutron detection.

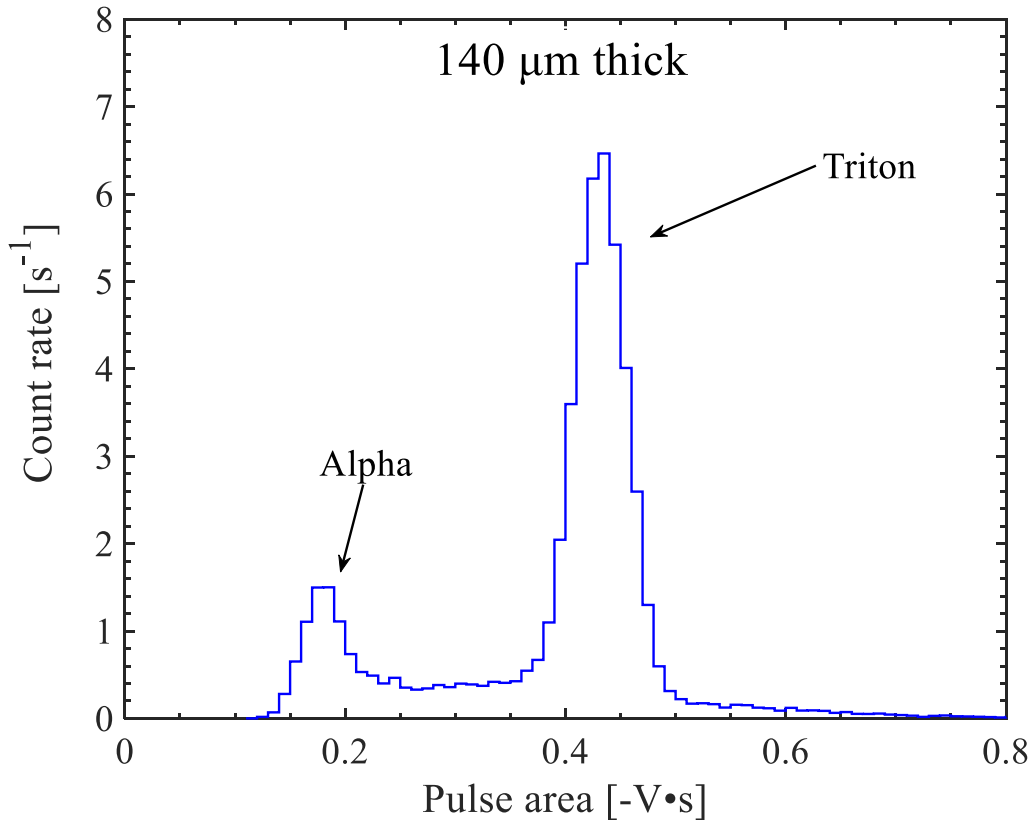


Figure 5.15: Pulse-area distribution of TCT-Acqiris digital system with the 140- μm -thick diamond detector for a mixed source based on the electron linear accelerator.

The 25- and 140- μm -thick CVD diamond detectors exhibited slightly different energy resolutions (8.4% and 8.6%, respectively) at the triton peak under the same signal-processing conditions. Nonetheless, the energy resolution was sufficient for discriminating gamma events from neutron events through analysis of the pulse height and area.

In the measurement based on the KURNS-LINAC accelerator, different

beam conditions were used. The beam information and the count rate for the different conditions are presented in Table 5.2. For the TCT-Acqiris digital system, the triton detection efficiencies for the 25- and 140- μm -thick detectors were 5.32 ± 0.97 and $5.65 \pm 0.81 \mu\text{A}^{-1}\text{s}^{-1}$, respectively. For the analog system, the triton detection efficiency for the 25- μm -thick detector was $5.95 \pm 0.03 \mu\text{A}^{-1}\text{s}^{-1}$.

Table 5.2: Beam information and the count rate.

Detector system		Beam information				Count rate [s^{-1}]
		Width [μs]	Average current [μA]	Peak current [A]	Repetition [Hz]	
TCT-Acqiris system	25 μm	4	7.01	0.18	10	40.01 ± 4.44
		0.1	3.5	4	10	18.42 ± 2.66
		0.1	3.56	4	10	18.00 ± 2.62
		0.1	35.78	4	100	188.21 ± 0.27
	140 μm	4	6.91	0.18	10	40.18 ± 4.66
		0.1	3.5	4	10	19.24 ± 3.33
Aanlog-25 μm		0.1	3.5	4	10	20.84 ± 0.11

Figure 5.16 shows count rate as a function of average current under different beam conditions. The count rate is linearly related to the average current, even under the beam condition of 0.1- μs -width and 100-Hz-repetition-frequency. This indicates that the diamond detection system can remain stable even when the electron-beam current increases rapidly.

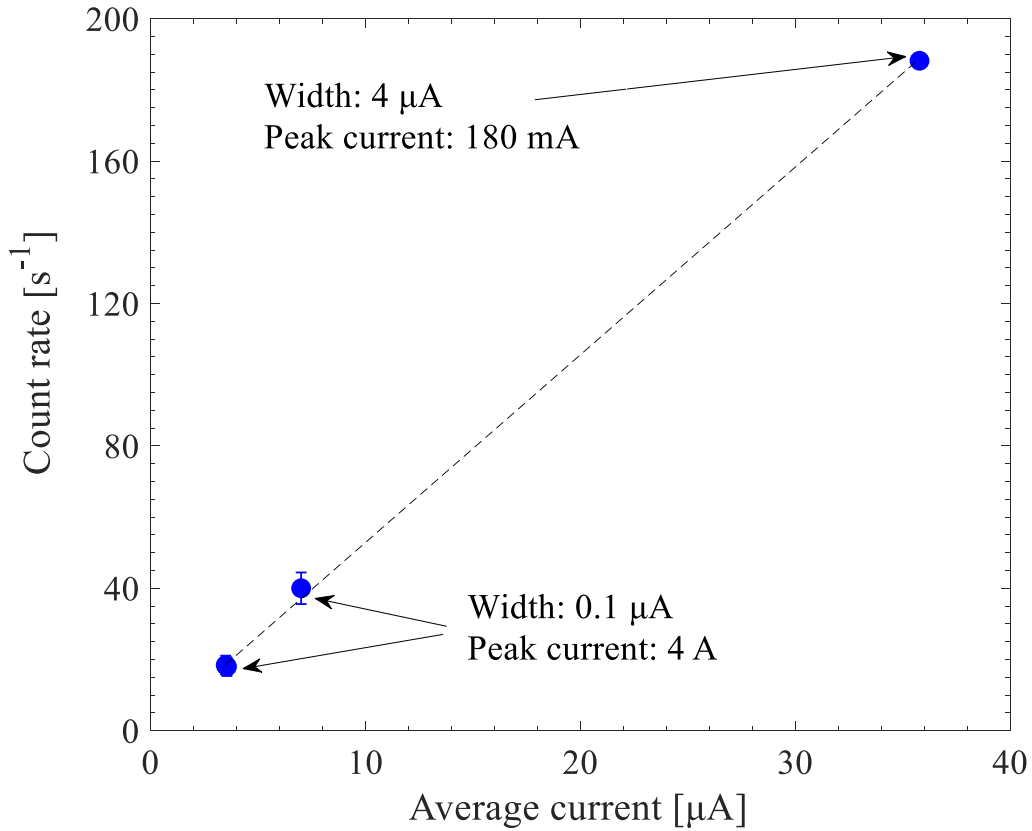


Figure 5.16: Count rate as a function of average current under different beam conditions.

As the thermal-neutron efficiency was previously measured (Section 4.3.4), the thermal-neutron flux was estimated according to the efficiency and count rate. The thermal-neutron flux was calculated as $1.86 \times 10^5 \pm 0.159 \times 10^5 \text{ cm}^{-2}\text{s}^{-1}$ at an average current of $3.5 \mu\text{A}$. The thermal-neutron flux measured by the gold-foil activation detectors was $2.01 \times 10^5 \text{ cm}^{-2}\text{s}^{-1}$ at an average current of $3.5 \mu\text{A}$. The fluxes measured by the two types of detectors agreed well.

In summary, the diamond detector was successfully used in a mixed environment based on compact accelerator-based neutron sources. Using the TCT-Acquis digital system, a pulse-height analysis can be performed to distinguish neutrons from γ -rays. Compared with the gold-foil activation detectors, the diamond detector provided reliable results for neutron detection.

Chapter 6

Application of response functions of Bonner sphere spectrometer

The Bonner sphere spectrometer (BSS) is used to characterize neutron fields ranging from the thermal energy region to hundreds of MeV. The measurement principle is to use thermal-neutron detectors and surround them with neutron moderators of different thicknesses. This requires the calculation or measurement of the responses of these detector/moderator combinations to neutrons from primary monoenergetic sources. One of the main advantages of the BSS system is its isotropic response to neutrons resulting from its symmetric spherical shape.

Four Bonner spheres were used in this study, as shown in Fig. 6.1.

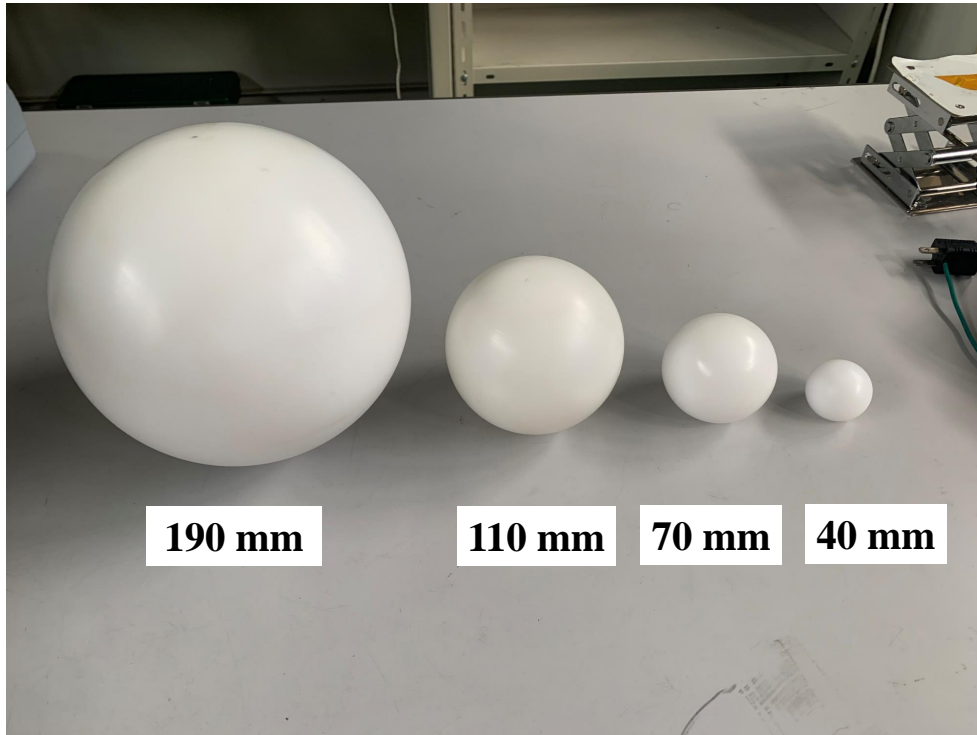


Figure 6.1: Spheres used in this study: 40, 70, 110, and 190 mm (in diameter).

6.1 Simulation of response functions of BBS

The PHITS code (version 3.2.4) was used to simulate the responses of the diamond detectors to γ -rays. Photons, electrons, and positrons were transported using the EGS5 algorithm. A cutoff energy of 10^{-4} eV was used for the transport of neutrons, but a cutoff energy of 1 keV was used for photons, electrons, and other ions. The t-deposit tally for the cell of the diamond crystal was used for calculating the energy-deposition spectrum.

The BSS consisted of a set of four polyethylene (density $\rho_{PE} = 0.96$ g/cm³) spheres with outer diameters of 40, 70, 110, and 190 mm. The material compositions and densities of the Bonner spheres used in the PHITS simulation are presented in Table 6.1. The responses of the BSS to neutrons were calculated for a broad parallel beam geometry with 42 values of monoenergetic neutrons in the range of 1.0×10^{-10} to 500 MeV.

Table 6.1: Material compositions and densities of the Bonner spheres used in the PHITS simulation.

Material	Element	Density [g/cm ³]	Atom ratio
Polyethylen	C	0.96	1
	H		1

A disk parallel source was used. For the bare diamond detector, the source area was equal to the size of the diamond detector. For the other four diamond detectors with Bonner spheres, the source area was equal to the surface area of the Bonner sphere. Figure 6.2 presents an overview of the simulated geometric setup.

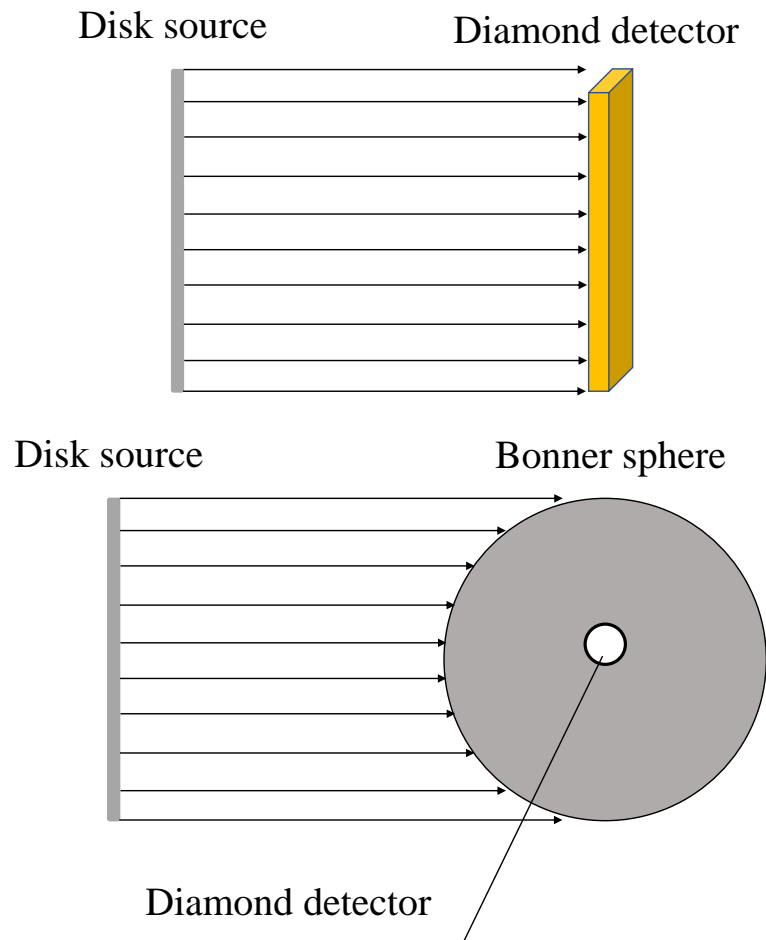


Figure 6.2: Simulated geometric setup.

Figure 6.3 shows the response function of the BSS system expressed as the number to unit source with respect to the neutron energy.

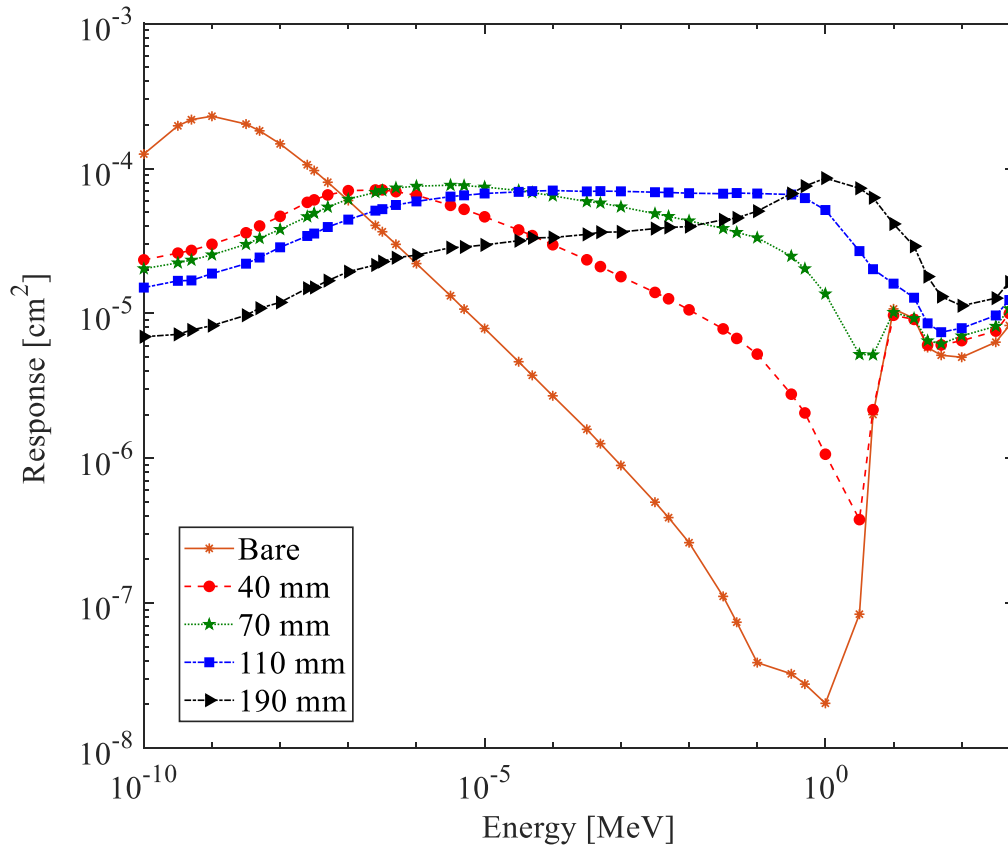


Figure 6.3: Neutron response of the BSS system with respect to the neutron energy.

The response function of bare diamond detector exhibited a steep decline and had its peak position at the lowest energy. A larger Bonner sphere corresponded to a higher energy of the peak position.

6.2 Application of response functions of Bonner sphere spectrometer

6.2.1 Experiment

(i) Validating neutron response functions of bare diamond detector using graphite pile

The response to thermal neutrons was obtained, i.e., the pulse-height spectrum and detection efficiency, using the thermal-neutron field at KEK. The source setting was identical to that shown in Fig. 4.3. The diamond detector was set at the surface of the graphite pile, 95 cm from the source. Figure 6.4 shows the experimental setup. The TCT-Acqiris digital detection system was used.

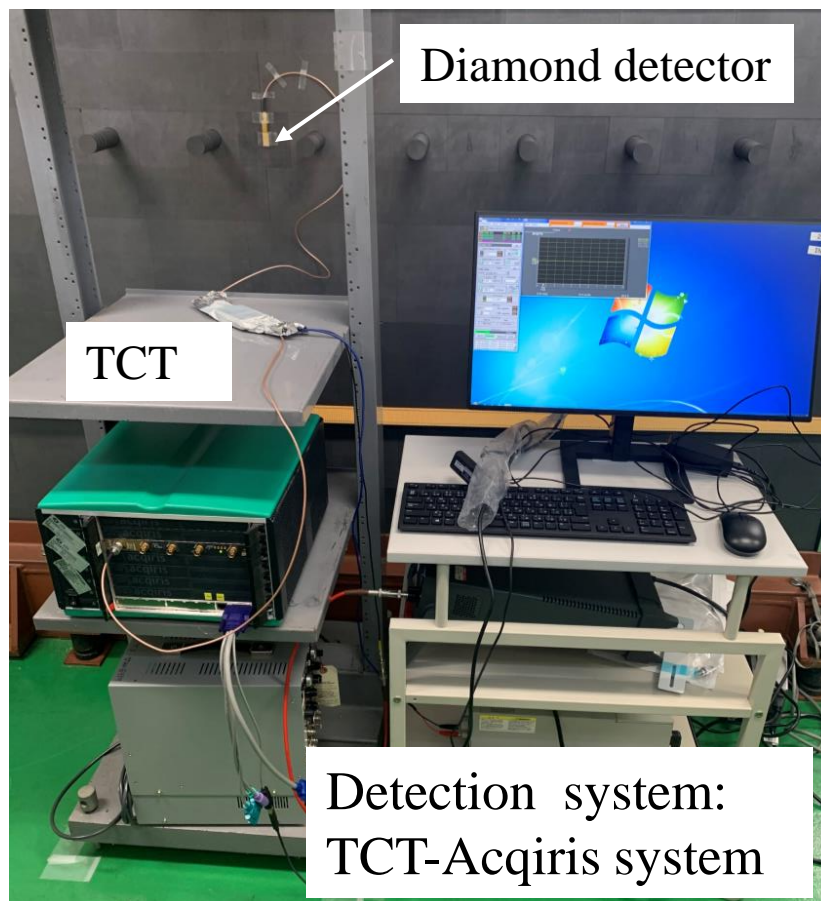


Figure 6.4: Experimental setup in the graphite pile.

(ii) Validating neutron response functions of BSS using fast-neutron source

The measurement accuracy of the BSS in the low-energy range was tested via measurements with a radionuclide source. The measurements were performed in a calibration laboratory at National Institute of Advanced Industrial Science and Technology (AIST) with $^{241}\text{Am-Be}$ and ^{252}Cf sources which were set 20 and 30 cm away from the center of the Bonner sphere, respectively. The emission rates of the $^{241}\text{Am-Be}$ and ^{252}Cf sources were 8.77×10^6 and 1.16×10^7 neutrons per second, respectively. The aforementioned analog detection system was used in the experiment. The experimental setup is shown in Fig. 6.5.

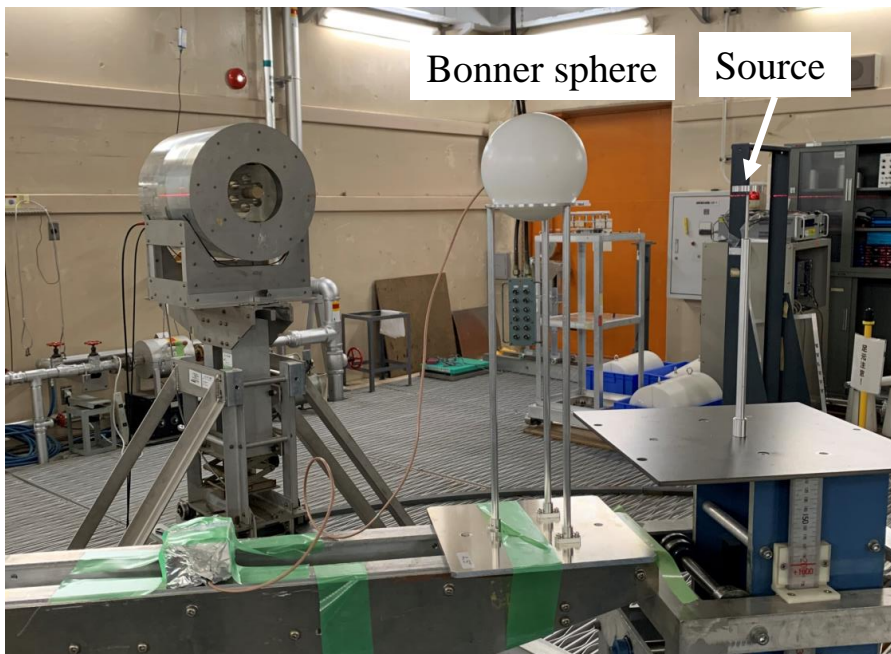


Figure 6.5: Experimental setup with the fast-neutron source at AIST.

(iii) Application of response functions of BSS in STF tunnel

Irradiation experimental measurements were performed in the STF tunnel at KEK to investigate the responses of the diamond detectors with Bonner spheres using an electron-beam source. The detection system was set behind the STF beam dump. The experimental setup in the STF tunnel is shown in Fig. 6.6. For the measurements, the energy of the electron beam was 369.27 MeV, the average current was $1 \mu\text{A}$, the pulse repetition frequency was 5 Hz, and the pulse width was $5.5 \mu\text{s}$. The analog detection system was used.



Figure 6.6: Experimental setup in the STF tunnel.

6.2.2 Simulation

(i) Validating neutron response functions of bare diamond detector using graphite pile

This simulation was similar to that described in Section 4.2; however, the diamond detector was set at the surface of the KEK graphite pile.

(ii) Validating neutron response functions of BSS using fast-neutron source

The PHITS code (version 3.2.4) was used in the simulation. Photons, electrons, and positrons were transported using the EGS5 algorithm. A cutoff energy of 10^{-4} eV was used for the transport of neutrons, but a cutoff energy of 1 keV was used for photons, electrons, and other ions. The t-track tally for the cell of the Bonner sphere was used for calculating the flux.

^{241}Am -Be and ^{252}Cf point sources were set 20 and 30 cm, respectively, from the center of the Bonner sphere. Additionally, a 1-m-thick concrete layer was used for the walls and floor. The room size was $11.5 \times 11.5 \times 11.5$ m³. The covers of the sources, supporting structure, cables, and other equipment were ignored. The room volume was filled with air, similar to the experiment.

(iii) Application of response functions of BSS in STF tunnel

The PHITS code (version 3.2.4) was used in the simulation. Photons, electrons, and positrons were transported using the EGS5 algorithm. A cutoff energy of 10^{-4} eV was used for the transport of neutrons, a cutoff energy of 1 keV was used for photons, and a cutoff energy of 1 MeV was used for electrons and other ions. The t-track tally for the cell of the Bonner sphere was used for calculating the flux. The input file is presented in the Appendix.

6.2.3 Results and discussion

(i) Validating neutron response functions of bare diamond detector using graphite pile

The count rate in the experiment was $3.9 \times 10^{-3} \text{ s}^{-1} \pm 4\%$. For validating the response functions of a bare diamond detector, the flux at the detector position was simulated. The flux spectrum is shown in Fig. 6.7.

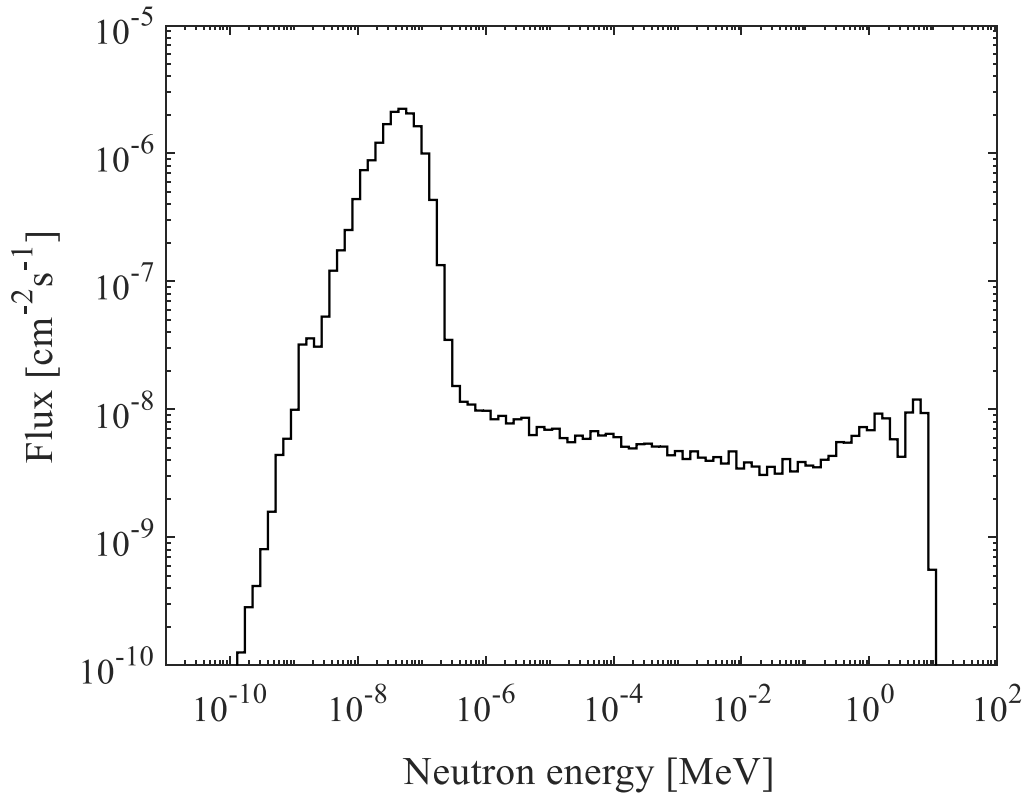


Figure 6.7: Spectrum of thermal neutrons at the surface of the graphite pile.

As shown in Fig. 6.7, the spectrum was mainly composed of thermal neutrons. Considering the energy spectrum and response curve of the bare diamond detector, through the a folding code, the count rate was obtained as $3.6 \pm 3\%$. Comparing the simulated and experimental count rate results revealed a difference of only 7.7%. The experimental source was not perfectly parallel, but the simulated response curve was obtained using a parallel source. This is a potential reason for the difference.

(ii) Validating neutron response functions of BSS using fast-neutron source

The SANDII code [61] was used to obtain neutron flux spectra for diamond-detector measurements. Figures 6.8 and 6.9 show the energy spectra obtained from the SANDII code and PHITS simulation with $^{241}\text{Am-Be}$ and ^{252}Cf sources, respectively.

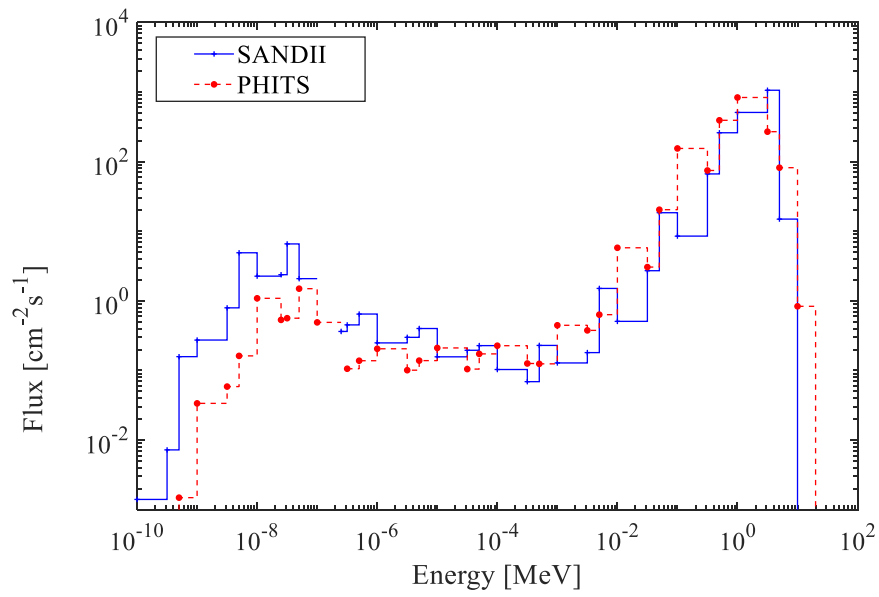


Figure 6.8: Measured and simulated $^{241}\text{Am-Be}$ neutron spectra.

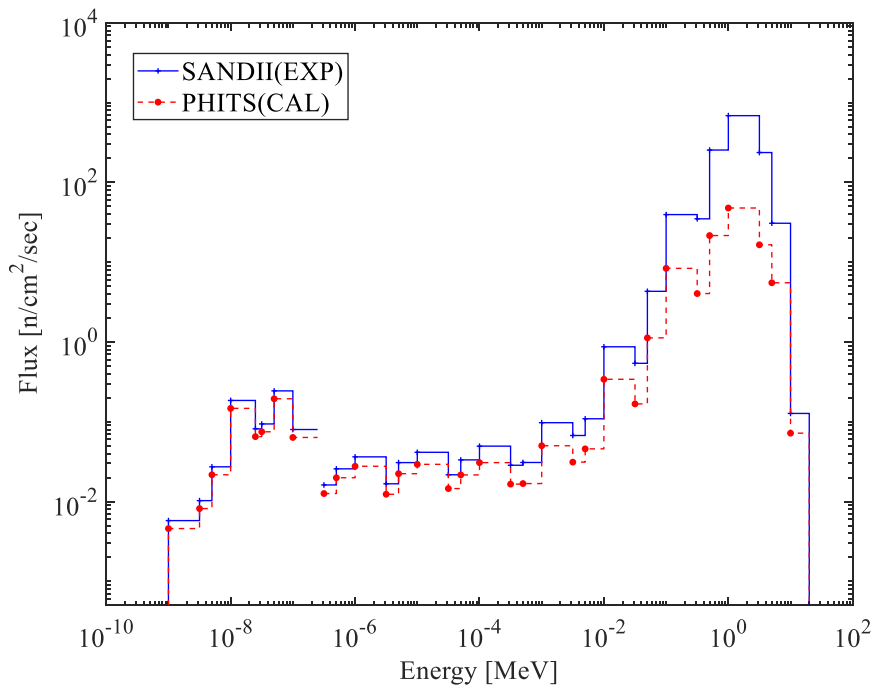


Figure 6.9: Measured and simulated ^{252}Cf neutron spectra.

Using the SANDII unfolding code, the neutron spectra were successfully reproduced. The simulated BSS spectra agreed well with the experimentally measured spectra.

The total neutron flux for the BSS in the PHITS simulation was 1.84×10^3 and $1.06 \times 10^3 \text{ cm}^{-2}\text{s}^{-1}$ for the $^{241}\text{Am-Be}$ and ^{252}Cf sources, respectively. The total neutron flux for the BSS obtained via the SANDII unfolding code was 1.97×10^3 and $1.29 \times 10^3 \text{ cm}^{-2}\text{s}^{-1}$ for the $^{241}\text{Am-Be}$ and ^{252}Cf sources, respectively. This total fluence represented the accumulation of neutrons from the neutron source, including air-scattered neutrons and neutrons reflected by the walls, ceiling, and floor of the room. For the $^{241}\text{Am-Be}$ source, the difference between the simulated and experimental fluxes reached 6.6%, and for the ^{252}Cf source, it reached 17.8%. The reasons for these large differences were as follows: (1) the uncertainty of the count rate was large owing to the small number of experiments and the low detection efficiency and (2) the simulation was not identical to the experiment; e.g., the equipments were ignored in the simulation.

(iii) Application of response functions of BSS in STF tunnel

Figure 6.10 shows the energy spectra for neutron detection using Bonner spheres in the STF tunnel with the 25- μm -thick diamond detector. In the spectra, the triton peaks and alpha distributions are clearly observed. A small peak appeared at 0.2 MeV, which was caused by protons produced in the dump. The electron distribution overlapped with the proton distribution but was separated from the alpha distribution. This indicates that the γ -ray intensity was not high enough to cause the pile-up effect. Moreover, the gamma, neutron, and proton distributions were separated successfully.

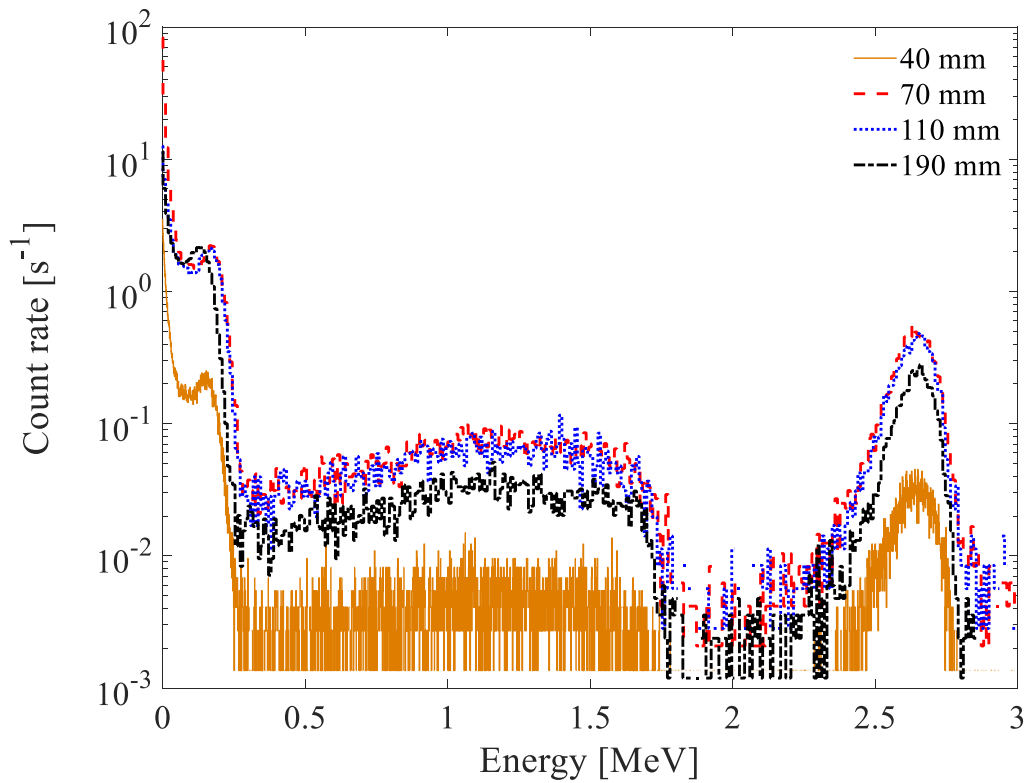


Figure 6.10: Measured energy spectra for neutron detection using Bonner spheres in the STF tunnel with the 25- μm -thick diamond detector.

Figure 6.11 shows the simulated flux distribution for neutrons around the dump in the STF tunnel. Figure 6.12 shows the measured and simulated neutron spectra for the STF tunnel.

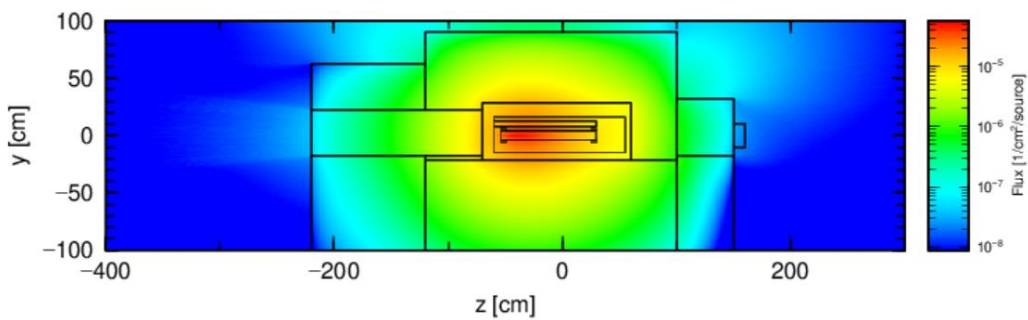


Figure 6.11: Flux distribution for neutrons around the dump in the STF tunnel.

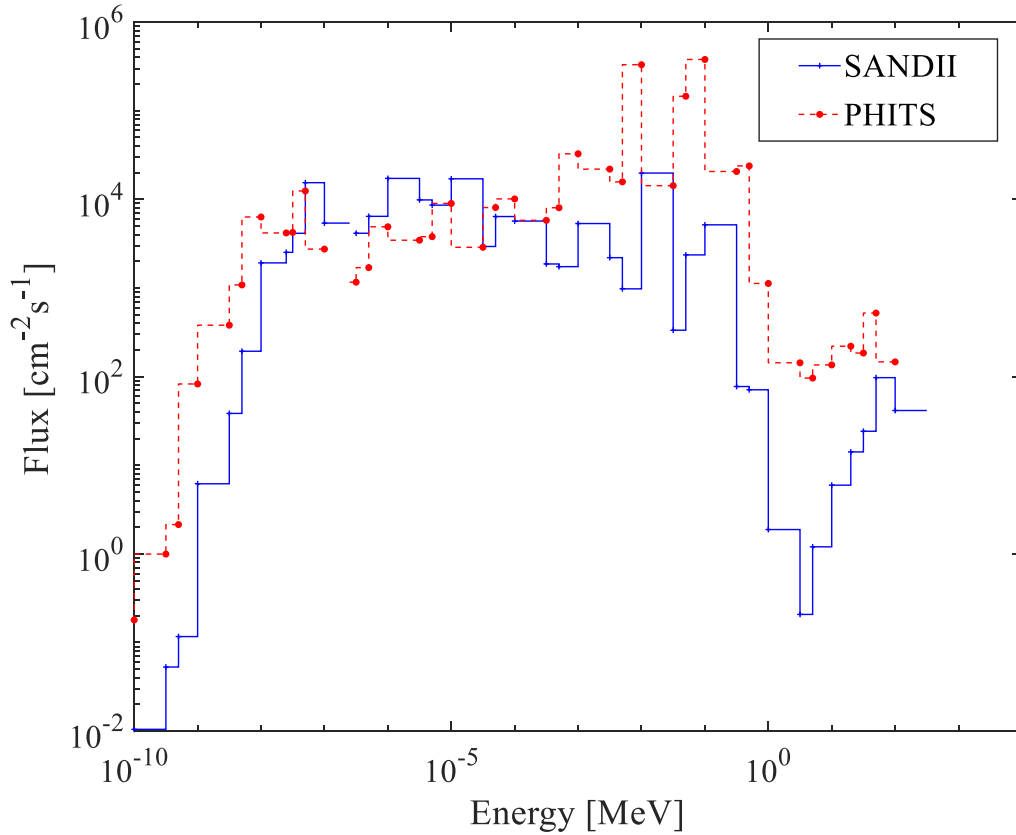


Figure 6.12: Measured and simulated neutron spectra for the STF tunnel.

Using the SANDII unfolding code, the neutron spectra were successfully reproduced. The simulated BSS spectra agreed well with the experimental spectra when the neutron energy was below hundreds of keV. On the other hand, in the high energy region, the unfolded and simulated spectra disagreed. Two peaks at approximately 0.01 and 0.1 MeV appeared in the simulated spectrum which were 100 times higher than that of thermal neutron. In this case, such a large difference should affect the count rate owing to the different responses of the Bonner spheres, as shown in Fig. 6.2. However, the count rate did not differ significantly among the different Bonner spheres, which did not match the simulated spectra. The count rate values obtained experimentally and calculated using the SANDII code were compared, as shown in Table 6.2. The differences between the experimental and calculated count rate values were small, indicating that the unfolding spectra are reliable. Therefore, the neutron flux was $1.6 \times 10^5 \text{ cm}^{-2}\text{s}^{-1}$, and the neutron dose rate was 0.7 mSv/h.

Table 6.2: Count rate for different Bonner spheres.

Diameter [mm]	Count rate (exp) [s ⁻¹]	Count rate (cal) [s ⁻¹]	Cal/Exp
190	4.39	4.35	0.99
110	11.2	8.87	1.06
70	9.70	9.14	0.94
40	6.48	6.54	1.01
0	3.66	3.72	1.01

The reason of the difference between the unfolded and simulated spectra may come from the response function in the energy range, or inaccuracy of the physical models for the photon induced neutron production in PHITS. In order to evaluate the response function of the BBS system, further experimental studies should be performed using high energy neutron beams.

Chapter 7

Conclusion

The purpose of this study is to develop a high-flux capability neutron detection system for harsh radiation (gamma/neutron mixed and quite high fluxes) environments by avoiding pulse shape analysis. A series of experimental and simulation tests were performed using CVD diamond detectors.

The n/ γ separation was improved for a thermal-neutron detector that consisted of an ${}^6\text{LiF}$ neutron converter and a CVD diamond detector by decreasing the gamma-pulse height through a reduction in the thickness of the diamond crystal. The thickness was determined with consideration of the charged-particle range in the diamond. The effect of the thickness on the energy-deposition spectrum was evaluated via simulations involving monoenergetic neutrons and γ -rays. The thickness of 25 μm was selected according to the energy-deposition spectrum, γ -ray sensitivity, and energy gives 99.99% events.

To experimentally demonstrate the effectiveness of reducing the detector thickness, 25- and 140- μm -thick diamond detectors were prepared. The 25- μm -thick diamond detectors exhibited CCEs of $>90.0\%$ and low leakage currents (<20 pA at room temperature) under applied electric fields of 15 kV/cm, however, the leakage currents were >140 μm under electric fields of <7 kV/cm.

The detectors combined with a signal readout system comprising a conventional charge-sensitive preamplifier and a linear amplifier (analogue system) were tested for alpha particles, γ -rays, and thermal and fast neutrons. For alpha particles of 5.486 MeV, energy resolutions of $\sim 1.0\%$ were achieved. For γ -rays, the detectors were tested at dose rates ranging from 0.693 to 107 Gy/h. Although, the 25- μm -thick diamond detector exhibited significant pile-up effects, the neutron/gamma discrimination capability was maintained with the pulse-height distributions. However, for the 140- μm -thick detector, the energy deposition exceeded the 2.73-MeV equivalent pulse height that

was the separation energy of neutron events due to pile-up at 6.36 Gy/h. For thermal neutrons, the energy-deposition spectra were obtained using an ^{241}Am -Be neutron source and a graphite pile. The spectra exhibited triton peaks well separated from low-energy events. By using the peak counts, the thermal-neutron detection efficiency was estimated as $1.04 \times 10^{-3} \pm 9 \times 10^{-5}$. By performing fast-neutron tests, triton peak count rates were obtained for 144-keV, 565-keV, 1.2-MeV, 5-MeV, and 14.8-MeV neutrons with an acrylic slab phantom for the 25- μm -thick detector. The results indicated that the reduction of the diamond-detector thickness to 25 μm was effective for thermal- and fast-neutron detection with γ -ray rejection.

Concerning the readout system, a fast current amplifier and waveform digitizer (the TCT-Acqiris digital system) was used for the diamond detector. The combination of the detector and this system was tested for alpha particles, γ -rays, and thermal neutrons in comparison with an analogue system. For γ -rays, the system did not exhibit pile-up with dose rates up to 107 Gy/h. For thermal neutrons, the system exhibited the same detection efficiency as the analog system.

To evaluate the system in a mixed radiation field in an electron accelerator target area, tests were performed at the Kyoto University. The thermal-neutron flux was $1.86 \times 10^5 \pm 0.16 \times 10^5 \text{ cm}^{-2}\text{s}^{-1}$ at a 30-MeV beam energy, with an average current of 3.5 μA on a tungsten target and a water moderator.

For fast-neutron measurement, the system was used with a BSS with five moderators. The response function of the BSS was successfully calculated using the PHITS Monte Carlo code. The combination of the detector and BSS was tested for ^{241}Am -Be and ^{252}Cf neutron sources. Using the SAND II unfolding code and the response function, the energy spectra of the neutron sources were successfully represented. Then, the BSS was used for the measurement of the neutron energy spectrum behind the 369.27 MeV-1 μA electron beam dump in the tunnel of the STF at KEK. The unfolded neutron spectrum was in good agreement with one obtained from simulation for below hundreds of keV. On the other hand, in the high energy region, the unfolded and simulated spectra disagreed. In order to evaluate the response function of the BSS system, further experimental studies should be performed using high energy neutron beams. The developed BSS system is a neutron energy spectrometer which can be used in harsh radiation environment. It is an ideal device for real-time monitoring beam losses in high-energy and high-power accelerator facilities.

Taken together, the 25- μm -thick detector showed good properties, i.e., low noise level, less sensitive to γ -rays, keep stable in harsh radiation environments, in this study. Combining with TCT-Acqiris digital system, 25- μm -

thick detector offered a high flux detection capability of gamma and neutron events. Using the BBS, fast neutron spectra could be represented. In future applications, a 25- μm -thick detector could be used for neutron detection in a harsh radiation (gamma/neutron mixed and quite high fluxes) environment.

Funding

This study was performed in the framework of the FY2018 Center of World Intelligence Project for Nuclear Science/Technology and Human Resource Development and was partially funded by the CLADS, JAEA.

Appendix A

Input files of the simulation on diamond detector using PHITS

A.1 Flux simulation in STF tunnel

```
[ Title ] \\
STF \\

[ Parameters ] \\
icntl      = 0 \\
maxcas     = 1000 \\
maxbch     = 3600*31 \\
emin(1)    = 1e-9 \\
emin(2)    = 1e-10 \\
emin(12)   = 1e-9 \\
emin(13)   = 1e-9 \\
emin(14)   = 1e-9 \\
dmax(2)    = 20 \\
dmax(12)   = 1000 \\
dmax(13)   = 1000 \\
dmax(14)   = 1000 \\
negs       = 1 \\
ipnint     = 1 \\
pnimul     = 1000 \\
ejamnu     = 3000.0 \\
nlost      = 9999 \\
inclg      = 2 \\
itall      = 1 \\
file(1)    = /home/iwase/phits \\
file(6)    = phits.out \\

set: c1[0.014] $thickness of diamond[cm] \\
set: c2[1.e-5] $thickness of Ti[cm] \\
set: c3[0.10] $thickness of PCB[cm] \\
set: c4[1.9e-4] $thickness of LiF[cm] \\
set: c5[0.1] $thickness of peek[cm] \\
set: c6[0.15] \\
set: c37[0.662] $photon energy[MeV] \\
set: c10[9.5] \\

[ Source ] \\
s-type = 1 \\

proj = electron \\
dir = 1.0 \\
r0 = 0.5 \\
y0 = 0 \\
z0 = -55.001 \\
z1 = -55.001 \\
e0 = 369.27 \\

[ Material ] \\
$ Air D = 1.20e-3 g/cm3 \\
mat[101]  1H   -6.40e-04 \\
          12C  -1.40e-04 \\
          14N  -7.51e-01 \\
          16O  -2.36e-01 \\
          40Ar -1.28e-02 \\

$ Concrete D = 2.2 g/cm3 \\
mat[102]  1H   1.3407e-2 \\
          12C  1.1030e-3 \\
          16O  4.3887e-2 \\
          27Al 1.7971e-3 \\
          28Si 1.6123e-2 \\
          40Ca 1.8940e-3 \\
          56Fe 3.3448e-4 \\

$ Copper Cu (8.96 g/cm3) \\
mat[103]  63Cu 6.917E+01 \\
          65Cu 3.083E+01 \\

$ Iron D = 7.1 g/cm3 \\
mat[104]  54Fe 0.05845 \\
          56Fe 0.91754 \\
          57Fe 0.02119 \\
          58Fe 0.00282 \\

$ marble D = -2.71 g/cm3 \\
```

```

mat[105] 40Ca 1 \\
         12C 1 \\
         16O 3 \\
$ soil D = 1.5 g/cm3
mat[106] 1H -0.021 \\
         12C -0.016 \\
         16O -0.577 \\
         27Al -0.05 \\
         28Si -0.271 \\
         K -0.013 \\
         40Ca -0.041 \\
         56Fe -0.011 \\
$ aluminum D = 2.7 g/cm \\
mat[107] 27Al 1.0 \\
$ water D = 1 g/cm \\
mat[108] H 2.0 \\
         O 1.0 \\
$ lead D = 11.34 g/cm \\
mat[109] Pb 1.0 \\
$ PE D = 0.96 g/cm \\
mat[110] C 1 \\
         H 2 \\
[ S u r f a c e ] \\
999 rpp -200 200 -200 \\
300 -600 300 \\
$target \\
2000 rcc 0 0 -55 0 \\
0 85 4 \\
$target_outer \\
2001 rcc 0 0 -60 0 \\
0 115 16 \\
$target_water1 \\
2002 rcc 0 0 -50 0 \\
0 -5 6.5 \\
$target_water2 \\
2003 rcc 0 0 -50 0 \\
0 80 4.5 \\
$target_water3 \\
2004 rcc 0 0 25 0 \\
0 5 6.5 \\
$target_water4 \\
2005 rcc 0 10 -60 0 \\
0 90 2.5 \\
$Dump_space1 \\
2015 rpp -17 17 -17 17 \\
-61 56 \\
$Dump_space2 \\
2016 rpp -25 25 -21.5 28.5 \\
-70 60 \\
$Dump_space3 \\
2017 rpp -5 5 -17.5 22.5 \\
-220 -70 \\
$Iron1 \\
2021 rpp -85 85 -117.5 -21.5 \\
-120 100 \\
$Iron2 \\
2022 rpp -85 85 -21.5 90.5 \\
-120 100 \\
$Iron3 \\
2023 rpp -50 50 -17.5 62.5 \\
-220 -120 \\
$Iron4 \\
2024 rpp -50 50 -17.5 32.5 \\
100 150 \\
2025 rpp -50 50 -117.5 -17.5 \\
-220 -120 \\
$FeSheet \\
2031 rpp -152.4 152.4 -120 -117.5 \\
-245 212.2 \\
$conc \\
2041 rpp -50 50 -117.5 -17.5 \\
100 150 \\
$Xu-experiment region \\
2052 sph 0 0 150+c10 c10 \\
[ C e 11 ] \\
$$target Al and water \\
2000 107 -2.7 -2000 \\
2001 107 -2.7 -2001 2000 \\
2005 #2002 #2003 #2004 \\
2002 108 -1 -2002 2000 \\
2003 108 -1 -2003 2000 \\
2004 108 -1 -2004 2003 \\
2005 108 -1 -2005 \\
$$target air \\
$2015 101 -1.20e-3 -2015 2001 \\
2016 101 -1.20e-3 -2016 2001 \\
2017 101 -1.20e-3 -2017 \\
$$$$DUMP-2 Fe \\
2021 104 -7.1 -2021 \\
2022 104 -7.1 -2022 2016 2017 \\
2023 104 -7.1 -2023 2017 \\
2024 104 -7.1 -2024 \\
2025 104 -7.1 -2025 \\
2041 102 -2.1 -2041 \\
$Xu-san experiment region \\
2052 101 -1.20e-3 -2052 \\
$ L-xing tunnel \\
10001 101 -1.20e-3 -999 2021 \\
2022 2023 2024 2025 2041 \\
2052 \\
10003 -1 999 \\
[Importance] \\
part = neutron photon

```

```

reg      imp  \\  

2000    3**0 \\  

2001    3**1 \\  

2002    3**1 \\  

2003    3**1 \\  

2004    3**1 \\  

2005    3**1 \\  

2016    3**2 \\  

2017    3**3 \\  

2021    3**3 \\  

2022    3**3 \\  

2023    3**3 \\  

2024    3**3 \\  

2025    3**3 \\  

2041    3**4 \\  

2052    3**5 \\  

10001   3**5 \\  

[V o l u m e] \\  

reg      vol  \\  

2052    20*20*20 \\  

[T - C r o s s] \\  

title = Energy distribution in region mesh \\  

mesh = reg \\  

reg = 1 \\  

non      r-in      r-out      area \\  

1        (2041 10001) 2052      20*20*6 \\  

e-type = 3 \\  

emin = 1.0E-10 \\  

emax = 1000 \\  

ne = 100 \\  

unit = 1 \\  

axis = eng \\  

file = cross-neutron.out \\  

output = flux \\  

part = all neutron proton triton alpha electron \\  

epsout = 1 \\  

[T - T r a c k] \\  

mesh = reg \\  

reg = 2052 \\  

part = all neutron proton triton alpha electron \\  

e-type = 3 \\  

ne = 1000 \\  

emax = 1000.0 \\  

emin = 1.0E-10 \\  

unit = 1 \\  

axis = eng file = track_eng.out \\  

title = Track Detection using [T-track] tally \\  

gshow = 3 \\  

epsout = 1 \\  

[ T - T r a c k ] \\  

mesh = xyz \\  

x-type = 1 \\  

nx = 1 \\  

-50.0 50.0 \\  

y-type = 2 \\  

ny = 500 \\  

ymin = -100 \\  

ymax = 100 \\  

z-type = 2 \\  

nz = 1000 \\  

zmin = -400 \\  

zmax = 300 \\  

part = electron neutron photon proton \\  

e-type = 1 \\  

ne = 1 \\  

0.0 9260+50 \\  

unit = 1 \\  

axis = yz \\  

file = track_yz.out \\  

title = Track Detection using [T-track] tally \\  

gshow = 1 \\  

epsout = 1 \\  

[ E n d ] \\  

[T - T r a c k] \\  


```

A.2 Energy deposition using KEK graphite pile

```

[title]
KEK Bonner Response for KEK Graphyte pile

4.14e-7 1.44e-2 \\
1.10e-1 3.34e-2 \\
3.30e-1 3.13e-2 \\
5.40e-1 2.81e-2 \\
7.50e-1 2.50e-2 \\
9.70e-1 2.14e-2 \\
1.18e0 1.98e-2 \\
1.40e0 1.75e-2 \\
1.61e0 1.92e-2 \\
1.82e0 2.23e-2 \\
2.04e0 2.15e-2 \\
2.25e0 2.25e-2 \\
2.47e0 2.28e-2 \\
2.68e0 2.95e-2 \\
2.90e0 3.56e-2 \\
3.11e0 3.69e-2 \\
3.32e0 3.46e-2 \\
3.54e0 3.07e-2 \\
3.75e0 3.00e-2 \\
3.97e0 2.69e-2 \\
4.18e0 2.86e-2 \\
4.39e0 3.18e-2 \\
4.61e0 3.07e-2 \\
4.82e0 3.33e-2 \\
5.04e0 3.04e-2 \\
5.25e0 2.74e-2 \\
5.47e0 2.33e-2 \\
5.68e0 2.06e-2 \\
5.89e0 1.82e-2 \\
6.11e0 1.77e-2 \\
6.32e0 2.04e-2 \\
6.54e0 1.83e-2 \\
6.75e0 1.63e-2 \\
6.96e0 1.68e-2 \\
7.18e0 1.68e-2 \\
7.39e0 1.88e-2 \\
7.61e0 1.84e-2 \\
7.82e0 1.69e-2 \\
8.03e0 1.44e-2 \\
8.25e0 9.68e-3 \\
8.46e0 6.52e-3 \\
8.68e0 4.26e-3 \\
8.89e0 3.67e-3 \\
9.11e0 3.81e-3 \\
9.32e0 5.06e-3 \\
9.53e0 6.25e-3 \\
9.75e0 5.52e-3 \\
9.96e0 4.68e-3 \\
1.02e1 3.70e-3 \\
1.04e1 2.78e-3 \\
1.06e1 1.51e-3 \\
1.08e1 3.63e-4 \\
1.10e1 \\

[ P a r a m e t e r s ]
icntl = 0 \\
maxcas = 50000 \\
maxbch = 400 \\
emin(2) = 1.0E-10 \\
dmax(2) = 20.0 \\
emin(12) = 0.01 \\
emin(13) = 0.01 \\
emin(14) = 0.01 \\
emin(15) = 0.01 \\
emin(16) = 0.01 \\
emin(17) = 0.01 \\
emin(18) = 0.01 \\
emin(19) = 0.01 \\
nlost = 10000 \\
neps = 1 \\
e-mode = 2 \\
ireschk = 1 \\
itall = 1 \\
file(1) = /home/ce/hiwase/phits \\
file(6) = phits.out \\

set: c1[250] #x \\
set: c2[190] #y \\
set: c3[190] #z \\
set: c11[0.1] $thickness of PEEK[cm] \\
set: c12[1.9e-4] $thickness of LiF[cm] \\
set: c13[0.1] $thickness of PCB[cm] \\
set: c14[1.e-5] $thickness of Ti[cm] \\
set: c15[0.0025] $thickness of diamond[cm] \\
set: c16[0.15] $thickness of pcb hole[cm] \\

[source] \\
s-type = 4 \\
proj = neutron \\
dir = all \\
r0 = 0 \\
z0 = 0 \\
z1 = 0 \\
e-type = 1 \\
ne = 52 \\

[material] \\
mat[1] C 1.0 !Graphite \\
mt1 grph.20t \\

```

mat[3]	24052	-0.195 \\		mat[11]	Cu	-0.1022 \\
	26056	-0.705 \\			Ni	-0.0119 \\
	28058	-0.1 \\			Au	-0.0006 \\
		!SUS \\			C	-0.6866 \\
mat[5]	1H	1.47 \\			H	-0.0542 \\
	12C	0.836 \\			O	-0.1445 \\
	16O	4.13 \\		mat[12]	6Li	0.475 \\
	23Na	0.0194 \\			7Li	0.025 \\
	24Mg	0.0297 \\			F	0.500 \\
	27Al	0.0725 \\		mat[13]	N	-0.755 \\
	28Si	0.419 \\			O	-0.232 \\
	40Ca	0.987 \\			Ar	-0.013 \\
	56Fe	0.0192 \\		mat[14]	Ti	1.0 \\
				mat[15]	C	1.0 \\

```
[surface]
1 rpp -c3/2 c3/2 -c2/2
      c2/2 -c1/2 c1/2 \\
5 rpp -500 500 -c2/2-22.5-50
      -c2/2-22.5 -500 500 \\
4 rpp -c3/2+5 c3/2-5 -c2/2-22.5
      -c2/2-2.5 -c1/2+5 c1/2-5
      $ Fe-base-inside-air \\
6 rpp -c3/2-5 c3/2+5 -c2/2-22.5
      -c2/2 -c1/2-5 c1/2+5
      $ Fe-base\\
7 rpp -c3/2-145-1.5 c3/2+260+1.5 -c2/2-22.5-1
      300+1.5 -c1/2-170-1.5 c1/2+370+1.5
\\
8 rpp -c3/2-145 c3/2+260 -c2/2-22.5-1
      300 -c1/2-170 c1/2+370
      $ Wall-inside \\
9 sph 0 0 0
      2000 \\
51 rpp -47-10 -47+10 -190/2-22.5
      -190/2-2.5 84-10 84+10 \\
52 rpp -10 +10 -190/2-22.5
      -190/2-2.5 84-10 84+10 \\
53 rpp 47-10 47+10 -190/2-22.5
      -190/2-2.5 84-10 84+10 \\
54 rpp -47-10 -47+10 -190/2-22.5
      -190/2-2.5 42-10 42+10 \\
55 rpp -10 +10 -190/2-22.5
      -190/2-2.5 42-10 42+10 \\
56 rpp 47-10 47+10 -190/2-22.5
      -190/2-2.5 42-10 42+10 \\
57 rpp -47-10 -47+10 -190/2-22.5
      -190/2-2.5 -10 10 \\
58 rpp -10 +10 -190/2-22.5
      -190/2-2.5 -10 10 \\
59 rpp 47-10 47+10 -190/2-22.5
      -190/2-2.5 -10 10 \\
60 rpp -47-10 -47+10 -190/2-22.5
      -190/2-2.5 -42-10 -42+10 \\
61 rpp -10 +10 -190/2-22.5
      -190/2-2.5 -42-10 -42+10 \\
62 rpp 47-10 47+10 -190/2-22.5
      -190/2-2.5 -42-10 -42+10 \\
63 rpp -47-10 -47+10 -190/2-22.5
      -190/2-2.5 -84-10 -84+10 \\
```

```

64 rpp -10 +10 -190/2-22.5
-190/2-2.5 -84-10 -84+10 \\
65 rpp 47-10 47+10 -190/2-22.5
-190/2-2.5 -84-10 -84+10 \\
11 rpp -0.475 0.475 -5
-5+0.525 c1/2-78 c1/2-78+3.96
$ PEEK \\
12 rpp -0.25 0.25 -5+0.525-c11-c12
-5+0.525-c11 c1/2-78+0.91-0.25 c1/2-78+0.91+0.25 \\
14 rpp -0.2 0.2 -5+0.525-c11-c12-c13-c14
-5+0.525-c11-c12-c13 c1/2-78+0.91-0.2 c1/2-78+0.91+0.2 \\
15 rpp -0.225 0.225 -5+0.525-c11-c12-c13-c14-c15
-5+0.525-c11-c12-c13-c14 c1/2-78+0.91-0.225 c1/2-78+0.91+0.225
$ diamond \\
16 rpp -0.20 0.20 -5+0.525-c11-c12-c13-c14-c15-c14
-5+0.525-c11-c12-c13-c14-c15 c1/2-78+0.91-0.2 c1/2-78+0.91+0.2
$ Ti \\
$ PCB hole \\
13 rcc 0 -5+0.525-c11-c12-c13 c1/2-78+0.91 0 c13 0 0.125 \\
17 rcc 0 -5+0.525-c11-c12-c13-c14-c15-c16 c1/2-78+0.91 0 c16 0 0.05 \\
$air hole \\
20 rpp -5 5 -5 5 c1/2-78 c1/2 $ hole air \\

```

```

[cell]
1 1 -1.75 -1 20 $ Pile \\
4 13 -1.2e-3 -9 1 5 $ PEEK \\
#7 6 $ Room (Air) \\
5 5 -2.2 -5 $ Floor \\
6 3 -7.8 -6 4 $ Fe-base \\
7 5 -1.5 -7 8 5 \\
$ Wall \\
8 13 -1.2e-3 -4 51 \\
52 53 54 55 56 57 [volume]
58 59 60 61 62 63 reg vol \\
64 65 $ Fe-base-inside(Air) \\ 15 0.45*0.45*c11 \\
9 -1 9 [ T - Deposit ] $ Diamond \\
20 13 -1.2e-3 -20 11 \\ title = Energy deposition in xyz mesh \\
51 5 -2.2 -51 \\ mesh = reg \\
52 5 -2.2 -52 \\ reg = 15 \\
53 5 -2.2 -53 \\ unit = 3 \\
54 5 -2.2 -54 \\ material = all \\
55 5 -2.2 -55 \\ output = deposit \\
56 5 -2.2 -56 \\ e-type = 2 \\
57 5 -2.2 -57 \\ ne = 100 \\
58 5 -2.2 -58 \\ emin = 0 \\
59 5 -2.2 -59 \\ emax = 4.0 \\
60 5 -2.2 -60 \\ axis = eng \\
61 5 -2.2 -61 \\ file = deposit.out \\
62 5 -2.2 -62 \\ part = all electron photon alpha triton \\
63 5 -2.2 -63 \\ gshow = 1 \\
64 5 -2.2 -64 \\ epsout = 1 \\
65 5 -2.2 -65 \\

```

[End]

A.3 Response functions of Bonner sphere

```

[ T i t l e ]
calculation

[ P a r a m e t e r s ]
icntl      = 0 \\
maxcas     = 3000000 \\
maxbch     = 300 \\
itall      = 1 \\
e-mode     = 2 \\
file(1)    = /gdfs/home/ce/hiwase/phits \\
file(6)    = phits.out \\

set: c1[0.0025] $thickness of diamond[cm] \\
set: c2[1.e-5] $thickness of Ti[cm] \\
set: c3[0.1] $thickness of PCB[cm] \\
set: c4[1.9e-4] $thickness of LiF[cm] \\
set: c5[0.1] $thickness of PEEK[cm] \\
set: c6[0.15] $thickness of pcb hole[cm] \\
set: c10[5.5] \\

[ S o u r c e ]
s-type     = 1          # mono-energetic source \\
proj       = neutron   # kind of incident nucleus \\
e0         = eee       # energy of beam [MeV] \\
r0         = c10        \\
z0         = -5-c10     \\
z1         = -5-c10     \\
dir        = 1.0       \\

[ M a t e r i a l ]
mat[1]     C 1.0
$ 3.5g/cm3 diamond \\
mat[2]     Ti 1.0
$ 4.506g/cm3 Ti \\
mat[3]     N -0.755
$ 0.0013g/cm3 air PCB hole \\
           O -0.232 \\
           Ar -0.013 \\
mat[4]     Si 1.0
$ 1.8g/cm3 PCB \\
           O 2.0 \\
mat[5]     6Li 0.475 \\
$2.64g/cm3 LiF neutron converter \\
           7Li 0.025 \\
           F 0.500 \\
mat[9]     Cu -0.1022 \\
           Ni -0.0119 \\
           Au -0.0006 \\
           C -0.6866 \\
           H -0.0542 \\
           O -0.1445 \\
mat[10]    C 1 \\
           H 2 \\

[ S u r f a c e ]
11  rpp -0.91 3.05 -0.5 0.5 -0.285 0.285 $ peek \\
21  rpp 3.05 3.53 -0.5 0.5 -0.435 0.285 $ peek \\
22  rpp 3.53 3.7 -0.5 0.5 -0.435 0.355 $ peek \\
41  rcc 3.7 0 0.00 0.3 0.00 0.00 0.3 $ luosi \\
42  rcc 4 0 0.00 0.5 0.00 0.00 0.5 $ luosi \\

$$ diamond sensor \\
$ neutron converter \\
12  rpp -0.25 0.25 -0.25 0.25 -c2-c3-c4-c1/2 -c2-c3-c1/2 \\
$ Ti \\
14  rpp -0.20 0.20 -0.20 0.20 -c2-c1/2 c1/2 \\
$ diamond \\
15  rpp -0.225 0.225 -0.225 0.225 -c1/2 c1/2 \\
$ Ti \\
16  rpp -0.20 0.20 -0.20 0.20 c1/2 c1/2+c2 \\
$ PCB hole \\
13  rcc 0.00 0.00 -c2-c3-c1/2 0.00 0.00 c3 0.125 $ for lif \\
17  rcc 0.00 0.00 c1/2+c2 0.00 0.00 c6 0.05 $ for a \\
$$ bonner ball \\
100 rcc -0.91 0 0 4.61 0 0 1 \\
101 rcc 3.7 0 0 1.8 0 0 1 \\
110 sph 0 0 0 c10 \\
201 rcc 3.7 0 0 1.8 0 0 0.5 \\
$$ flux test \\
6  rcc 0 0 -c10-0.1 0 0 0.09999 c10 \\
999 sph 0 0 0 200 \\

```

```

[ C e l l ] \\  

$ peek \\  

  11  9  -1.46  -11  12  

  13  14  15  16  17 $ peek \\  

  21  9  -1.46  -21  $ peek \\  

  22  9  -1.46  -22  $ peek \\  

  41  9  -1.46  -41  $ peek \\  

  42  9  -1.46  -42  $ peek \\  

$ diamond \\  

  12  5  -2.64  -12  $ neutron converter \\  

  14  2  -4.5  -14  $ Ti \\  

  15  1  -3.5  -15  $ diamond \\  

  16  2  -4.5  -16  $ Ti \\  

$ pcb hole \\  

  13  3  -0.0012  -13  $ PCB hole \\  

  17  3  -0.0012  -17  $ PCB hole \\  

$$ bonner ball \\  

  100  10  -0.96  -100  11  21  

  22 \\  

  101  10  -0.96  -101  -110  201 \\  

  110  10  -0.96  -110  100  201 \\  

  201  3  -0.0012  -201  -110  41  

  42 \\  

$$ flux test \\  

  6  0  -6 \\  

  666  0  -999  110  6 \\  

  999  -1  999 \\  

[Volume] \\  

  reg  vol \\  

  15  0.45*0.45*c1 \\  

[ T-Deposit ] \\  

title = Energy Deposition for each cell \\  

mesh = reg \\  

reg = 15 \\  

unit = 3 \\  

dedxfnc = 0 \\  

material = all \\  

output = deposit \\  

e-type = 2 \\  

emin = 0 \\  

emax = 3 \\  

ne = 100 \\  

axis = eng \\  

file = deposit.out \\  

part = all triton alpha neutron C proton \\  

epsout = 1 \\  

[END]

```

A.4 Response of thermal neutron with different thicknesses

```

[ T i t l e ]                               set: c6[0.15] $thickness of pcb hole[cm] \\
calculation

[ P a r a m e t e r s ]
icntl      = 0 \\
maxcas     = 3000000 \\
maxbch     = 120 \\
negs       = 1 \\
itall      = 1 \\
e-mode     = 2 \\
file(1)    = /gpfs/home/ce/hiwase/phits \\
file(6)    = phits.out \\
emin(1)    = 1.000000000E-03 \\
emin(2)    = 1.000000000E-10 \\
emin(12)   = 1.000000000E-09 \\
emin(13)   = 1.000000000E-03 \\
emin(14)   = 1.000000000E-09 \\
emin(15)   = 1.000000000E-03 \\
emin(16)   = 1.000000000E-03 \\
emin(17)   = 1.000000000E-03 \\
emin(18)   = 1.000000000E-03 \\
emin(19)   = 1.000000000E-03 \\
dmax(2)    = 20.0000000 \\
dmax(12)   = 1000.00000 \\
dmax(13)   = 1000.00000 \\
dmax(14)   = 1000.00000 \\
esmin      = 1.000000000E-6 \\

set: c1[0.001] $thickness of diamond[cm] \\
set: c2[1.e-5] $thickness of Ti[cm] \\
set: c3[0.1] $thickness of PCB[cm] \\
set: c4[1.9e-4] $thickness of LiF[cm] \\
set: c5[0.1] $thickness of PEEK[cm] \\

[ S o u r c e ] \\
s-type     = 2 \\
proj       = neutron \\
x0         = -0.01 \\
x1         = 0.01 \\
y0         = -0.01 \\
y1         = 0.01 \\
z0         = -1 \\
z1         = -1 \\
dir        = 1.0 \\
e0         = 2.5E-8 \\

[ M a t e r i a l ]
mat[1]     C      1.0 \\
mat[2]     Ti     1.0 \\
mat[3]     N      -0.755 \\
           O      -0.232 \\
           Ar     -0.013 \\
mat[4]     Si     1.0 \\
           O      2.0 \\
mat[5]     6Li    0.475 \\
           7Li    0.025 \\
           F      0.500 \\
mat[9]     Cu     -0.1022 \\
           Ni     -0.0119 \\
           Au     -0.0006 \\
           C      -0.6866 \\
           H      -0.0542 \\
           O      -0.1445 \\
mat[10]    C      1 \\
           H      2 \\

[ S u r f a c e ] \\
$peek \\
11 rpp -0.91 3.05 -0.5 0.5 -0.285 0.285 \\
$ neutron converter \\
12 rpp -0.25 0.25 -0.25 0.25 -c2-c3-c4-c1/2 -c2-c3-c1/2 \\
$ Ti \\
14 rpp -0.20 0.20 -0.20 0.20 -c2-c1/2 -c1/2 \\
$ diamond \\
15 rpp -0.225 0.225 -0.225 0.225 -c1/2 c1/2 \\
$ Ti \\
16 rpp -0.20 0.20 -0.20 0.20 c1/2 c1/2+c2 \\
$ PCB hole \\
13 rcc 0.00 0.00 -c2-c3-c1/2 0.00 0.00 c3 0.125 $ for lif \\
17 rcc 0.00 0.00 c1/2+c2 0.00 0.00 c6 0.05 $ for a \\
999 sph 0 0 0 20 \\

[ C e l l ] \\
$ peek
11 9 -1.46 -11 12 13 14 15
16 17 \\
$ diamod \\
12 5 -2.64 -12 $ neutron converter
14 2 -4.5 -14 $ Ti
15 1 -3.5 -15 $ diamond
16 2 -4.5 -16 $ Ti
$ pcb hole

```

```
13 3 -0.0012 -13 $ PCB hole \\  
17 3 -0.0012 -17 $ PCB hole \\  
666 0 -999 11 \\  
999 -1 999 \\  

```

```
[Volume] \\  
reg vol \\  
15 0.45*0.45*c1 \\  

```

```
[T-Deposit] \\  

```

```
title = c1 \\  
mesh = reg \\  
reg = 15 \\  
unit = 3 \\  
dedxfnc = 0 \\  
material = all \\  
output = deposit \\  
e-type = 2 \\  
emin = 0 \\  
emax = 3 \\  
ne = 100 \\  
axis = eng \\  
file = deposit.out \\  
part = all triton alpha electron \\  
epsout = 1 \\  

```

```
[END] \\  

```

Appendix B

Input file of the SANDII

42

(6f12.5) BOUND ENERGY

5.00000E+08	4.08000E+08	2.08000E+08	7.50000E+07	4.08000E+07	2.58000E+07
1.50000E+07	7.50000E+06	4.08000E+06	2.08000E+06	7.50000E+05	4.08000E+03
2.08000E+05	7.50000E+04	4.08000E+04	2.08000E+04	7.50000E+03	4.08000E+03
2.08000E+03	7.50000E+02	4.08000E+02	2.08000E+02	7.50000E+01	4.08000E+01
2.08000E+01	7.50000E+00	4.08000E+00	2.08000E+00	7.50000E-01	4.08000E-01
2.83000E-01	1.75000E-01	7.50000E-02	4.08000E-02	2.83000E-02	1.75000E-02
7.50000E-03	4.08000E-03	2.08000E-03	7.50000E-04	4.08000E-04	2.08000E-04
1.00000E-04					

5

(6f12.5)

1 DIAM SPHERE B.B RESPONSE FUNCTION 19.0CM

2.19168E-05	1.71641E-05	1.42898E-05	1.54665E-05	2.01766E-05	3.25176E-05
4.24374E-05	6.31202E-05	7.31433E-05	8.59131E-05	7.56596E-05	6.72286E-05
5.07868E-05	4.56336E-05	4.43013E-05	3.97683E-05	3.92369E-05	3.85103E-05
3.65295E-05	3.63699E-05	3.51326E-05	3.34135E-05	3.32261E-05	3.17524E-05
2.97243E-05	2.87535E-05	2.84589E-05	2.52485E-05	2.42313E-05	2.27955E-05
2.16087E-05	1.94108E-05	1.68344E-05	1.51085E-05	1.49205E-05	1.19082E-05
1.08627E-05	9.71085E-06	8.23650E-06	7.68362E-06	7.16618E-06	6.90392E-06

2 DIAM SPHERE B.B RESPONSE FUNCTION 11.0CM

1.77113E-05	1.38290E-05	1.08901E-05	9.86231E-06	1.08900E-05	1.66519E-05
1.72537E-05	2.03900E-05	2.69577E-05	5.17614E-05	6.25533E-05	6.62134E-05
6.72619E-05	6.77862E-05	6.70756E-05	6.76249E-05	6.83744E-05	6.86738E-05
6.96485E-05	6.99054E-05	6.95433E-05	7.05320E-05	6.98604E-05	6.90720E-05
6.72939E-05	6.53473E-05	6.40700E-05	5.93428E-05	5.60660E-05	5.24652E-05
5.12298E-05	4.44473E-05	3.94916E-05	3.55984E-05	3.42506E-05	2.86052E-05
2.43105E-05	2.20510E-05	1.88450E-05	1.68912E-05	1.67893E-05	1.50750E-05

3 DIAM SPHERE B.B RESPONSE FUNCTION 7.0CM

1.57998E-05	1.18898E-05	9.75966E-06	8.51277E-06	8.83219E-06	1.32156E-05
1.14453E-05	5.37628E-06	5.22619E-06	1.36581E-05	2.03641E-05	2.48610E-05
3.32852E-05	3.62832E-05	3.86172E-05	4.35625E-05	4.67683E-05	4.88464E-05
5.44151E-05	5.79211E-05	5.92141E-05	6.48714E-05	6.82830E-05	7.05324E-05
7.45714E-05	7.62666E-05	7.68015E-05	7.55989E-05	7.35438E-05	7.05555E-05
6.85235E-05	6.14924E-05	5.42785E-05	4.91966E-05	4.65566E-05	3.80284E-05
3.30582E-05	2.99967E-05	2.53786E-05	2.33408E-05	2.23402E-05	2.03583E-05

4 DIAM SPHERE B.B RESPONSE FUNCTION 4.0CM-point

1.44146E-05	1.10605E-05	9.14725E-06	8.29801E-06	8.34406E-06	1.30585E-05
1.09338E-05	2.29126E-06	3.94794E-07	1.07965E-06	2.07869E-06	2.79706E-06
5.25905E-06	6.72715E-06	7.82782E-06	1.05881E-05	1.26188E-05	1.39612E-05
1.79519E-05	2.10455E-05	2.34561E-05	2.97843E-05	3.44444E-05	3.76875E-05
4.64411E-05	5.23272E-05	5.57329E-05	6.54309E-05	6.92580E-05	7.13071E-05
7.11746E-05	7.03763E-05	6.57683E-05	6.08104E-05	5.84586E-05	4.68116E-05
4.01494E-05	3.60286E-05	3.00095E-05	2.72219E-05	2.60793E-05	2.34321E-05

5 DIAM SPHERE B.B RESPONSE FUNCTION BARE

1.33239E-05	1.03093E-05	8.07733E-06	8.09534E-06	8.88958E-06	1.46443E-05
1.32015E-05	2.28400E-06	1.02076E-07	3.54288E-08	4.03656E-08	7.14384E-08
9.96072E-08	1.36052E-07	1.72933E-07	3.17262E-07	4.41844E-07	5.51324E-07
9.81407E-07	1.38695E-06	1.74254E-06	2.96817E-06	4.11033E-06	5.10015E-06
8.65552E-06	1.17824E-05	1.45737E-05	2.42823E-05	3.30007E-05	4.02998E-05
4.45954E-05	6.62179E-05	8.85075E-05	1.06589E-04	1.16881E-04	1.62918E-04
2.00449E-04	2.23314E-04	2.52806E-04	2.39543E-04	2.17132E-04	1.38524E-04

0.001
200

(6f12.5) dose conversion factor from ICRP74 [pSv/(n/cm²)] by XXQ!

3.58385E+02	3.11640E+02	3.20395E+02	4.01235E+02	5.01220E+02	5.72140E+02
4.43205E+02	4.04015E+02	4.11340E+02	4.10850E+02	3.22530E+02	2.43855E+02
9.03455E+01	4.27785E+01	2.61815E+01	1.08400E+01	8.20645E+00	7.85220E+00
7.91375E+00	8.29895E+00	8.59570E+00	9.39525E+00	9.89580E+00	1.02450E+01
1.12935E+01	1.19895E+01	1.24435E+01	1.32885E+01	1.35670E+01	1.35505E+01
1.35255E+01	1.28615E+01	1.17550E+01	1.09845E+01	1.05965E+01	9.20990E+00
9.00000E+00	9.00000E+00	9.00000E+00	9.00000E+00	9.00000E+00	9.00000E+00

STF p-Li spectrum

1	4.39E+00
2	8.38E+00
3	9.70E+00
4	6.50E+00
5	3.70E+00

0 0 0.

(6f12.5) test spectlum 1 am

0.0000E+00	0.0000E+00	2.4684E-12	7.5783E-12	2.1507E-12	2.9364E-12
1.8546E-12	1.5251E-12	2.2689E-12	1.4911E-11	3.6122E-10	4.1634E-10
5.2312E-09	2.2596E-09	2.4207E-10	6.0054E-09	2.2776E-10	4.3899E-10
4.9667E-10	1.2419E-10	1.1169E-10	1.1787E-10	1.1688E-10	4.1687E-11
1.4663E-10	3.5049E-11	6.4724E-11	6.4957E-11	1.7575E-11	2.2355E-11
0.0000E+00	3.1842E-11	1.5634E-10	6.3866E-11	7.2874E-11	1.5737E-10
1.4039E-11	4.6114E-12	1.4329E-12	8.8112E-14	1.9365E-14	5.3826E-15

List of Figures

1.1	Concept of criticality prevention [1].	2
1.2	Sediments on the fuel debris [2].	2
1.3	Livingston chart of accelerators [4].	4
1.4	Operation principle of a thermal-neutron detector using a ${}^6\text{LiF}$ converter layer.	9
1.5	BSSs of different diameters [41].	10
1.6	Rectangular pulse shape of an alpha particle [35].	12
1.7	Triangular pulse shape for an electron [35].	12
2.1	Spectrum of ${}^6\text{Li}(n, \alpha){}^3\text{H}$ reaction measured using the Cx Spectroscopic Shaping Amplifier with a 500 μm diamond detector [35].	15
2.2	The simulation model of the CVD diamond detectors. (a) Overall and (b) enlarged views of the sensor part.	17
2.3	The simulated spectrum of the diamond detector with different thickness and its housing for five photon energies.	20
2.4	Total counts per source for diamond detectors with different thicknesses and different gamma-sources.	21
2.5	$E_{99.99}$ as a function of incident photon energy for diamond detector with different thicknesses.	23
2.6	Simulated spectra for diamond detectors with different thicknesses and a neutron source.	26
3.1	The photograph and structure of the CVD diamond detectors.	29
3.2	I–V curves of the 25- and 140- μm -thick diamond detectors. The straight line is the linear fitting line for the 25- μm -thick detector.	31
3.3	Measurement system for CCE.	33
3.4	CCEs of the 25- and 140- μm -thick diamond detectors with respect to the electric- field strength.	34
4.1	Layout for the moderate-activity γ -ray response experiment.	38

4.2	Photograph and plan view of the experimental setup for high-dose rate γ -ray response measurement.	39
4.3	Schematics and photograph of the experimental setup for thermal-neutron response measurement.	41
4.4	Monochromatic neutron irradiation system at FRS [57].	43
4.5	Moderator installation during neutron irradiation.	43
4.6	Measurement system for neutron irradiation.	44
4.7	The energy spectra of the mixed alpha-source for the two diamond detectors with analog system. The bias voltages of the 25- and 140- μm -thick detectors were, respectively, 20 and 80 V.	48
4.8	Measured and simulated responses of the 25- and 140- μm thick diamond detectors to ^{137}Cs γ -rays	50
4.9	Measured and simulated responses of the 25- and 140- μm -thick detectors to ^{60}Co γ -rays.	50
4.10	Measured spectra for the 25- and 140- μm -thick detectors exposed to ^{60}Co γ -rays with respect to the air absorbed dose rate.	53
4.11	The simulated and experimental spectrum for thermal neutron detection in KEK graphite pile by the 25- and 140- μm -thick diamond detectors.	55
4.12	The cross-section for different $n + ^{\text{nat}}\text{C}$ reaction channels [58].	58
4.13	The cross-section for different $n + ^6\text{Li}$ reaction channels [58].	59
4.14	Experimental spectra for 144-keV neutron irradiation (left, albedo layout; right, sandwich layout).	60
4.15	Experimental spectra for 565-keV neutron irradiation (left, albedo layout; right, sandwich layout).	60
4.16	Experimental spectra for 1.2-MeV neutron irradiation (left, albedo layout; right, sandwich layout).	61
4.17	Experimental spectra for 5-MeV neutron irradiation (left, albedo layout; right, sandwich layout).	61
4.18	Experimental spectra for 14.8-MeV neutron irradiation (left, albedo layout; right, sandwich layout).	62
4.19	Fast-neutron detection efficiencies with different energies (left, albedo layout; right, sandwich layout).	64
5.1	Typical signals of an ^{241}Am alpha source from TCT-Acquis digital system with the 25- and 140- μm -thick CVD diamond detectors under bias voltages of 20 and 80 V, respectively.	66
5.2	Flowchart of the pulse-height analysis method used in this study.	67
5.3	Pulse-height analysis method.	67

5.4	Measurement system of energy resolution using the TCT-Acqiris digital system.	68
5.5	Experimental setup in the target room.	70
5.6	Geometry of the simulation.	71
5.7	Energy spectra of the mixed alpha-source for the two diamond detectors with the TCT-Acqiris digital system. The bias voltages of the 25- and 140- μm -thick detectors were 20 and 80 V, respectively.	72
5.8	Pulse-height distributions obtained via the TCT-Acqiris digital system with the 25- and 140- μm -thick diamond detectors for ^{60}Co γ -rays with a dose rate of 107 Gy/h.	73
5.9	Largest-pulse height signals of the electrons from the TCT-Acqiris digital system with the 25- and 140- μm -thick diamond detectors.	74
5.10	Typical signal shape of the alpha particles for the analog system with the 25- μm -thick diamond detector.	75
5.11	Measured pulse-height distributions for thermal-neutron detection in the KEK graphite pile with the 25- μm detector.	76
5.12	Pulse-height distribution of TCT-Acqiris digital system with the 25- μm -thick CVD diamond detector for a mixed source based on the electron linear accelerator.	78
5.13	Pulse-height distribution of TCT-Acqiris digital system with the 140- μm -thick diamond detector for a mixed source based on the electron linear accelerator.	79
5.14	Typical noise shape.	80
5.15	Pulse-area distribution of TCT-Acqiris digital system with the 140- μm -thick diamond detector for a mixed source based on the electron linear accelerator.	81
5.16	Count rate as a function of average current under different beam conditions.	83
6.1	Spheres used in this study: 40, 70, 110, and 190 mm (in diameter).	85
6.2	Simulated geometric setup.	86
6.3	Neutron response of the BSS system with respect to the neutron energy.	87
6.4	Experimental setup in the graphite pile.	88
6.5	Experimental setup with the fast-neutron source at AIST.	89
6.6	Experimental setup in the STF tunnel.	90
6.7	Spectrum of thermal neutrons at the surface of the graphite pile.	92

6.8	Measured and simulated ^{241}Am -Be neutron spectra.	93
6.9	Measured and simulated ^{252}Cf neutron spectra.	93
6.10	Measured energy spectra for neutron detection using Bonner spheres in the STF tunnel with the 25- μm -thick diamond detector.	95
6.11	Flux distribution for neutrons around the dump in the STF tunnel.	95
6.12	Measured and simulated neutron spectra for the STF tunnel. .	96

List of Tables

1.1	Candidate sensors and their radiation tolerance.	5
1.2	Properties of the diamond detector and other semiconductor detectors [2].	6
1.3	Reaction channels of the $n + {}^{12}\text{C}$ reaction.	10
2.1	Material compositions and densities (diamond detector and its housing) used in the PHITS simulation.	17
4.1	Details regarding the gamma source used in the experiment.	38
4.2	Irradiation conditions of the FRS neutron calibration field.	42
4.3	Material compositions and densities used in the PHITS simulation.	46
4.4	Experimental results of count rate, maximum deposition energy, response.	51
4.5	Simulated results of count rate, maximum deposition energy, response.	52
4.6	Measured gamma-source dose rate and count rate.	54
4.7	Measured count rate and efficiency.	57
5.1	Measured thermal-neutron fluxes and efficiencies for the TCT-Acqiris digital system (25 μm).	77
5.2	Beam information and the count rate.	82
6.1	Material compositions and densities of the Bonner spheres used in the PHITS simulation.	86
6.2	Count rate for different Bonner spheres.	97

Bibliography

- [1] JAEA, https://www.jaea.go.jp/english/04/ntokai/fukushima/fukushima_01.html.
- [2] Masayuki Hagiwara, “Feasibility Study on Neutron Dosimetry under Extreme Radiation Environments Using a Diamond Detector”, the CNRS-JSPS workshop in Grenoble, July 7-12, 2019.
- [3] IAEA Review mission reports. <https://www.iaea.org/newscenter/pressreleases/iaea-issues-final-report-fourthreview-of-fukushima-decommissioning>.
- [4] Koji Takata, *Fundamental Concepts of Particle Accelerators V: Future of the High Energy Accelerators*.
- [5] S. Bacher, G. Bassi, L. Bosisio, et al., *Nucl. Instrum. Meth. A* 997 (2021) 165157.
- [6] I. Adachi, T. Browder, P. Križan, S. Tanaka, Y. Ushiroda, *Nucl. Instrum. Meth A* 907 (2018) 46–59.
- [7] CG.Pang, P. Bambade, SDi. Carlo, et al., *Nucl. Instrum. Meth. A* 931 (2019) 225-235.
- [8] K. Ueno, T. Tadokoro, Y. Ueno, et al., *J. Appl. Phys.* 58(2019)106509.
- [9] A. Cavallini, B. Fraboni, P. Chirco, et al., *Nucl. Instrum. Meth. A* 448(3)(2000)558-566.
- [10] M. Jauhar Kholili, Doctor thesis SOKENDAI, Japan 2019.
- [11] DE. Wooldridge, AJ. Ahearn, JA. Burton. *Phys Rev.* 71(12) (1947)913.
- [12] AHB. Benny, FC. Champion. 234(1198)(1956)432-440.
- [13] M. Kamo, Y. Sato, S. Matsumoto, et al., *J. Cryst. Growth.* 62(3)(1983)642–644.

- [14] C.Jany, F. Foulon, P. Bergonzo, et al., Nucl. Instrum. Meth. A 380(12)(1996)107–111.
- [15] FG. Celii, JE. Butler. Annu. Rev. Phys. Chem. 42(1991)643-684.
- [16] SF. Kozlov, E. Belcarz, M. Hage-Ali, et al., Nucl Instrum Meth.117(1)(1974)277–283.
- [17] B. Marczewska, T. Nowak, P. Olko, et al., Diam. Relat. Mater. 13(4-8)(2004)918 -922.
- [18] B. Marczewska, I. Kupriyanov, Yu. Pal’yanov, et al., Diam. Relat. Mater. 16(2007)191-195.
- [19] M. Pomorski, E. Berdermann, A. Caragheorghopol, et al., Phys. Status Solidi A 203 (2006) 3152–3160.
- [20] P. Bednarczyk, E. Berdermann, J. Gerl, et al., Acta. Phys. Pol. B 38(2007) 1293–1296.
- [21] T. Shimaoka, S. Koizumi, J. H., Kaneko, Functional Diamond, 1(2021)205-220.
- [22] L Liu, X Ouyang, J Zhang, et al., AIP Advances 4 (2014) 017114.
- [23] H. Kagan, A. Alexopoulos, M. Artuso, et al., Nucl. Instrum. Meth. A 924 (2019) 297-300.
- [24] Y. Sato, T. Shimaoka, JH. Kaneko, et al., Nucl. Instrum. Meth. A 784 (2015) 147-150.
- [25] E. Bossini, N. Minafra. Front. Phys. 8 (2020). DOI: 10.3389/fphy.2020.00248.
- [26] JA. Dueñas, J de la Torre Pérez, A Martín Sánchez, et al., Appl. Radiat. Isot. 90 (2014) 177–180.
- [27] GR. Fern, PR. Hobson, A Metcalfe, DR.Smith, Nucl. Instrum. Meth. A 958 (2020) 162486.
- [28] F. Burkart, R. Schmidt, O. Stein, D. Wollmann, E. Griesmayer, “Experimental results from the characterization of diamond particle detectors with a high intensity electron beam”, in proceedings of IPAC2014, Dresden, Germany (2014): 3671-3673.

- [29] P. Dong, R. Eusebi, C. Schrupp, et al., “Beam Condition Monitoring with Diamonds at CDF. in proceedings of 15th IEEE-NPSS Real-Time Conference” (2007) 9871237.
- [30] M. Marinelli, E. Milani, G. Prestopino, et al., *Appl. Phys. Lett.* 89 (2006) 143509.
- [31] DS. McGregor, MD. Hammig, YH. Yang, et al., *Nucl. Instrum. Meth. A* 500(2003)272-308.
- [32] M. Angelone; G Aielli; S Almagora, et al., “Neutron Detectors Based Upon Artificial Single Crystal Diamond”, in proceedings of IEEE Trans. Nucl. Sci. 56 (2009) 2275-2279.
- [33] S. Almagora, M. Marinelli, E. Milani, et al., *J. of Appl. Phys.* 103 (2008) 054501.
- [34] M. Marinelli, E. Milani, G. Prestopino, R. Rosa and E. Santoro, *Appl. Phys. Lett.* 90 (2007) 183509.
- [35] P. Kavrigin, P Finocchiaro, E Griesmayer, et al., *Nucl. Instrum. Meth. A* 795 (2015) 88-91.
- [36] X. Xie, X Yuan, X Zhang, et al., *Nucl. Instrum. Meth. A* 761 (2014) 28-33.
- [37] IA. Zahradnik, MT. Pomorski, L. De. Marzi, et al., *Phys. Status Solidi A* 215 (2018) 1800383.
- [38] C. Weiss, H. Fraiss-Kölbl, E. Griesmayer, and P. Kavrigin, *Eur. Phys. J. A.* 52 (2016) 269.
- [39] RL. Bramblett, RI. Ewing, and TW. Bonner. *Nucl. Instrum. Meth.* 9(1960)1-12.
- [40] M. Awschalom, and RS. Sanna, “Applications of Bonner sphere detectors in neutron field dosimetry”, United States, 16(15)(1983)16054828.
- [41] R. Tursinah, B. Bunawas, J Kim. *GANENDRA Majalah IPTEK Nuklir.* 20(2)(2017)65-72.
- [42] Zhimeng Hu, Guoqiang Zhong, Lijian Ge, et al., *Nucl. Instrum. Meth. A* 895(2018) 100-106.
- [43] R. Bedogni, C. Domingo, N. Roberts, et al., *Nucl. Instrum. Meth. A* 63(2014) 547-552.

- [44] CIVIDEC Instrumentation: <https://cividec.at>.
- [45] MI. Kobayashi, M. Angelone, S. Yoshihashi, et al., *Fusion Eng. Des.* 161 (2020) 112063.
- [46] I. Mandić, V. Cindro, A Gorišek, et al., *JINST.* 8(2013) P04016.
- [47] J. Isberg, A. Tajani, and DJ. Twitchen. *Phys. Rev. B* 73(2006) 2452079.
- [48] H. Pernegger, S. Roe, and P. Weilhammer, *J. of Appl. Phys.* 97(2005)073704.
- [49] J. Bronuzzi, A. Mapelli, M. Moll, et al., *JINST.* 11(2016)P08016.
- [50] J.F Ziegler. SRIM. 1985, <http://www.srim.org/>.
- [51] T. Sato, Y. Iwamoto, S. Hashimoto, et al., *J. Nucl. Sci. Technol.* 55 (2018) 684-690.
- [52] M. Tsubota, JH. Kaneko, D. Miyazaki, et al., *Nucl. Instrum. Meth. A* 789 (2015) 50–56.
- [53] A. Brambilla, D. Tromson, P. Bergonzo, C. Mer, F. Foulon, “Thin CVD Diamond Detectors With High Charge Collection Efficiency”, in proceedings of IEEE Transactions on Nuclear Science. 49 (2002) 277-280.
- [54] XQ. Xu, M. Hagiwara, H. Iwase, M. Nakhostin, et al., “Gamma background rejection using CVD diamond neutron detectors”, proceedings of the 34th Workshop on Radiation Detectors and Their Uses. 2020 Jan 15; Tsukuba. Japan: KEK.
- [55] KURRI: Institute for Integrated Radiation and Nuclear Science, Kyoto University [Internet]. <http://www.rii.kyoto-u.ac.jp/gamma/>.
- [56] S. Yonai, T. Sanami, S. Sasaki, et al., *Health Physics.* 37 (2) (2002) 118-127.
- [57] JAEA-Review-2019-040, “Research and Development of Radiation-resistant Sensor for Fuel Debris by Integrating Advanced Measurement Technologies”.
- [58] K. Shibata, O. Iwamoto, T. Nakagawa, et al., ”JENDL-4.0: A New Library for Nuclear Science and Engineering,” *J. Nucl. Sci. Technol.* 48(1), 1-30 (2011).

- [59] T. Oyama, M. Hagiwara, T. Sanami, et al. Nucl. Instrum. Meth. B. 434(2018)29-36.
- [60] Mohammad Nakhostin, "Signal Processing for Radiation Detectors", book, 2018, 245.
- [61] S. berg, MODIFICATION OF SAND II.
<https://www.osti.gov/servlets/purl/4481466>.

Acknowledgments

I wish to express my gratitude to many people for the support and help that I received during my three-year Ph.D. program.

First and foremost, I am sincerely grateful to Professor Masayuki Hagiwara. I appreciate his patient guidance and tender encouragement over the past three years. Without his help, my research could not have begun. In addition, his financial support has made my life in Japan easier. Words cannot express my appreciation to him.

I express my sincere gratitude to my supervisor Professor Hiroshi Iwase, who provided valuable help with the PHITS simulations. During my Ph.D. program, he devoted considerable time and energy toward guiding my research. I am deeply grateful to him for various forms of help and valuable suggestions concerning my study.

I would like to thank Prof. Yoshihito Namito, Toshiya Sanami, Kiwamu Saito, Yuji Kishimoto, Hiroshi Iwase and Masayuki Hagiwara, the members of the dissertation committee. I am really very grateful for their helpful comments and discussions, which helped enhance the quality of my thesis. Many thanks to Professor Toshiya Sanami, who provided suggestions for revising my dissertation and research work. Special thanks to Professor Mohammad Nakhostin, who provided numerous valuable suggestions in the paper revision stage. I also wish to thank Dr. So Kamada, who provided financial support in the final year of my doctoral program, and my friend M. Jauhar Kholili, who shared with me a great deal of experimental knowledge when I was accepted to the Ph.D. program.

Finally, my deepest thanks go to my family and parents-in-law for their love and support. I also wish to thank my husband for his love and companionship. Furthermore, I wish to thank all the friends who supported me throughout my academic journey.

Xiuqing Xu

Declaration

I declare that I wrote this Ph.D.-dissertation independently and without any other references and resources than that stated in the bibliography.

Tsukuba, JAPAN